Co-registration of fluorescence diffuse optical tomography (fDOT) with Positron emission tomography(PET) and development of multi-angle fDOT

Thesis for the degree of Doctor of Philosophy (Ph.D.)

L'École Doctorale "Sciences et Technologies de l'Information, des Télécommunications et des Systèmes" (ED STITS)
Université Paris Sud

TONG Xiao

24/10/2012

Supervisor: Pr. Bertrand TAVITIAN
Tutor: Dr. Anikitos GAROFALAKIS

Composition of jury:

President: Dr. Irène BUVAT
Reviewer: Dr. Patrick POULET
Reviewer: Dr. Vincent LORIETTE
Member: Dr. Anne KOENIG
Member: Dr. Anikitos GAROFALAKIS

Acknowledgements

First of all I would like to express my deep appreciation and gratitude to my supervisor Pr. Bertrand Tavitian for his patient guidance and mentorship he provide to me, from the time when I first applied to the Ph.D. program in SHFJ, through to the completion of the thesis. Pr. Tavitian's unsurpassed knowledge in molecular imaging and his expertizing advices have been one of the most valuable gains during my three years thesis.

I express my sincere acknowledgement to Dr. Anne Flüry-Hérard, director of the SHFJ, for her kind intention and her advices to my thesis.

The accomplishment of this thesis would not have been possible without the help, the patience and his expertise in optical tomography of my tutor Dr. Anikitos Garofalakis, to whom I would like to express my sincere gratitude. Thanks to him, I have been able to discover the magical world of optical tomography.

I would like to express my deep gratitude to all members of the jury for sharing their expertise with the pertinent comments on my thesis, and respectively: to Dr. Irène Buvat, president of the jury and the chairman of my Ph.D. defense, for her grateful attention to the validation of my thesis in detail; to Dr. Patrick Poulet and Dr. Vincent Loriette, reviewers of my thesis, for their time and efforts spent on the pre-evaluation of my thesis; to Dr. Anne Koenig, member of the jury, for her assistance to my Ph.D. defense.

It is an honor for me to express my acknowledgement to the Computer Science Department of the UCL in London: to Pr. Arridge Simon for his kind reception during my visit to his team; to Dr. Teresa Correia who has helped me getting over all the difficulties I met with TOAST reconstruction during my last year of thesis; to Dr. Martin Schweiger for his generosity and his expertise in TOAST reconstruction and to all people in CS department with who I have spent a great moment there.

I would like to acknowledge my former tutor Dr. Albertine Dubois, who has helped me getting familiar with the work environment at the beginning of my thesis, been patient to help me with every bug I had in C++ and answer all my questions from scientific aspect to personal.

I own my gratitude to Dr Frédéric Ducongé, Dr Trébossen Régine, Dr Raphaël Boisgard, Dr. Alexandra Winkeler, Dr. Renault Maroy, Dr. Sebastian Jan and Dr. Claud Comtat who have supported me with my daily work in sharing their expertise, for the time they sacrificed in answering my questions and all the precious advices they gave me.

I would like to thank the secretariat of LIME madam Karima Ait Aissa and madam Maryse Mouveroux of SHFJ, for their great assistant so that I was able to concentrate on my work without having any worries about administrative problems. Great thanks are also given to the computer engineers Fabien Rastelo and Maximilien Piredda in SHFJ for their efficacious technique support to my daily work.

It is my pleasure to acknowledge my entire fellow students: Clare, Camille, Juan, Simon, Nicholas, Benoit… and everyone in SHFJ whom I have had the opportunity to meet during these three years, for their support, the friendship, the emotions and all the jokes we shared in leisure time.

Finally I deeply thank my parents for their support throughout my studies and their innumerable sacrifice for me: being worried about me at every moment, cheering for all my happiness, bearing all my depression and all my unreasonable emotion during these years. Their encouragement is a must-have for the achievement of my thesis.

1 General outline

The rapid development of molecular imaging techniques is progressively changing the way we practice Medical Imaging. While classical imaging explores mostly structural changes, molecular imaging techniques can provide information of the molecular processes that are the basis of structural or physical alterations in tissue. The most commonly used modalities of in-vivo imaging are: X-ray computed tomography (CT), Magnetic resonance imaging (MRI), ultrasound, nuclear medicine including Single-Photon Emission Computed Tomography (SPECT) and Positron Emission Tomography (PET), and optical imaging (OI).

Among the different optical approaches, diffuse optical tomography is a relatively new technique, which provides volumetric and quantitative images of the targeted subject by reconstructing spatially resolved maps of a biologically-relevant optical property within the tissue. In particular, the development of fluorescent optical probes has significantly improved the image contrast of the optical readouts. The combination of diffuse optical tomography with the use of fluorescent probes has led to the recent development of fluorescence diffuse optical tomography (fDOT), which reconstructs the three dimensional distribution of fluorescent probes within tissue. fDOT provides functional and quantitative fluorescent images with non-ionizing radiation and relatively inexpensive equipment. These characteristics make fDOT well suited for small animal studies, related to tumor imaging, drug discovery and gene therapy.

However, fDOT is a novel imaging technique that is still under development. In the context of multimodal imaging, different studies have demonstrated the potential interest of combining optical imaging with other modalities. The most common approach is the combination with CT images, where the latter can serve as an anatomical reference. In the present thesis, fDOT is co-registered with PET, which represents a functional imaging technique. The aim of this approach is to explore the potential of multimodal functional imaging. To build an automatic and feasible PET/fDOT co-registration method based on multi-modal fiducial marker was the first of the two objectives of this thesis. A co-registration algorithm was developed by taking in account the particularities of fDOT with respect to other modalities (CT, MRI, PET etc.).

The second objective of the thesis was oriented towards the improvement of fDOT reconstructions. The majority of fDOT systems are restricted to single camera (single angle) configurations, thus limiting the information gained from different angular views. As a consequence, the reconstruction quality of the fDOT is restricted in terms of depth resolution. This can be solved with the incorporation of gantries in a similar manner to well established tomographic imaging techniques such as PET or CT. A gantry system enables the recording of multiple-angle projections for image reconstructions. However these approaches result in increased apparatus costs and in challenging engineering. In the present study an approach is presented were multi-angle fDOT imaging is achieved with the use of mirrors. The aim was to improve fDOT reconstruction while retaining the instrumentation simplicity of the basic fDOT system.

The necessary basic theoretical background, implementation and accomplished results of this work will be presented in this dissertation in five chapters. The chapters are organized as followed:

In the next chapter, a basic introduction of the framework is presented, including an introduction to molecular imaging in pre-clinical research, the principle of optical tomography imaging and in particular of the fDOT imaging system. The challenges of multimodality imaging and the concept of image registration are also described This

part intends to show the context of the study and the basic knowledge acquired for implementation of objectives.

In chapter three, the first part of the thesis concerning the automatic co-registration of the fDOT with PET is presented. The method is based on the automatic detection of fiducial markers visible in both modalities. The novelty of our method relies on the introduction of surface extraction techniques in the fDOT imaging acquisition and analysis. Quantitative evaluation after testing this method on a set of experiments confirmed the feasibility of this co-registration method. The method was applied to a practical tumor study, with co-registration of FDG-PET images of glycolysis and of tumor vascularity with fDOT using Sentidye® fluorescent probe.

In the fourth chapter, the second part of the thesis related to the improvement of depth resolution in fDOT reconstruction will be presented. After analyzing the drawback of the conventional fDOT imaging system, the improvement proposed is to develop a new multi-angle fDOT system with two mirrors redirecting the signal coming from the lateral side of the subject to the camera. The new fDOT reconstruction method was tested on two different types of experiments: phantom and mouse kidney. The reconstruction based on the mirror geometry was compared with the conventional geometry to determine the improvement in depth resolution.

Finally, in the fifth chapter, the essential elements of the study presented in chapter four will be discussed. The final section concludes the thesis with the summary of the works accomplished during the three year PhD thesis, the possible applications and the general perspective that may be valuable for future research.

Table of content

Acknowledgements....1
1 General outline....5
2 Introduction....13
2.1 Molecular imaging....14
2.2 Molecular Imaging Techniques....14
2.2.1 Nuclear imaging, Single-Photon Emission Computed Tomography (SPECT) and Positron Emission Tomography (PET)....15
2.3 Optical imaging....16
2.3.1 Bioluminescence imaging....18
2.3.2 Planar fluorescence imaging....19
2.3.3 Diffused Optical tomography (DOT) and fDOT....22
2.4 Challenges in Multimodality imaging....25
2.4.1 X-ray Computed Tomography (CT):....26
2.4.2 Multimodality imaging:....27
3 Automatic Co-registration of fDOT and PET images....29
3.1 Complementarity of PET with fDOT....31
3.2 Materials....33
3.2.1 Animal models....35
3.2.2 Imaging probes....36
3.3 Method- Image Acquisition....36
3.3.1 Acquisition of the Optical Images....36
3.3.2 PET Image Acquisition....39
3.4 Method - Image co-registration....40
3.4.1 Theory of the image co-registration....40

3.4.2 Fiducial markers method for FDOT 45
3.4.3 Co-registration of fDOT image with PET image 47
3.5 Results 54
3.5.1 Co-registration procedure 54
3.5.2 Quantitative Evaluation of the Co-registration 56
3.5.3 In-vivo Co-registration of tumor vascularity and metabolism 59
3.6 Discussion 65
4 Multi-angle fDOT imaging with the use of mirrors 71
4.1 The conventional fDOT system and the multi-angle approach 75
4.1.1 The conventional fDOT system 75
4.1.2 Multi-angle optical imaging 76
4.2 Image reconstruction 81
4.2.1 Forward problem - Diffuse optics theory 82
4.3 Inverse problem 86
4.4 Materials and Methods 89
4.4.1 Experimental Setup 89
4.4.2 Tissue-like phantoms 89
4.4.3 Data processing algorithm 90
4.4.4 Incorporation of mirrors in a conventional fDOT imager 90
4.4.5 Implementation of the TOAST reconstruction algorithm 93
4.4.6 Mesh file generation. 94
4.4.7 The Source/detector file (QM file) 97
4.4.8 Data file - Fluorescence matrix (M_{fluo}) and Excitation matrix (M_{exc}) 99
4.4.9 Modification and execution of the TOAST algorithm with the generated input data 101
4.5 Results 103
4.5.1 Semi-cylindrical phantom experiment 103
4.5.2 In-vivo experiments 106
4.6 Quantitative evaluation of the reconstruction 109
4.6.1 Quantitative evaluation of the phantom experiment 109
4.6.2 Quantitative evaluation of the in vivo experiment 112
5 Discussion 115
5.1 Reconstruction parameter 115
5.2 Comparison of TOAST reconstruction with TOMOFLUO3D reconstruction

118
5.2.1 The reconstruction comparison of phantom experiments 118
5.2.2 The reconstruction comparison of in-vivo experiments 119
5.3 The use of CT image for mesh generation 122
5.4 Conclusion 125
6 Annex 129
6.1 An example of the mesh file in TOAST 129
6.2 An example of the QM file in TOAST 130
7 List of publication and communications 133
8 References 135

2 Introduction

Medical imaging, used to explore the human body in order to diagnose, monitor, or treat disease (Elliott, 2005), is based on the observation of contrast between diseased and healthy tissues. Obtaining a specific contrast is of particular diagnostic value and facilitate the early identification and staging of pathologies (Riker et al., 1997; Black, 1998) The most commonly used imaging modalities include radiography, magnetic resonance imaging, nuclear imaging, ultrasound imaging and optical imaging. Each type of technology provides a different type of information about the studied subject, by relating tissue condition to the measurement of a physical property, e.g the radioactivity concentration in nuclear medicine. These measurements provide insight into the biochemistry or physiology of tissue.

Conventional imaging methods probe structural or micro-structural and physiological alterations in tissue. However, these alterations are the results of molecular processes such as the activation or inhibition of a molecular receptor, or a physiological signal pathway (Mattson, 2000; Massoud and Gambhir, 2003). Molecular imaging is of particular interest because it allows the direct visualization of these molecular events.

2.1 Molecular imaging

Advances in molecular biology, applied physics and biotechnology allowed the development of powerful tools for the imaging of the biological tissue. New imaging techniques have been developed for the direct visualization of molecular events. In contrast to “classical” imaging, molecular imaging sets forth rather to probe the molecular abnormalities that are the basis of disease, rather than image the ending effects of these molecular processes (Weissleder et al., 1999; Weissleder, 2002). Molecular imaging exploits molecular processes with non-invasive methods to generate image contrast and provides annotations of molecular, structural and biochemical information. Based on the above, molecular imaging can be broadly defined as the non-invasive in-vivo characterization and measurement of biologic processes at the cellular and molecular level (Miller and Thrall, 2004; Rudin, 2005; Rudin et al., 2005; Weissleder, 2006).

An important aspect of molecular imaging is its capacity to provide quantitative data, hence a greater degree of objectivity for the diagnosis of disease. The ability to image and quantify molecular changes opens up a number of exciting possibilities for medical applications, including the early detection of cancer based on the detection of specific biomarkers (Munnink et al., 2009; van der Meel et al., 2010) and efficient testing of new drugs in pre-clinical and clinical tests (Rudin, 2005; Hampel et al., 2011).

2.2 Molecular Imaging Techniques

Efforts have been oriented towards the development of high-resolution, in-vivo technology, for studying diseases noninvasively and quantitatively at the molecular level (Weissleder, 2002; Massoud and Gambhir, 2003). The rapid growth of molecular

imaging has provided scientists with tools for the visualization of molecular processes. The most basic and the most commonly used modalities in molecular imaging include Nuclear Imaging, Optical Imaging, Magnetic Resonance Imaging and Ultrasound,. The studies presented in this thesis revolve around the first two modalities.

2.2.1 Nuclear imaging, Single-Photon Emission Computed Tomography (SPECT) and Positron Emission Tomography (PET)

Nuclear imaging methods detect radioactive radiation emitted by a decaying radionuclide (Rudin, 2005). SPECT and PET are both clinically established technologies and suited for translational applications (Stahl et al., 2004; Sharma and Ebadi, 2008).

SPECT: the gamma radiation emitted by the radioisotope is detected directly by a gamma camera. Multiple 2D images (projections) are acquired in multiple angles that provide 3D information. However, the signals are detected by detector equipped with collimators that reducing the space angle. Therefore, the sensitivity is less than in PET scanners (in the order of nano-molar concentrations in comparison to pico-molar concentrations achieved by PET). Typical values of the spatial resolution for SPECT (Rudin, 2005) are in the order of 10mm for clinical scanners. In preclinical studies millimeter or sub-millimeter resolution is achieved by multi-pinhole techniques (Beekman and Van der Have, 2007; Gross, 2005).

PET: PET radioisotopes emit positrons during positive beta decay. In the body the positron travels through the tissue for a short distance before being annihilated with an electron (Townsend, 2004). The annihilation produces two gamma photons that are emitted in opposite directions. These photons are detected by a scintillator detector, which creates a burst of light that is detected by photomultipliers. Coincidence detection yields a line of response on which the annihilation has occurred. During the time between positron emission and positron annihilation the particles travels 0.5-3mm, depending on the initial energy of the positron emitted

(Rudin, 2005). Typically the resolution of PET is of the order of 6-8 mm for clinical scanners (Townsend, 2004), and 1-1.5mm for small-animal scanners. An important advantage of PET is its high sensitivity, which allows the use of tracer concentrations that are far below the pharmacological effective dose (Rudin, 2005).

PET is considered both a medical and research tool. It is commonly used in clinical oncology (Delbeke and Martin, 2001) and neuroimaging (Kim et al., 2010) for diagnosis of brain diseases. PET is also an important research tool to map normal human brain and heart function (Gusnard et al., 2001). PET scanning is non-invasive, but involves exposure to ionizing radiation. Thus, safety precaution should be paid to the total dose of radiation received by the patient.

Improved spatial resolution allows PET imaging of mouse models of human disease, so that preclinical findings and concepts can be translated *a posteriori* into the clinical context. By employing the same technology in an experimental setting and in clinical practice, the translation from preclinical research to clinical application is facilitated (Nanni et al., 2007). Small animal PET (Myers and Hume, 2002), which are adapted to the geometry and size of mice, have been developed for molecular imaging studies. They exhibit substantially higher sensitivities (in the order of 10^{-11} – 10^{-12} M) (Rudin, 2005) than the clinical PET scanners. A main advantage of small animal PET is the possibility of longitudinal studies of the disease evolution and of the response to a specific therapy (Nanni et al., 2007). Applications of the PET imaging in preclinical studies include drug development (Tsukada, 2011), targeted radiotherapy of cancer (Anderson and Ferdani, 2009) and preclinical evaluation of tumour angiogenesis (Nayak et al., 2011).

2.3 Optical imaging

As stated in the previous section, medical images of living tissue can be obtained by using techniques such as CT, PET, Ultrasound or MRI. Each of the aforementioned techniques exhibits specific advantages and limitations. Despite constant advances in

the existing imaging technologies, the development of new modalities is still at the center stage of molecular imaging research. There is a high interest in developing modalities characterized by a reduced cost and use of non-ionizing radiation, and that can provide molecular and functional information on molecular processes. In the microscopic domain, a number of optical imaging techniques have been developed, including confocal imaging (Claxton et al., 2006), multi-photon imaging, or microscopic imaging with intravital microscopy (Tabuchi et al., 2008).

In recent years, molecular imaging has encountered the rapid development of macroscopic imaging using light (Weissleder and Ntziachristos, 2003). Light is nonionizing over many wavelengths and in the Near Infra-Red (NIR), it can penetrate deep in tissue. This range of wavelengths where light exhibits low absorption is called light's "biological window", which is also known as the "NIR window" (Weissleder, 2001) (Figure 2-1). The figure below presents the absorption spectrum of the three major tissue chromophores: water (H_2O), oxyhemoglobin (HbO_2) and deoxyhemoglobin (Hb). As can be seen the area of low absorption spans the range between 600nm and 900nm.

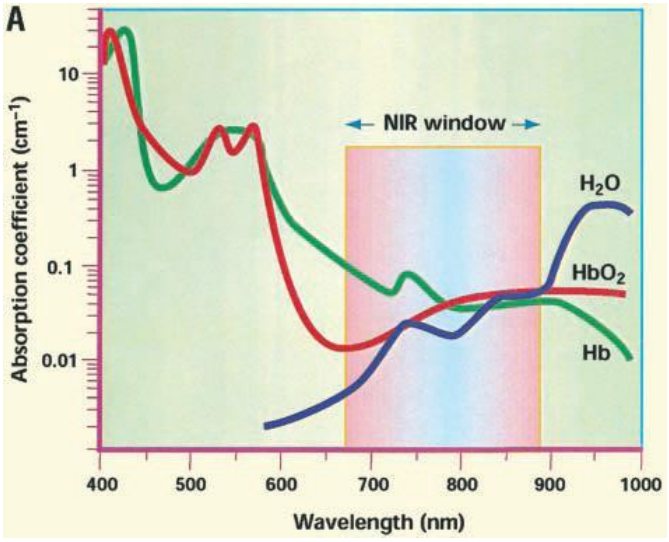


Figure 2-1: Absorption spectrum of the three major chromophores in tissue: water (H_2O), oxyhemoglobin (HbO_2) and deoxyhemoglobin (Hb). Within the NIR window, the absorption coefficients of all three chromophore are relatively low (Sharma et al., 2006).

In the NIR window, photon propagation in tissues is possible over many cm

(Ripoll et al., 2005). During light propagation in tissue, photons are absorbed but also scattered. In the “biologic window” where tissue absorption is low, the scattering of light is the predominant process that influences light propagation. Due to this effect, light propagates in a diffusive manner. The influence of the optical properties on light’s propagation can be used to quantify these properties. These, in turn, often characterize tissue pathologies.

Macroscopic optical imaging methods have received great attention in recent years. The main reason has been the development of a technology that incorporates NIR laser sources and sensitive cameras for probing signals originating from large-scale subjects. Advances in the field of tissue optics allowed the theoretical description of the propagation of light with tissue thus giving rise to 3D reconstruction techniques (Chance et al., 1992). The potential of this novel technology has been demonstrated by the probing of hemodynamics (Boas et al., 2004), detection of tumors (Ntziachristos and Chance, 2001; Yodh, 2008) and providing functional imaging of the brain (Benaron et al., 2000; Culver et al., 2003).

There are three major macroscopic techniques for small animal imaging: Bioluminescence imaging, planar fluorescence imaging and optical tomography.

2.3.1 Bioluminescence imaging

In bioluminescence imaging, the enzyme luciferase transgenically expressed in transgenically modified animal models serve as the source for the contrast agent. After the administration of luciferin via injection, oxidation of the luciferin substrate occurs and visible light is emitted (Contag et al., 1998). The emitted photons travel through the tissue and are recorded by photon sensitive cameras that focus on the surface of the animal (Figure 2-2).

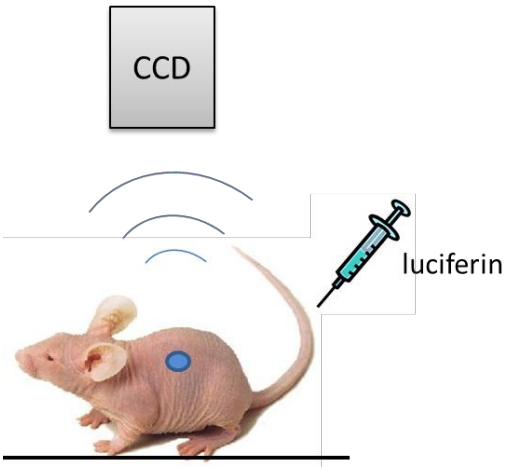


Figure 2-2: Schematic representation of bioluminescence imaging (BI). After the administration of luciferin, planar image of the emission light from the luciferase is captured by the CCD camera.

Bioluminescent studies mainly involve the imaging of gene expression products (Contag and Bachmann, 2002) and the tracking of tumor cells (Sweeney et al., 1999). Luciferase imaging provides images of surface events with a high signal to noise ratio, since the light is intrinsically generated without any external excitation. However, full quantification of signal located deep inside the subject is not yet feasible.

Overall, Bioluminescence technique is a very sensitive technique and enables throughput measurements; however the requirement of systemic delivery of the luciferin substrate to the animal is a limitation for long-term experiments. Another drawback is that the intensity of emission and the peak wavelength strongly depend on the temperature and the pH.

2.3.2 Planar fluorescence imaging

Molecular biology and biotechnology have provided tools to label cells and molecules with fluorescent probes, to produce valuable contrast agents for optical imaging studies (Bremer et al., 2003; Nolting et al., 2011). Fluorescent contrast agents, which were first applied in cell biology (Zhang et al., 2002) and cell microscopy (Brown et al., 2001), provide high signal to noise ratio and high specificity,

thus significantly improving the detection limit, the resolution and the depth of localization.

Fluorescent probes label the target via three major labeling mechanisms (Figure 2-3):

a) Vascular probes (nonspecific probes): One hallmark of tumor and inflammation is enhanced vascular permeability (also called the Enhanced Permeability and Retention effect). Passive targeting of the vascular probes is achieved by extravasation of these long-circulating nanoparticles through increased permeability of the tumor vasculature and accumulation in the pathological site. (Maeda et al., 2000). In addition, maintaining a required level of the vascular probes (nanoparticles) in the blood and a prolonged circulation can help to achieve a better targeting effect for nanoparticles and allows more time for interaction with the target tissue (Torchilin, 2007).

b) Targeted probes: a fluorophore is attached to a ligand, which is specific for a receptor. Targeted probes are generally used to determine the position of the receptor concentration, or localize proteins. In antibody labeling, the fluorescent labeling uses the specificity of antibodies binding to their antigen to target fluorescent dyes to specific targets within a cell, and therefore allows visualization of the distribution of the target molecule (Vira et al., 2010).

c) Activatable probes: Activatable near-infrared fluorescent probes have been recently developed (Weissleder, 1999) and they represent a unique contrast technique in the field of Molecular Imaging. These probes are initially quenched and thus non-fluorescent. Upon interaction with the target, they are dequenched and emit light. These probes cleaved by a specific target. Thus, probes undergo a change in their optical properties (Lovell and Zheng, 2008). This activatable (quenching and dequenching) approach represents an amplification phenomenon that increases target-to-background ratios. It holds promise for imaging of a number of endogenous proteases in cancer, inflammation (including inflammatory arthritis), cardiovascular diseases, infections and degenerative diseases in humans (Weissleder et al., 1999; Massoud and Gambhir, 2003).

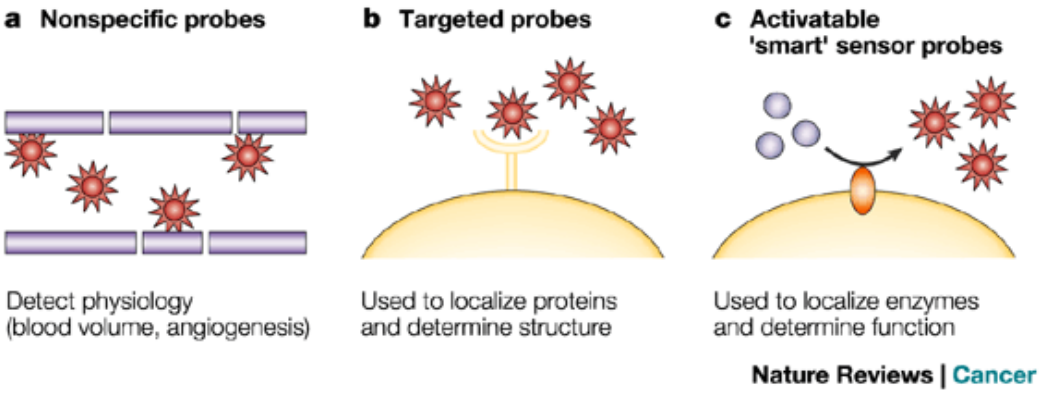


Figure 2-3: Three types of probe labeling mechanisms: a) nonspecific probes detect physiological parameters (blood volume, perfusion, flow) and target passively by extravasation through EPR effect in tumors, b) targeted probes specific for their receptor localize and determine the target tissue, and c) activatable "smart" probes are detected only after activation by the target (Weissleder, 1999).

A variety of probes including the activatable probes have been used for molecular imaging studies in mice (Weissleder and Mahmood, 2001). The simplest way to detect fluorescence from a macroscopic subject is by planar fluorescence imaging. The fluorescent agents are administered to the animal and fluorescent signals are produced upon excitation by a planar light exposure (Ntziachristos et al., 2005; Ntziachristos, 2006) (Figure 2-4) . The excitation light has a defined bandwidth, which corresponds to the excitation spectra of the fluorophores. When it encounters the fluorescent probes, the latter emits a signal with different spectral characteristics that can be resolved with an emission filter and captured with a high-sensitivity charge-coupled–device (CCD) camera.

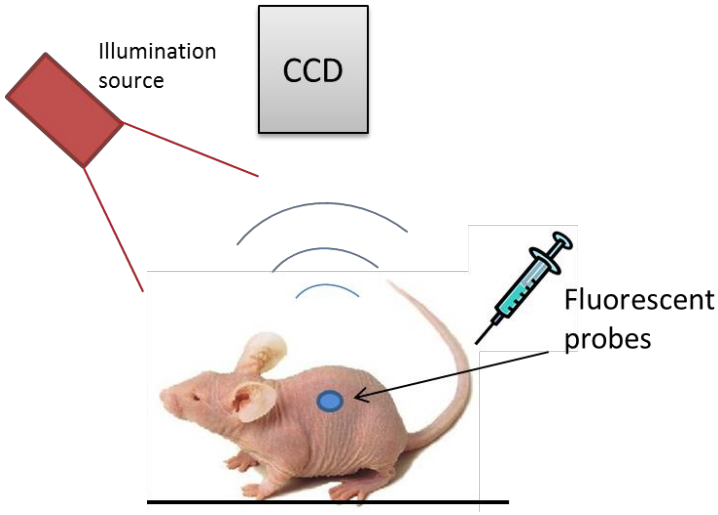


Figure 2-4: Schematic representation of planar fluorescent imaging (PFI). The emission of the fluorescent light after the excitation of fluorescent probes is captured by the CCD camera, in epi-illumination geometry.

Planar fluorescence imaging, which is also called fluorescence reflectance imaging (FRI), is a simple and high throughput technique for in vivo surface imaging. However, planar imaging lacks multiple projections and the nonlinear dependence of light is not accounted for. Therefore, resolution in depth is not feasible and the ability of volumetric quantification of fluorescent signals is restricted within a depth of a few millimeters under the skin (Ntziachristos, 2006).

2.3.3 Diffused Optical tomography (DOT) and fDOT

Over the last fifteen years, optical tomography has become one of the main tomographic modalities applied to molecular imaging studies. Diffuse Optical Tomography (DOT) was the first technique developed aiming at reconstructing three-dimensional maps of the optical properties of tissue, such as oxygen saturation and blood volume (Ntziachristos et al., 2001).

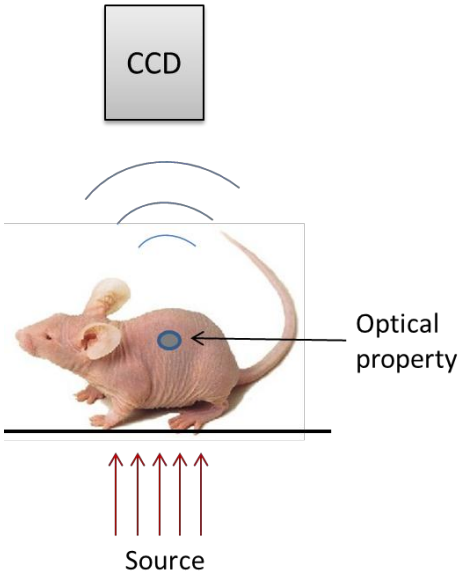


Figure 2-5: Schematic representation of diffuse optical tomography (DOT). The CCD camera captures the emission light defined by the optical property of the tissue, after source illumination in trans-illumination geometry.

For DOT, as shown in figure 2-5, a NIR laser source illuminates the subject and a camera captures the signals on the opposite side. Images of transmitted light are recorded at different source/detector positions by moving the source and/or the camera and/or the subject. 3D images of the targeted property are then reconstructed by applying mathematical algorithms that take into account the absorption and the scattering of light during its propagation through tissue. DOT can provide volumetric and quantitative images of the optical properties of the targeted subject (Ntziachristos et al., 2001).

Fluorescence diffuse optical tomography (fDOT) or fluorescence molecular tomography (FMT) (Ntziachristos and Weissleder, 2001) has developed to provide better contrast sensitivity in comparison to DOT. FDOT incorporates the principles of DOT in combination with the use of fluorescent probes to improve contrast (Figure 2-7). For fDOT acquisition, the tissue of interest is illuminated with a NIR laser light. The excitation photons travel through tissue and a portion of them interact with a fluorescent target. During this interaction, the excitation photon is absorbed and a fluorescence photon is emitted with a longer wavelength (Figure 2-6).

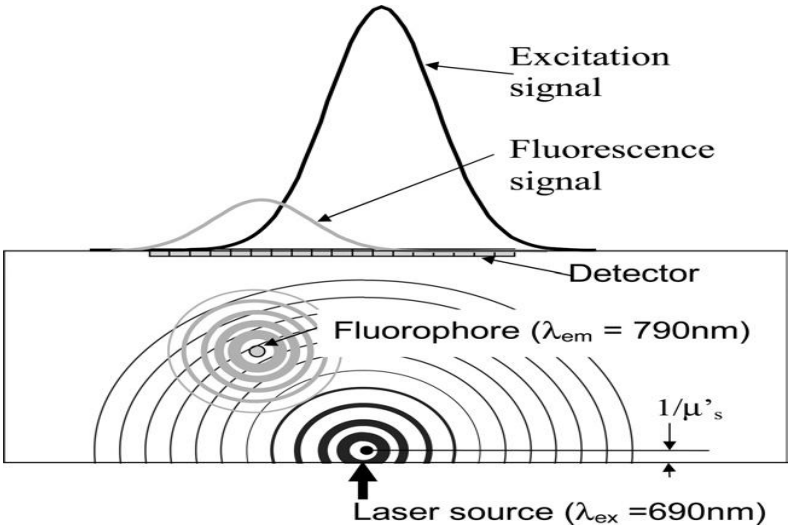


Figure 2-6: Scheme of the excitation signal of the laser source and the fluorescence signal of the fluorophore upon excitation (Hervé et al., 2007).

As mentioned, in the NIR spectral wavelength, the photon propagates in biological tissue through diffusive process. A detector captures the photons reaching to the surface. In switching between appropriate filters, both excitation and fluorescence photon signals can be measured.

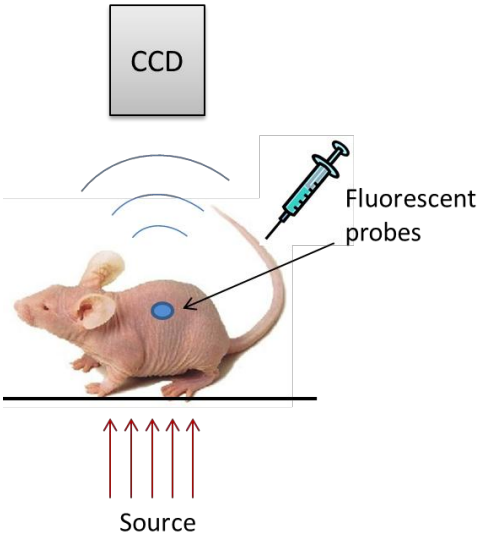


Figure 2-7: Schematic representation of fluorescent diffuse optical tomography (fDOT). The emission of the fluorescent light after the excitation of fluorescent probes is captured by the CCD camera, in trans-illumination geometry.

The first fDOT modalities incorporated fiber detectors in contact with the probed medium (Ntziachristos and Weissleder, 2001). Recent systems account for the free-space propagation of the transmitted light, thus enabling the development of non-contact fDOT imaging (Deliolanis et al., 2007). The non-contact approach enables CCD-based measurements which are characterized by higher spatial sampling, when compared to the fiber-based systems, resulting in improved resolution (Culver et al., 2003; Graves et al., 2003). fDOT 3D images are the result of a reconstruction process using algorithms that take into account the propagation of light and the geometry of the subject. A detailed presentation of these algorithms will be given in chapter 3.

FDOT is capable of resolving and quantifying fluorophores with nano-molar sensitivity in small animals and can achieve several centimeters of tissue penetration. FDOT provides 3-dimentional functional and quantitative images. An important advantage of fDOT in comparison to BI and PFI is its quantification capacity. Additional advantages include the fact that beacons and fluorophores are usually stable and do not decay like isotopes and that the technology is relatively inexpensive compared with other tomographic imaging systems. These characteristics make fDOT well suited for small animal studies, especially for cancer detection, drug discovery and gene therapy (Graves et al., 2003). It is also conceivable to perform multi-wavelength imaging to obtain information from multiple targets (Grieve et al., 2006).

2.4 Challenges in Multimodality imaging

Basic molecular imaging techniques have been presented with emphasis on optical imaging and its fluorescent counterpart, the fDOT. Each technique has advantages but also limitations, and the information that can be extracted from each modality has distinct characteristics. The MRI offers anatomical images of notable

spatial resolution, but it may not provide high-sensitivity functional information. In contrast, nuclear imaging may monitor specific functional or metabolic processes in a highly specific way, but generally lacks spatial resolution to allow probing of anatomical structures. Differences also concern the potential harmfulness induced by the modality.

Besides the molecular imaging techniques presented above, a conventional imaging modality: X-ray Computed Tomography (CT) has been commonly used to provide anatomical landmarks and co-register with different molecular imaging techniques.

2.4.1 X-ray Computed Tomography (CT):

In CT images, the contrast is due to tissue specific attenuation of X-ray beams travelling inside tissue. CT provides high-contrast resolution that allows distinguishing differences in the physical density of the tissue (Goldman, 2007). The development of the CT scanner made feasible the collection of full 3D data set that covers the whole subject. CT provides unsurpassed signal intensity of bony structures, but is also applied to studies of pulmonary diseases as it yields high contrast image for lung parenchyma and adipose tissue (Langheinrich et al., 2004). CT scanning can also be used in brain imaging to detect infarction, tumors etc., and in cardiac imaging for imaging of the coronary arteries. In clinical scanners the resolution is typically of the order of 0.5 -1 mm and for animal scanner, in the order of 10μm or less (Rudin, 2005).

The administration of contrast agents containing iodine or barium enhances X-ray contrast (Widmark, 2007). Contrast agents allow CT to give some contrast to anatomical images of soft tissue, e.g. kidney, in small animal. Consequently, CT is generally used as an anatomical reference for molecular imaging. However, one significant drawback of CT is the radiation dose delivered during the imaging session. The radiation in some cases can lead to damage of the tissue and increase the risk of cancer (Anand et al., 2008). Precautions are needed to avoid excess radiation dose to the patients.

2.4.2 Multimodality imaging:

As mentioned, different imaging modalities have different characteristics and each of them provides either functional or anatomical information. The development of multimodality imaging has originated from the need to compare information from multiple modalities in order to realize the complete study of a single subject. Multimodality imaging has been proposed as a means to enhance the information obtained from the use of one single imaging modality (Cherry, 2006; Townsend, 2008). Multimodality imaging facilitates the process of complementing functional data with anatomical data, thus facilitating the localization of the functional images.

The first implementation of multimodal imaging concerned the fusion of SPECT with CT for clinical purposes (Hasegawa et al., 2002). Since then, the number of combined SPECT/CT and PET/CT scanners has increased steadily because of their wide clinical utility. The main application of PET/CT imaging is found in the field of oncology (Kapoor et al., 2004). SPECT/CT and PET/CT systems were introduced by the major scanner manufacturers for routine clinical use (Beyer et al., 2000; Hasegawa et al., 2002).

Recently, the development of prototype systems that combine PET with MR Imaging represented a major technological achievement. The advantage from the use of MRI is the ability to image soft tissue contrast as well as functional processes. Some studies have reported the application of this multi-modal approach in the field of cardiac imaging (Nekolla et al., 2009) and high-resolution brain imaging (Cho et al., 2008).

The clinical technology was soon transferred to preclinical research with the development of small-scale system analogs devoted to animal studies. Preclinical multimodal systems need to address multiple instrumentation challenges. The subject should be measured by two techniques while maintaining its geometrical position between the two acquisition sessions. In addition the multi-modal system should provide co-registered images from the multiple scans.

There are two approaches for addressing the above requirements: sequential

acquisitions sessions (Nahrendorf et al., 2009) between different modalities, and systems that allow simultaneous acquisitions with combined multi-modal detectors (Goertzen et al., 2002).

Currently, the majority of multimodality research studies involve sequential imaging by moving the mouse support from one system to the other (Stout and Zaidi, 2008). The sequential approach has been more commonly applied because of its simplicity. The main drawback of sequential imaging concerns the risk of changing the animal position when it is displaced between the imaging sessions. One solution for sequential imaging was the use of imaging chambers (Suckow et al., 2009). This approach integrated heating, anesthesia, and positioning within a chamber bearing a common mounting plate for the different modalities. The chamber can be fixed in the same location enabling a fixed translational offset to co-register the data, eliminating the often difficult task of software registration. Further refinements with software enable automated processing to create the fused images without user interaction, thus simplifying the creation of data and lessening the burden for the user (Suckow et al., 2009).

Data processing in multimodality imaging concerns the use of software to achieve co-registration and fusion of multiple images. Depending on the type of the acquisition system, image registration software needs to account for misalignment due to the bed transportation or the movement of the animal between the different image scans (Chow et al., 2006).

.

3 Automatic Co-registration of fDOT and PET images

Several multimodality imaging systems are either in use or under development. As presented in the previous chapter, the most commonly used systems in practice, consist of dual-modality imaging scanners that combine anatomical imaging with functional imaging. fDOT was mainly fused with CT, so that the fDOT functional image could be visualized and processed in comparison to a structural reference image provided by CT.

Recent studies have demonstrated the potential interest of combining fDOT with PET (Prout et al., 2004; Nahrendorf et al., 2010; Li et al., 2011). FDOT/PET dual-modality imaging involves two functional modalities, where each one provides information about a different process. This combination may serve to enhance the molecular information originating from a single subject at a given time point. The first attempts in combining fDOT with PET showed that complementary information was achievable and demonstrated the imaging performance of fDOT in comparison to PET. However, only few studies are devoted to the combination of PET with fDOT mainly due to the technical difficulties or some misconceptions for the benefits of the combined images. Another reason is that fDOT is a relatively novel technique and in constant development in comparison to the established PET technology.

In oncologic imaging, there is a clear trend towards multimodal imaging of tumor

as the best way to provide relevant information on a significant number of various cancer hallmarks (Culver et al., 2008; Hanahan and Weinberg, 2011). The complexity of tumors interactions with their environment calls for imaging methods capable of detecting a diversity of tumor hallmarks (Egeblad et al., 2010; Hanahan and Weinberg, 2011). Positron emission tomography (PET) with [18F]2-deoxy-2-fluoro-D-glucose (FDG), the most efficient imaging method to detect cancer, is an indicator of tumor energy metabolism dominated by aerobic glycolysis in both cancer and tumor-associated inflammatory cells (Gillies et al., 2008). However, FDG-PET carries no information about other cancer hallmarks such as angiogenesis, replicative immortality, evasion of growth suppressors, capacity to metastasize, and yields at best indirect information on resistance to apoptosis and proliferation (Hanahan and Weinberg, 2011). PET imaging with other radiotracers can complement FDG, although radiolabeling of multiple tracers add in the complexity of an experiment. As far as experimental molecular imaging is concerned, multiple PET sessions are difficult to envision on a large scale because of high cost and low practicability.

Important information can be extracted from fusion images of glucose activity given by FDG-PET and an optical probe targeting a tumor-related process. The fusion images require image processing tools that would process images acquired separately by the different modalities. Given the resolution of small-animal PET and fDOT scanners (1–2 mm), accurate and reliable co-registration between both modalities is essential. Among different co-registration methods that have been developed, such as geometrical co-calibration (Cao et al., 2010) and dynamic contrast methods (Hillman and Moore, 2007), the use of fiducial markers (FM) (Nahrendorf et al., 2010) in close position to the body of the animal is the most straightforward and universal approach today. The coordinates of the FM in images acquired independently are used for the geometrical transformations leading to the fusion of images. Co-registration of large data sets from different imaging modalities results in time-consuming, tedious and operator-dependent image analyses when performed manually. Therefore, methods for the automatic identification of the FM's coordinates have been developed for co-registration of computed tomography (CT),

PET and magnetic resonance imaging (MRI) modalities (Wang et al., 1996; West et al., 1997; Fitzpatrick et al., 1998; Liu, 2003; Yang et al., 2006). However, so far, these methods have not been adapted to co-registration with fDOT because fDOT reconstructions are spatially restricted and do not cover the FM positions

In the present thesis, the use of surface images obtained during fDOT acquisition session was introduced for automatic identification of the FM's positions in space. Surface reconstruction by laser patterning can retrieve the 3-D surface of the subject and that of the FM located in its close vicinity (Bernardini and Rushmeier, 2002). Surface reconstruction is directly implemented into the 3-D fDOT-PET combined image.

In this chapter, the new method for automatic co-registration of fDOT image with PET image is presented. In section 3.1, the basic features of fDOT and PET are presented together with their complementarity for molecular imaging studies. In section 3.2 the material including the mouse model and the imaging probes are described. In section 3.3, the instrumentation and the image acquisition of our method are presented, focusing on the novelty of our method of optical surface extraction in fDOT. In section 3.4, the fiducial marker based image co-registration taking into account the particularity of the fDOT technique is described, with the details of the image processing procedure used in our method. Section 3.5 presents the results showing the co-registration of fDOT and PET images of the same mouse together with the quantitative evaluation of this method. As a proof of concept, mice bearing neuroendocrine tumors have been imaged for glycolytic metabolism with FDG-PET and for tumoral blood pool with a fluorescent blood pool contrast agent. Finally, a conclusion for this chapter is given in 3.6.

3.1 Complementarity of PET with fDOT

In this study, we were particularly interested in exploring the potential of fusing PET with the fDOT. PET is a well-established technique that is routinely used in clinic

for the diagnosis and staging of tumors. In preclinical research, the notable advantage of PET consists in a sensitivity in the range of pM and short acquisition times qualifying it as the reference method to analyze early probe pharmacokinetics (Pryma et al., 2006; Khandani et al., 2007). PET systems are suited for whole-body measurements enabling the parallel measurement of kinetics in multiple organs. The main shortcomings of the nuclear methods are their high implementation and maintenance costs and the need of security precautions due to radioactivity.

In the table below, the imaging features of the PET are compared to of fDOT.

	PET	**Optical**
Resolution	~ 1 mm^3	~ 1 mm^3
Kinetics	Fast (~1min)	10-15 min/scan
Time range of follow up	~ hours	~days
Cost	Expensive	Low cost
Activatable probes	NO	YES
Labelling	Need radiochemistry	Easy
Sensitivity	pM	nM

Table 3-1 Comparison of the major feature of the PET imaging technique with the fDOT technique in preclinical study

This table shows some notable imaging features of the fDOT technique. For instance, it is comparable with PET in terms of resolution and also offers nanomolar sensitivity (Garofalakis et al., 2010). fDOT is non-radioactive imaging and in controlled intensities does not cause any harm to the tissue. In contrast to imaging modalities demanding heavy instrumentation such as PET, fDOT is based on relatively simple hardware that does not require a sophisticated technological environment or tedious safety precautions. In terms of cost, fDOT is a low cost imaging system comparing to PET system that may serve as a technique of choice for functional imaging studies. fDOT also benefits from the huge portfolio of fluorescent probes and beacons that have been developed against a variety of molecular targets (Ntziachristos et al., 2002; Martin et al., 2008; Garofalakis et al., 2010). An important unique feature of optical

imaging is the availability of activatable probes that present some important imaging advantages, like an increased signal to noise ratio and a high specificity. Fluorescent probes may stay active over days or even weeks, enabling extended longitudinal studies.

Although fDOT may not replace PET in many applications, it can complement standard PET readings by enhancing the information that is extracted from a single subject. Preliminary studies have shown the potential of combining these two modalities: Nahrendorf et al (2010) have proposed a hybrid PET-optical imaging approach using biocompatible targeted nanoparticles that were imaged sequentially with both modalities. A good correlation between the PET and fDOT image was found in terms of probe concentration ($r(2) > 0.99$) and spatial signal distribution ($r(2) > 0.85$). This study suggested that fDOT can serve as a surrogate modality for the screening and development of radionuclide-based imaging agents (Nahrendorf et al., 2010). Li et al (Li et al., 2009) have developed a simultaneous PET and 3D fDOT system. This system on one hand provides a method of 3D fDOT imaging using simultaneous PET information as prior to guide the image reconstruction, and on the other hand demonstrates the feasibility of simultaneous PET and 3D FOT imaging (Li et al., 2011). Besides, they have proposed a fiber-based video-rate FDOT with preclinical NanoSPECT/CT system (Bioscan, Inc.) for combined optical and nuclear imaging of sentinel lymph nodes (Solomon et al., 2011). Garofalakis et al (2010) have proposed a method, using a dual-labeled Oligonucleotide, to image and calibrate the quantity and localization of a probe provided by free-space fDOT with PET and CT. This study has demonstrated a strong linear correlation (($r(2) = 0.95$)) between free-contact fDOT and PET for probe concentrations ranging from 3nM to 1μM in a deep-seated organ, and quantified the sensitivity of fDOT in a range of nM (Garofalakis et al., 2010).

3.2 Materials

The imaging system used in this study for PET and fDOT acquisition are

respectively the Focus 220 MicroPET scanner (Siemens, Knoxville, USA), and the 3D optical imager TomoFluo3D (Cyberstar, Grenoble, France) (shown in Figure 3-1) with a mouse support on which four fiducial marker are fixed.

The TomoFluo3D tomograph (Cyberstar, Grenoble, France) is composed of a high sensitivity CCD camera and a laser source (690 nm, 26 mW, Powertechnology) coupled to translation stages. The system is also equipped with excitation filters on a filter wheel allowing selection of the wavelength of transmission light. Moreover the tomography is equipped with an extra oblique green planar laser, giving access to the animal's surface (Boutet et al., 2011).

The Focus 220 MicroPET scanner provides high sensitivity and high-resolution image of small animal ranging from large rodents to small non-human primates. The PET reconstructions were performed using the MicroPET Manager software (Siemens-Concorde Microsystems), using Fourier rebinning and two-dimensional ordered-subsets expectation maximization (2D-OSEM). The attenuation correction was performed by the PET transmission measurements. Transmission scans are necessary for estimating the attenuation correction factors (ACFs) to yield quantitatively accurate PET emission images. The dimensions of reconstruction volumes were 256 x 256 x 95 with a voxel size of 0.475 x 0.475 x 0.796 mm3. The counts were decay-corrected and expressed in Bq/cc.

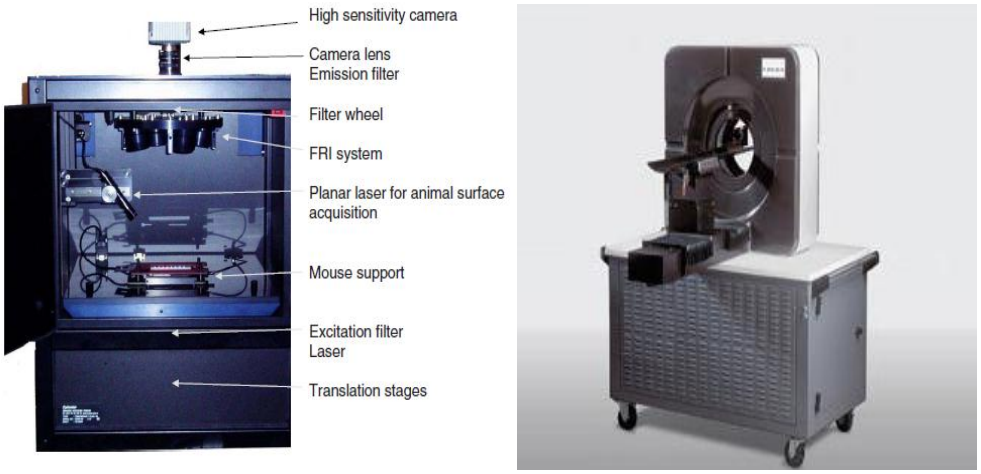


Figure 3-1: The imaging instruments used in this study. Left: the 3D optical imager TomoFluo3D (Cyberstar, Grenoble, France); Right: Focus 220 MicroPET scanner

(Siemens, Knoxville, USA)

The fiducial markers (FM) used in this work were four Plexiglas cubes of 1cm*1cm*1cm containing a source of germanium-68 (74 kBq, 1mm diameter and 0.5mm length; Isotop Product Laboratories, Valencia, USA) originally designed for PET-CT co-registration. The germanium-68 is an isotope of germanium with a half-life time of 270 days, hence it can provide adequate radioactive signals in PET images for a relative long period of time.

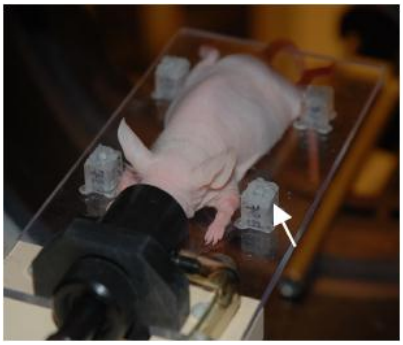


Figure 3-2 Plexiglas cubes containing sources of germanium-68 are fixed in close position to the animal on the mouse supporting plate (Arrow)

Concerning the fiducial marker for the optical image, a spot in the order of 2mm diameter was drawn with precaution using standard white liquid corrector (Tipp-Ex®, Bic, Clichy, France) on the top of each Plexiglas cube, exactly above the ^{68}Ge sources. The Tipp-Ex® spots provide a high signal contrast in optical white light image, without interfering with signal coming from the ^{68}Ge. Radioactive ^{68}Ge and the Tipp-Ex® spots on the upper surface transform the Plexiglas cubes into a bi-modal fiducial marker that can be visualized both in PET and fDOT images. These four Plexiglas cubes were then glued permanently to the transparent glass mouse supporting plate at four corners close to the position of the mouse on the plate (Figure 3-2).

3.2.1 Animal models

Animal experiments were performed under an animal use and care protocol approved by the animal ethics committee and conducted in accordance with Directive 2010/63/EU of the European Parliament. Six female nude mice (body weight of ~25

grams) were obtained from Elevage Janvier (Le Genest Saint Isle, France) and received a subcutaneous injection in the flank of 106 PC12-MEN2A cells (Michiels et al., 1997). The mice were anesthetized by continuous gaseous anaesthesia (1-2% isoflurane in O2) and imaged sequentially by fDOT and PET.

3.2.2 Imaging probes

The near-infrared (NIR) fluorescent dye Sentidye® (20 nmol; Fluoptics, Grenoble, France) was injected three hours before starting the fDOT acquisition. [18F]2-deoxy-2-fluoro-D-glucose (FDG) (7400 kBq; Flucis, IBA) was administered one hour before the PET scan. Each mouse underwent a 20-minute fDOT acquisition followed by a 30-minute PET acquisition. During the transfer from fDOT to PET instruments, the animal was kept under anaesthesia and care was taken to avoid movement of the animal on the supporting plate.

3.3 Method- Image Acquisition

3.3.1 Acquisition of the Optical Images

The fDOT system used in this work consisted of a free spacing system avoiding animals being restrained between two glass plates. To obtain the position of the FM, two optical images covering both the subject and the FM were acquired with the mouse placed in the prone position: (i) a planar white light image recorded from a camera snapshot yielding the x and y coordinates (Figure 3-3, left); and (ii) an image of the 3D surface (the optical surface image) of the animal, acquired by rapid consecutive camera shootings during axial scanning with an inclined green planar laser of the TomoFluo3D, yielding the z coordinate (Figure 3-3, middle).

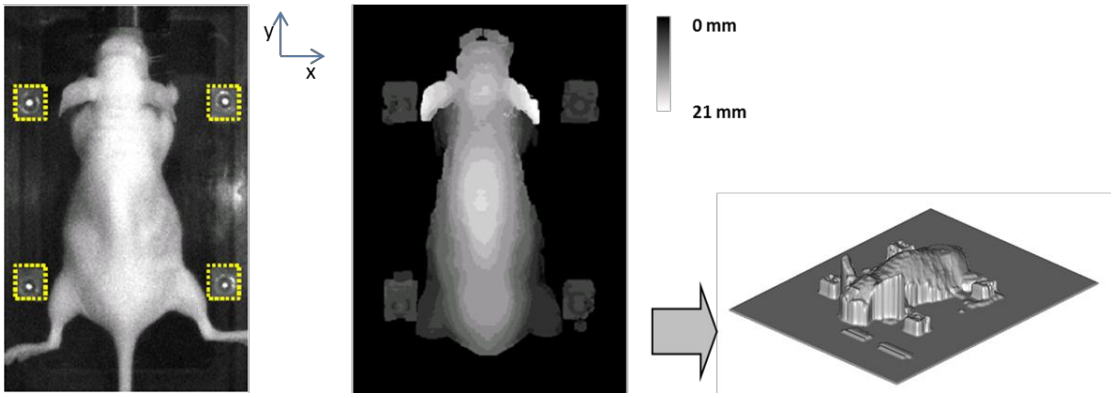


Figure 3-3: optical images acquired by fDOT system. Left: planar white light image (yellow squares refer to the region of detection). Middle: optical surface images. Image on the right serves to represent in altitude the grey-scale value of the optical surface image.

3.3.1.1 Optical surface extraction

The system is equipped with an extra oblique green planar laser connected with the x translation stage (Figure 3-4), which allows extracting the surface of the animal with green light and the maximum intensity distribution of the green light remains localized near the incidence point of the mouse skin.

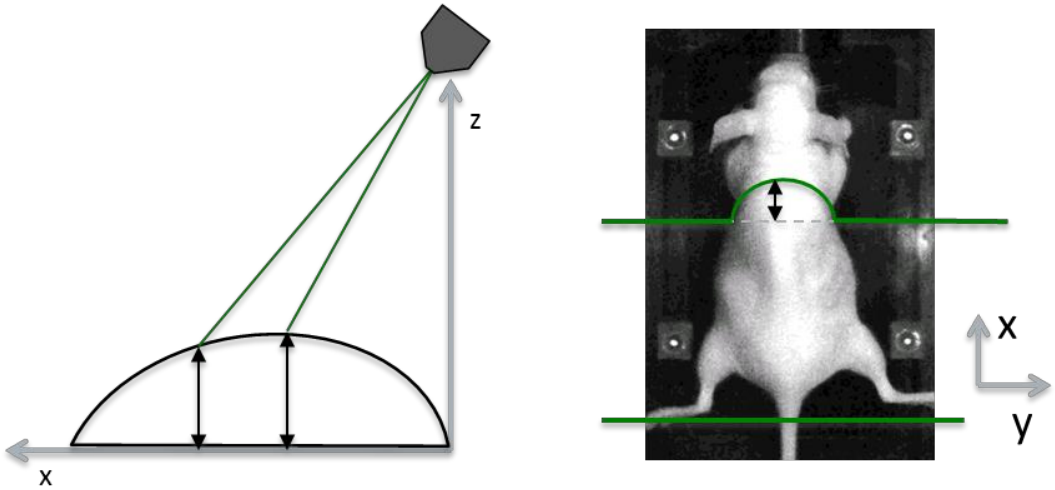


Figure 3-4: Scheme of the surface extraction technique: oblique green planar laser connected with the x translation stage, allows extracting the surface of the animal with green light.

According to Koenig et al (2010), at a given x position, the intersection curve

between the laser plane and the studied object is acquired by the top camera. The intersection is linearly distorted along the x-axis depending on the height of the intersection. The object surface is recovered using the triangulation formula, with the condition that no region is in the shadow of the planar laser. This information about the object surface is then recorded on the optical surface image, with the value of the intensity equivalent to the altitude of the object's surface. This technique has been validated by Koenig et al in using a staircase phantom (Koenig et al., 2010).

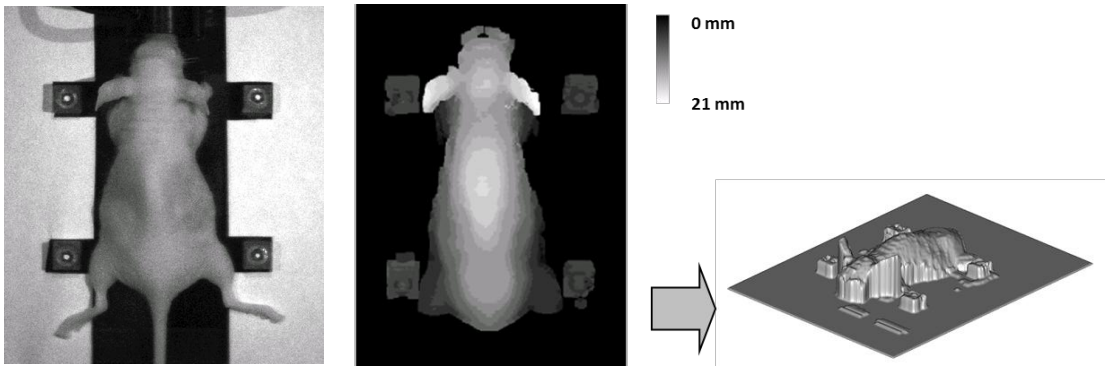


Figure 3-5: Example of the optical surface image extraction. Right: white light image acquired during image acquisition with the use of white paper; Middle: opical surface image with grey scale intensity representing the altitude of the surface. Right: Envelop of the mouse and the FM reconstructed with the optical image surface.

Care was taken to obtain a smooth surface image. The exposure time was adjusted to tens of milliseconds in order to obtain a good contrast between the subject and its surrounding plane surface. This included the use of white paper placed around the object to intensify the reflection of the laser in the surrounding area (Figure 3-5, left). The mouse and the four fiducial markers are both present in the optical surface image (Figure 3-5, middle), with the differences in gray level representing the differences in surface altitude. From this image, it is possible to reconstruct the 3D surface envelope or the mesh of the mouse (Figure 3-5, right) by constructing a stack of binary image with each value of the altitude from the surface image, and then to concatenate these images into a 3D volume taking in account the resolution in z direction. This process has been integrated into the Brainvisa image processing software (http://brainvisa.info/index_f.html) (Cointepas et al., 2001).

3.3.1.2 Acquisition of 3D fluorescent Images

As presented previously, the optical surface image is acquired using a tiled planar green laser, which is implemented on the TOMOFLUO3D system (Figure 3-4) and scans in a linear horizontal movement over the top of the subject. During the acquisition, one temporary image was recorded for each green laser position during laser scanning of the animal, and all images were then integrated into a single image (Koenig et al., 2010). A surface image of the animal was then reconstructed from the intersection curve between the surface of the animal and the surface of the supporting plate by triangulation (Koenig et al., 2010).

The 3D fluorescent fDOT image was obtained by a 20-minute scan of a defined volume of interest covering the region of interest, using excitation by a 680nm laser on the anterior side of the animal (Koenig et al., 2010) and recording with a CCD camera facing its dorsal side. The scanning grid consisted of 7×6 sources in steps of 2 mm and the detection area was 15×13 mm^2. A 2×2 binning was applied to the fluorescent image. The mesh volume corresponding to the detection area was mathematically discretized in voxels of 0.67×0.67×1 mm^3 size to build the reconstruction mesh volume. Finally, the inverse problem of the tomographic reconstruction was solved with the Algebraic Reconstruction Technique (Koenig et al., 2010).

3.3.2 PET Image Acquisition

A 30-min scan was acquired in a Focus 220 MicroPET scanner (Siemens, Knoxville, USA). Image acquisition and reconstruction used the MicroPET Manager software (Siemens-Concorde Microsystems). Image reconstruction was performed using Fourier rebinning and two-dimensional ordered-subsets expectation maximization (2D-OSEM).The attenuation correction was performed by the PET transmission measurements. Transmission scans are necessary for estimating the attenuation

correction factors (ACFs) to yield quantitatively accurate PET emission images. Attenuation map was segmented in three compartments, the soft tissue, the bones and the mouse support plate, and corresponding attenuation coefficients have been attributed at each tissue. The dimensions of reconstruction volumes were 256 x 256 x 95 with a voxel size of 0.475 x 0.475 x 0.796 mm^3. The counts were decay-corrected and expressed in Bq/cc.

3.4 Method - Image co-registration

3.4.1 Theory of the image co-registration

Image registration is the process that precisely overlays two or more than two images of the same area through the geometrical fusion of common features or control points identified in each image. The image to which a transformation will be applied is referred to as the target image while the image that serves as a reference is referred to as the “reference” or “source” image. The images can be taken at different times, from different viewpoints or by different imaging systems. Therefore, image registration techniques normally can be grouped into four categories: multi-model registration, template registration, multi-viewpoint registration and multi-temporal registration. In the present thesis where information of different imaging modalities will be fused, only the first category is considered.

Image co-registration or image alignment algorithms can be classified into intensity-based and feature-based (McLaughlin et al., 2002; Teverovskiy et al., 2007). Intensity-based methods compare intensity patterns in images via correlation metrics, while feature-based methods find correspondence between image features such as points, lines, and contours. Feature-based methods (Boda, 2009) establish a correspondence between a number of especially distinct points in images. With the aid of this correspondence, a transformation is then determined to map the target

image to the reference image, thus establishing a point-by-point correspondence between the reference image and target image. In a more detailed way, Brown et al. has also classified the registration algorithms into four approaches: frame based, point landmark based (using external and/or internal landmarks), surface based and voxel based (Brown, 1992). In voxel-based registration, the mutual information-based registration approach is one of the most commonly used method for registration of multimodal images in medical imaging (Pluim et al., 2003). It begins with the estimation of the joint probability of the intensities of corresponding voxels in the two images.

Point landmark and surface based registration algorithms are typically used for the alignment of anatomical scans, while voxel similarity based registration algorithms seem to be more robust for alignment involving functional scans, although surface based registration algorithms is also used in the latter case. A point landmark can be a fixed geometrical point that is called a fiducial: this is the way that the co-registration has been performed in the present thesis.

3.4.1.1 Rigid body registration/ rigid transformation and non-rigid registration

In clinical and preclinical study, depending on the application and regions of the body involved, the image registration can been performed using two general approaches: rigid or non-rigid registration, according to the transformation models they use to relate the target image space to the reference image space.

Rigid body registration is a fundamental task in three-dimensional (3-D) medical image processing that serves to align two or more 3-D scans taken at a different time, or generated using different medical imaging modalities (Ashburner and Friston, 2004). It is one of the simplest forms of image registration. Rigid body registration involves simple geometric transformations (rigid transformation) such as translation and rotation, to match the two image data sets (Eggert et al., 1997). In other words,

fusion of the two images is performed by finding the rotations and translations that optimize common information provided by the images, which generally involves matching the images by minimizing the sum of squared difference between them. These techniques have been successfully applied to brain studies (Myers and Hume, 2002), and are routinely used in clinical and research settings.

Translations

If a point x is to be translated by q units, then the transformation is simply:

$$y = x + q \qquad \textbf{Eq. 3-1}$$

In matrix terms, this can be considered as:

$$\begin{bmatrix} \mathbf{y_1} \\ \mathbf{y_2} \\ \mathbf{y_3} \\ \mathbf{1} \end{bmatrix} = \begin{bmatrix} \mathbf{1} & \mathbf{0} & \mathbf{0} & \mathbf{q_1} \\ \mathbf{0} & \mathbf{1} & \mathbf{0} & \mathbf{q_2} \\ \mathbf{0} & \mathbf{0} & \mathbf{1} & \mathbf{q_3} \\ \mathbf{0} & \mathbf{0} & \mathbf{0} & \mathbf{1} \end{bmatrix} \begin{bmatrix} \mathbf{x_1} \\ \mathbf{x_2} \\ \mathbf{x_3} \\ \mathbf{1} \end{bmatrix} \qquad \textbf{Eq. 3-2}$$

where (q_1, q_2, q_3) corresponds to the translation in x, y, z from point (x_1, x_2, x_3) to point (y_1, y_2, y_3).

Rotations

In two dimensions, a rotation is described by a single angle. Consider a point with coordinates (x_1; x_2) on a two dimensional plane. A rotation of this point to new coordinates (y_1; y_2), by θ around the origin, can be generated by the transformation:

$$\begin{aligned} \boldsymbol{y_1} &= \mathbf{cos}(\boldsymbol{\theta})\, \boldsymbol{x_1} + \mathbf{sin}(\boldsymbol{\theta})\, \boldsymbol{x_2} \\ \boldsymbol{y_2} &= -\mathbf{sin}(\boldsymbol{\theta})\, \boldsymbol{x_1} + \mathbf{cos}(\boldsymbol{\theta}) \boldsymbol{x_2} \end{aligned} \qquad \textbf{Eq. 3-3}$$

This is an example of the rotation in a rigid transformation. For the three dimensional case, there are three orthogonal planes that an object can be rotated in. These planes of rotation are normally expressed as being around the axes. A rotation of q_1 radians about the x axis is normally performed by:

$$\begin{bmatrix} \mathbf{y_1} \\ \mathbf{y_2} \\ \mathbf{y_3} \\ \mathbf{1} \end{bmatrix} = \begin{bmatrix} \mathbf{1} & \mathbf{0} & \mathbf{0} & \mathbf{0} \\ \mathbf{0} & \boldsymbol{cos}(\boldsymbol{q_1}) & \boldsymbol{sin}(\boldsymbol{q_1}) & \mathbf{0} \\ \mathbf{0} & -\boldsymbol{sin}(\boldsymbol{q_1}) & \boldsymbol{cos}(\boldsymbol{q_1}) & \mathbf{0} \\ \mathbf{0} & \mathbf{0} & \mathbf{0} & \mathbf{1} \end{bmatrix} \begin{bmatrix} \mathbf{x_1} \\ \mathbf{x_2} \\ \mathbf{x_3} \\ \mathbf{1} \end{bmatrix} \qquad \textbf{Eq. 3-4}$$

Similarly, rotations along the y and z-axes are carried out by the following

matrices:

$$\begin{bmatrix} \cos(q_2) & 0 & \sin(q_2) & 0 \\ 0 & 1 & 0 & 0 \\ -\sin(q_2) & 0 & \cos(q_2) & 0 \\ 0 & 0 & 0 & 1 \end{bmatrix} \text{ and } \begin{bmatrix} cos(q_3) & sin(q_3) & 0 & 0 \\ -sin(q_3) & cos(q_3) & 0 & 0 \\ 0 & 0 & 1 & 0 \\ 0 & 0 & 0 & 1 \end{bmatrix} \quad \textbf{Eq. 3-5}$$

Rotations are combined by multiplying these matrices together in the appropriate order.

In mathematics, a rigid transformation is a transformation from a Euclidean space to itself that preserves distances between every pair of points. As mentioned the rigid-body transformation consists of only rotations and translations. They are a subset of the more general affine transformations (Davis et al., 1995). All rigid transformations are affine transformations. Affine transformation includes Translation, geometric contraction, expansion, dilation, reflection, rotation, shear, etc. The affine transformation has more degrees of freedom than the rigid transformation.

Over decades, the solutions to the image registration problem have become more complicated. However, when applied to regions of the body that can bend and where flex geometric relationships between different anatomic regions might be affected by the shape of the studied subject, the orientation of the body and also the respiratory state etc., the image registration process might result in good matching of only one particular region of a patient's anatomy and not necessarily to that of the whole scanned region.

The drawback of rigid body transformation is that it tends to ignore organ deformation owing to issues discussed previously (differences between shapes of the gantry bed, internal organ shift, respiratory motion, and so forth). To address these limitations, non-rigid registration algorithms that permit compensation for perceived organ deformation for different modalities have been proposed.

Non-rigid registration has been introduced as a technique to improve registration accuracy over a larger region of a patient's body (Crum et al., 2004a; Rueckert and Aljabar, 2010). It is generally used in computer vision for document analysis and image recognition. It involves more complicated and sophisticated algorithms than the

rigid transformation, and often demands large amounts of data set computation. Software-based non-rigid image registration is challenging and time consuming in most cases (Saxena et al., 2010), thus limiting its use to academic institutions with advanced technical support that can accommodate the requirements of these procedures and perform scanning with both modalities on the same day using carefully matched anatomic positioning and respiration protocols.

However, robust multimodality image registration for small-animal imaging remains challenging and likely will continue to be an active research field for years to come. In this work, the studies involve only rigid transformation, and non-rigid transformation thus has not been introduced in detail here.

3.4.1.2 Fiducial marker based registration

As discussed previously, image registration techniques have been developed to co-register images of different imaging modalities. The result of the co-registration algorithms is a transformation matrix that allows the co-registration of one image into another one. The first step for the calculation of the transformation matrices is the identification of reference points visible by each modality. These landmarks are called fiducials.

A fiducial marker or fiducial is an object used for multimodal imaging system that appears in each image produced as a point of reference or a point of measurement. It may be either something placed into or on the surface of the subject, in the form of either one or a set of landmarks. Images of the same subject produced with two different imaging systems may be correlated by placing fiducial markers in the area imaged by both systems. Therefore, it is necessary to make sure that the marker is visible in the images produced by both imaging modalities.

Fiducial markers are used in a wide range of medical imaging applications (Wang et al., 1996; Nahrendorf et al., 2009). For example, functional information from SPECT or PET has been related to anatomical information provided by MRI (Stout and Zaidi,

2008). Moreover, adhesive markers on the skin are widely used for image registration (Wang et al., 1996), with the centers of these markers serving as fiducial points in registration. It is important that a clearly recognizable fiducial point is defined in images of both modalities. Many studies have been done in order to propose algorithms to detect the fiducial point in multimodal images (Wang et al., 1996; West et al., 1997; Fitzpatrick et al., 1998). For modalities such as CT, PET, SPECT and MRI, the position of the fiducial can be selected manually, semi-automatically or automatically.

For preclinical studies, some co-registration techniques use external fiducial markers that are visible in the datasets. Those techniques have been widely used for dual-modality image registration with CT, PET or MRI (Nahrendorf et al., 2009; Nelson et al., 2011). However, most of the existing studies using the fiducial marker based co-registration in preclinical field are achieved manually. Challenges remain in the development of automatic fiducial marker based co-registration method serving for preclinical application.

3.4.2 Fiducial markers method for FDOT

Methods for the automatic identification of the FM's coordinates have been developed for co-registration of CT, PET and MRI modalities (Wang et al., 1996; Fitzpatrick et al., 1998; Liu, 2003; Yang et al., 2006)

However, so far these methods have not been adapted to image co-registration with fDOT because fDOT reconstructions are spatially restricted and do not cover the FM that is usually placed in close vicinity to the subject. There are some limitations that characterize fDOT acquisition and do not allow the parallel reconstruction of the organ signal and the FM signals. In fDOT, the laser beam is restricted to areas of high scattering, i.e the tissue, and fDOT is not suitable to image a disconnected FM source. Moreover, since the acquisition time of the fDOT is relatively long, the scanning area

is limited to the region of interest (ROI) and the scanning of multiple regions in the field of view of the CCD camera is a time consuming process. In figure 3-6, an example of the fDOT reconstruction is shown, this example illustrates that the fluorescent signal is restricted only to the region of the kidneys, excluding the area of the fiducial marker.

Accounting with the particularity of preclinical molecular imaging in terms of image resolution and size of the animal, a feasible and efficient co-registration method is essential to the image fusion of the two modalities. Previous studies used CT as an anatomical referential to co-register optical images with the PET image (Garofalakis et al., 2010; Nahrendorf et al., 2010). In our study, a new method has been proposed that directly and automatic all co-registers fDOT with PET. Our method has taken into account the particularities of fDOT, i.e. its capacity for surface extraction.

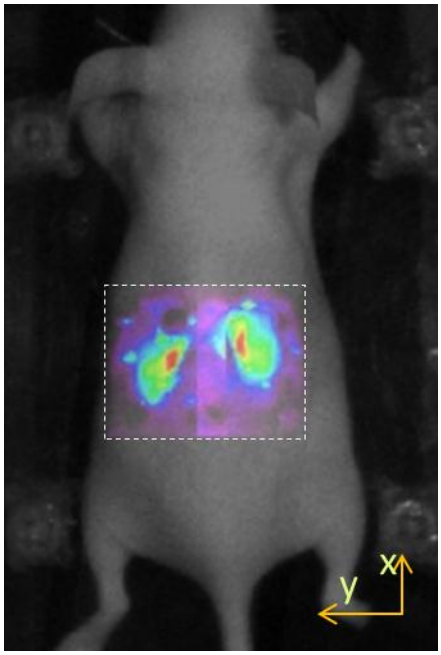


Figure 3-6: example of a fDOT reconstruction (rainbow color) is presented overlapping with the mouse white light image. Four cubes of fiducial markers are located in close position but disconnected to the mouse body.

3.4.3 Co-registration of fDOT image with PET image

As presented previously, the fDOT reconstruction is a local image of the region of interest and does not include the region of the fiducial markers. In order to co-register the regional fDOT reconstruction to the whole-body PET image, the co-registration is a combination of two steps, co-registration of the fDOT reconstruction to the planar white light image, and co-registration of the planar white light image to the PET image.

The three optical images (white light photo, surface and fDOT reconstruction) were acquired in the same spatial referential under the same fDOT imaging system and in the same imaging session. The field of view of the CCD camera holds the panorama of the mouse body and the FMs around it, and was recorded in the planar white light image. The region of interest refers to the scanning area of the laser source, which is defined by the user according to the FOV of the CCD camera. It also defined the relative position of the fDOT reconstruction image with respect to the white light image. Figure 3-6 shows the relative position of the fDOT image in the white light image.

The position of the fDOT reconstruction area is defined a priori according to the planar white light image. The transformation matrix between the fDOT image and the white light image $T_{fDOT-photo}$ is (Figure 3-6) calculated using the intrinsic parameters of the fDOT system (image dimension, coordinates of the defined region of interest, etc.). The fiducial marker based method presented in the following section is used to co-register the planar white light image with the PET image $T_{photo-PET}$. Finally, to co-register the fDOT fluorescence reconstruction with the whole body PET image, the two previous steps are combined and the $T_{fDOT-PET}$ transformation matrix for fDOT to PET co-registration is calculated as the product of $T_{fDOT\ \ photo}$ and $T_{photo-PET}$:

$$T_{fDOT-PET} = T_{fDOT-photo} \times T_{photo-PET}$$ **Eq. 3-6**

The co-registration of the planar white light image to the PET image ($T_{photo\text{-}PET}$) was performed in 4 steps.

3.4.3.1 Detection of the optical planar (x, y) FM Coordinates

The planar white light image is used to identify the optical planar coordinates of the FM. The Tipp-Ex® spot drawn on the top of each Plexiglas cube indicates the planar position of the FM in optical white light images. Four Regions of Detection (ROD) were assigned onto predetermined positions in the planar white light image (Figure 3-7). These regions can be squares, rectangles or circles, according to the shape of the FM included inside the ROD. Here, as our FM is a cubic object, the RODs were defined as four squares around the FM. Each ROD had a size of 6mm x 6mm, corresponding to 30x30 pixels in the concatenated mouse photograph, i.e. three times larger than the Tipp-Ex® spots' dimensions. This size of the ROD is chosen in order to obey the Nyquist–Shannon sampling theorem (Marks, 1991) for the following image processing step (given the dimension of the ROD as the largest bandwidth, the sampling should be at least twice larger than the bandwidth), while avoiding too large RODs that may induce parasite signals from the mouse body.

The first step consisted in the automatic detection of the x and y coordinates of the FM based on the maximal intensity inside the corresponding RODs (Figure 3-7). Three image pre-processing steps were firstly performed successively: (i) filtering with a 3x3 median filter that eliminated most of the noise present in the RODs, as the median filter is used to eliminate the noise present in the image while preserving the edge of the subject; (ii) high-pass thresholding of image pixel intensities at a threshold value of 90% of the maximum intensity, so that it eliminates the low intensity signal inside the RODs; (iii) application of a Deriche's recursive Gaussian filter (Deriche,

1993) in order to center the gradient intensity change in the filtered image of the Tipp-Ex® spots. Following these three steps, the coordinates of the local maximum intensity in each ROD coincided with the center of the FM signal given by the Tipp-Ex® spots in the planar white light image and this position was assigned as the planar coordinate (x_{opt}, y_{opt}) of the FM.

3.4.3.2 Detection of the optical altitude (z) FM coordinates

The optical surface image and the planar white light image were acquired with the same fDOT apparatus and the same field of view. These two images were concatenated into the same orientation and the same pixel size, the (x, y) coordinates in both images inter-correspond directly. The planar coordinates (x_{opt}, y_{opt}) of the FM identified previously were then relocated to the optical surface image. The intensity values of the optical surface image, representing the distance between the upper surface of the FM and the supporting plate were then measured at position (x_{opt}, y_{opt}) to yield the corresponding $z0_{opt}$ value of the upper surface of the FM. Altogether, the combination of the optical surface image and the planar white light image allowed assigning full 3D coordinates (x_{opt}, y_{opt}, $z0_{opt}$) to each FM in the optical image.

3.4.3.3 Detection of PET FM coordinates

As the PET image is a 3D volumetric image that presents all the x, y and z information, four 3D RODs of 9 mm^3 dimension (three times larger than the dimension of the FM signal in the PET image) were defined in the PET volume image (Figure 3-7). Following completion of the same image pre-processing steps as for the detection of the optical planar coordinates (median filtering, thresholding and Gaussian filtering), the local maximum was identified in each ROD to yield directly the coordinates (x_{PET}, y_{PET}, z_{PET}) of the FM in the PET volume image.

Since signals of the FM from the optical and PET images do not coincide in the z dimension (i.e. the optical signal is on the top of the Plexiglas cube, and the PET signal given by the ^{68}Ge is inserted inside the cube), a distance dz, which is half the length (Z dimension) of the Plexiglas cube, was added to account for translation in the z direction after the calculation of the rigid transformation matrix between the optical and PET images.

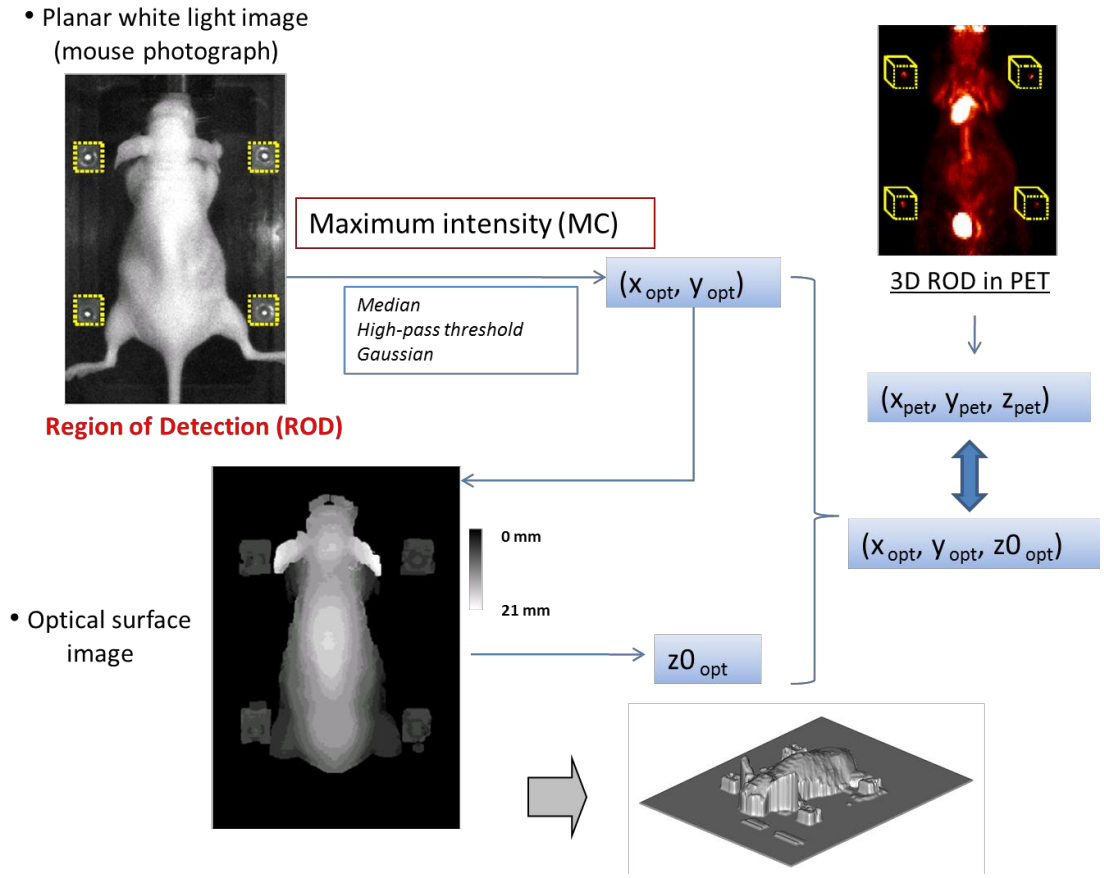


Figure 3-7: Schematical framework of the FM coordinates detection in optical images and PET image. The planar white light image is used to calculate the x and y coordinates of the optical image; the z coordinate detected with the optical surface image using the x and y previously calculated. The 3D coordinates of FM in the PET image (x_{pet}, y_{pet}, z_{pet}) can be extracted directly from the PET image; the coordinates (x_{pet}, y_{pet}, z_{pet}) and (x_{opt}, y_{opt}, $z0_{opt}$) of both modalities are used to calculate the rigid transformation.

3.4.3.4 Transformation from the planar white light image to the PET volume image

A rigid transformation with translation and rotation was calculated to co-register the optical and PET coordinates of the FM. With Po= {Po1, Po2, Po3, Po4} and Pp= {Pp1, Pp2, Pp3, Pp4} being the four FM positions in the optical and the PET volume images, respectively, the translation T and rotation R were defined as;

$$T = \begin{bmatrix} T_x \\ T_y \\ T_z \end{bmatrix} \qquad \textbf{Eq. 3-7}$$

$$R = \begin{bmatrix} R_{11} & R_{12} & R_{13} \\ R_{21} & R_{22} & R_{23} \\ R_{31} & R_{32} & R_{33} \end{bmatrix}$$

And

$$Pp = R * Po + T \qquad \textbf{Eq. 3-8}$$

The algorithm to compute the transformation [R, T] used the singular value decomposition (SVD) (Eggert et al., 1997) approach to find the least square error criterion (Eq. 3-9),

$$\sum_{i=1}^{N} E = \sum_{i=1}^{N} \left\| Ppi - \left(RPoi + T\right) \right\|^2 \text{ , (where N =4 is the number of FM.)} \qquad \textbf{Eq. 3-9}$$

The point sets $\{Pp_i\}$ and $\{Po_i\}$ were imposed the same centroid to calculate the rotation:

$$\overline{Pp} = \frac{1}{N}\sum_{i=1}^{N} Pp_i \qquad \hat{P}p_i = Pp_i - \overline{Pp}$$

$$\overline{Po} = \frac{1}{N}\sum_{i=1}^{N} Po_i \qquad \hat{P}o_i = Po_i - \overline{Po} \qquad \textbf{Eq. 3-10}$$

Rewriting and reducing equation (Eq. 3-9):

$$\sum_{i=1}^{n} E = \sum_{i=1}^{N} \left\| \hat{P}p_i - \hat{R}\,\hat{P}o_i \right\|^2$$
$$= \sum_{i=1}^{N} \left(\hat{P}p_i^T\ \hat{P}p_i + \hat{P}o_i^T\ \hat{P}o_i - 2\hat{P}p_i^T\ \hat{R}\,\hat{P}o_i \right)$$

Eq. 3-11

Transformation was expressed as:

$$\hat{T} = \overline{Pp} - \hat{R}\,\overline{Po}$$

Eq. 3-12

The $[\hat{R}, \hat{T}]$ is the optimal transformation that maps the set {Pp_i} to the {Po_i}. Equation (Eq. 3-11), also known as the orthogonal Procrustes problem (Eggert et al., 1997; Gower and Dijksterhuis, 2004), s minimal when the last term $2\hat{P}p_i^T\ \hat{R}\,\hat{P}o_i$ is maximal.

The optical images is proportionally larger than the PET images, due to (i) the difference in the pixel size between the optical planar image (0.21mm x 0.21mm) and the PET image (0.47mm x 0.47mm); and (ii) to the parallax induced by the camera detecting the Tipp-Ex® spots from the upper surface of the cube. Therefore a scaling factor was applied additional to the rigid transformation matrix, so that the FMs in the PET image are well overlapped with the FMs in the optical image. The scaling matrix including the scaling factor of the three axes was then integrated into the rotation matrix. The value of this scaling factor was calculated with the average distance of the points in the x and y axes between the two modalities as (do_x, do_y) and (dp_x, dp_y):

$$do_x = \left[\left(Po_2(x) - Po_1(x) \right) + \left(Po_4(x) - Po_3(x) \right) \right] / 2$$
$$dp_x = \left[\left(Pp_2(x) - Pp_1(x) \right) + \left(Pp_4(x) - Pp_3(x) \right) \right] / 2$$
$$do_y = \left[\left(Po_3(y) - Po_1(y) \right) + \left(Po_4(y) - Po_2(y) \right) \right] / 2$$
$$dp_x = \left[\left(Pp_3(x) - Pp_1(x) \right) + \left(Pp_4(x) - Pp_2(x) \right) \right] / 2$$

Eq. 3-13

A 3x3-scaling matrix was then built:

$$S = \begin{bmatrix} S_x & 0 & 0 \\ 0 & S_y & 0 \\ 0 & 0 & S_z \end{bmatrix}$$

Eq. 3-14

where $Sx = \frac{do_x}{dp_x}$; $Sy = \frac{do_y}{dp_y}$ and $Sz = 1$ (i.e., no scaling in the z direction)

After correcting for distance dz, by adding this value to Z translation $\hat{T}z$, the final transformation matrix $T_{photo\text{-}PET}$ for the optical photograph to the PET volume was:

$$T_{photo-PET} = \begin{bmatrix} \hat{R}S_{11} & \hat{R}S_{12} & \hat{R}S_{13} & \hat{T}x \\ \hat{R}S_{21} & \hat{R}S_{22} & \hat{R}S_{23} & \hat{T}y \\ \hat{R}S_{31} & \hat{R}S_{32} & \hat{R}S_{33} & \hat{T}z \end{bmatrix} \quad \textbf{Eq. 3-15}$$

where RS are the rotation matrix elements R multiplied by the scaling matrix elements S of (Eq. 3-14).

Applying matrix (Eq. 3-15) to the optical white light image (Figure3-8. f) aligned the 3D PET image (Figure 3-8 g) to yield the co-registered bimodal image shown in Figure 3-8 h.

3.4.3.5 The barycenter-based method

In previous studies (Wang et al., 1996; West et al., 1997; Fitzpatrick et al., 1998), the barycenter-based approach has been used for automatic identification of FMs for CT and MRI imaging. The barycenter-based method calculates the average location of a mass weighted in space. The barycenter was calculated as the center of mass B of a system (i.e. all voxels within the RODs) defined as the average of their positions ri, weighted by their mass mi:

$$B = \frac{\sum m_i r_i}{\sum m_i} \quad \textbf{Eq. 3-16}$$

For the mouse photograph, as the barycenter was calculated in two dimensions, the left upper corner of each ROD was taken as origin and the vector r_i corresponded to the relative position from this origin to each pixel within the ROD. The

signal intensity of each pixel inside the ROD gave the value of m_i. For the PET image, the barycenter was calculated in 3D and the position of the first voxel (left upper in axial view and first section in the z direction) of the 3D ROD taken as the origin. The position of each voxel relative to this point was taken as r_i and the value of each voxel as m_i. The barycenter calculated for each ROD represented the FM's position. The transformation matrix was calculated with the coordinates of the FM detected in the optical image and the PET image using this barycenter based method and compared with our maximum intensity based method. The results of the comparison will be presented in the Results section.

3.5 Results

3.5.1 Co-registration procedure

The general outline of the co-registration method is depicted schematically in Figure 3-8. Five steps are implemented successively: (i) registration of (xopt, yopt, z0opt), i.e. the x, y and z coordinates of the optical fiducial markers using both the white light (Figure 3-8 B) and optical surface (Figure 3-8 c) images; (ii) calculation of $T_{fDOT-photo}$, the transformation matrix from the fDOT reconstruction image to the whole body image; (iii) registration of (x_{PET}, y_{PET}, z_{PET}), i.e. the x, y and z coordinates of the fiducial markers in the PET images (Figure 3-8 d,e); (iv) calculation of $T_{photo-PET}$, the transformation matrix from optical to PET volumes (Figure 3-8 h); and (v) calculation of $T_{fDOT-PET}$, the transformation matrix for the co-registration of the fDOT volumes with the PET volumes.

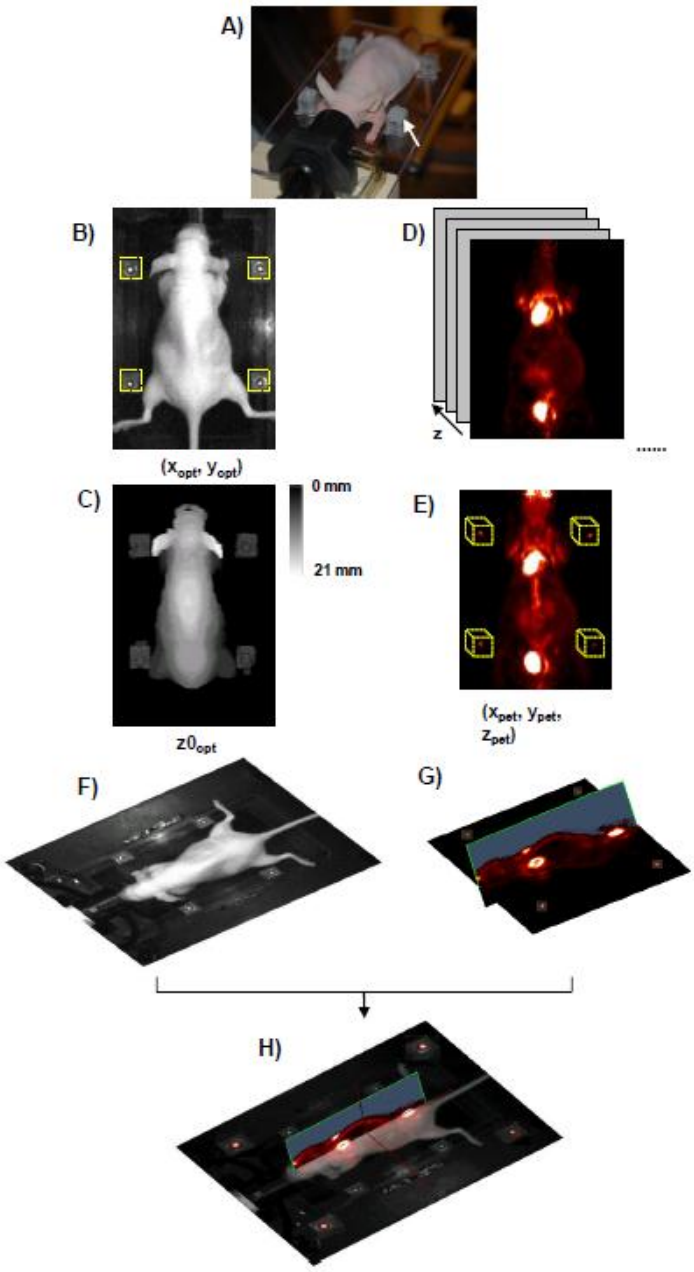


Figure 3-8: General outline of the automatic co-registration method for optical and micro-PET images: (A) View of the multimodality mouse support system showing the four Plexiglas cubes containing the fiducial markers (FM). (B) Planar white light image of the subject used for the extraction of the planar coordinates of the FM. (C) Optical surface image used for the extraction of the z (vertical) coordinates of the FM (z0opt). (D) A stack of coronal PET slices that corresponds to the different z positions. (E) Projection image of the PET volume signal. The localization of the FM where their coordinates correspond to the radiation signal (x_{PET}, y_{PET}, z_{PET}) is highlighted by dotted yellow rectangles (F) Bird's eye view of the optical image of the mouse. (G) Bird's eye view of the micro-PET volume image. (H) Assembled image of the co-registered optical- 3D PET images. The image shows the coronal view of the animal with signals from both modalities while the sagittal view depicts only the PET signal. The signals of

the co-registered FM were zoomed and shown at the four corners of image H.

The complete image processing method was written in C++ and integrated in Python with a user-friendly interface within the Brainvisa image processing software (http://brainvisa.info/index_f.html) (Cointepas et al., 2001). Input files include (i) the mouse photograph, (ii) the optical surface scan, (iii) a header file containing the position of the fDOT image relative to the camera's field-of-view, and (iv) the PET volume image. With this user-friendly toolbox, three transformation matrices ($T_{fDOT\text{-}photo}$, $T_{photo\text{-}PET}$, $T_{fDOT\text{-}PET}$) are calculated and sent as outputs. The program is completed in 20 to 30 seconds on a Dell Precision™ T7500 workstation with a 64-bit Intel® Xeon® quad-core processor.

3.5.2 Quantitative Evaluation of the Co-registration

3.5.2.1 Fiducial Registration Error (FRE)

To evaluate quantitatively the performance of our co-registration method, the Fiducial Registration Error (FRE) (Wang et al., 1996; West et al., 1997; Fitzpatrick et al., 1998) was calculated as the root-mean-square (rms) distance of the positions of the FM in the two image modalities after co-registration, in six independent experiments in six mice. It is a commonly used evaluation factor for the fiducial marker based co-registration. The FRE evaluates the certitude of the overlap between points, taking as landmark the relative distance of the detected markers' position by each modality in the co-registered images.

In the first place, attention was paid to the evaluation of the planar co-registration performance in the x and y planes. Therefore, the FRE in a 2D view was calculated where the white light image co-registered with the PET image, at the same horizontal plane of the FM (Figure 3-8H). In this plane, the FRE of the four FMs in the co-registered image are measured separately and then the mean value of these four FRE values of the four FMs is taken as the final FRE for the planar evaluation.

The errors were calculated in the co-registered images with the distance in pixel units, multiplied by the pixel size of each modality.

$$FRE_{opt-PET}(mm) = \begin{cases} \Delta pixel_{opt} \times pixelsize_{opt} \\ \Delta pixel_{PET} \times pixelsize_{PET} \end{cases} \quad \textbf{Eq. 3-17}$$

The FRE of our maximum intensity method (MI) was compared with that of the manual co-registration (MC) as a reference method, and of the barycenter-based (BC) method (Table 3-2).

FRE (mm)		MC	MI	BC
Optical	Mean	0.279	0.259	0.545
	SD	0.05	0.06	0.11
PET	Mean	0.217	0.256	0.448
	SD	0.09	0.12	0.08

Table 3-2: Fiducial Registration Errors (FRE). MC: Manual Co-registration; MI: Maximal Intensity co-registration; BC: Barycenter-based Co-registration; SD: Standard Deviation of the mean (n=6 for all calculations). All values are in mm.

Due to the differences of the pixel size in the fDOT image (0.212mm2) and the PET image (0.67mm2), individual FRE values were calculated for each modality. Using the BC approach, the FRE was 0.55 ± 0.11 mm (mean ± Standard Deviation; n=6) and 0.45 ± 0.08 mm for optical and PET images, respectively. Using the MI approach the FRE was 0.26 ± 0.06 mm and 0.26 ± 0.12 mm for optical and PET images, respectively. The FRE of the MC approach was 0.28 mm ± 0.05 mm in optical images and 0.22 ± 0.09 mm for PET images. Comparison of the three approaches showed that the MI approach produced average FRE smaller than the BC approach and in the same range as that of the MC approach.

In all cases, statistically significant differences were found between the FRE values of the MI and BC approaches (Student's t test, p=0.0003 and p=0.0007 for optical and PET images, respectively), while no statistically significant differences

were found between the MI and the MC approaches (p=0.51 and p=0.55 for optical and PET images, respectively). Taken together, these results indicate that the MI approach has the same co-registration performance as the MC approach and that both are more precise than the BC approach.

3.5.2.2 Evaluation of Co-registration quality in the z direction

In order to evaluate the co-registration error in the z direction of our MI approach, the mouse envelope reconstructed by the optical surface image was fused with the PET image using the transformation matrix $T_{photo\text{-}PET}$, as both of these volumetric images contain the information of the position of the FM. The average error in the z direction was 0.37± 0.06mm, a value smaller than the voxel size in the z direction (1 mm in optical images and 0.475 mm in PET images). Taking into account the error in the z direction, the 3D FRE value of our MI approach was 0.452 mm for the optical image and 0.446mm for the PET image. These values are smaller than the diagonal of the image voxel for both modalities.

3.5.2.3 Fiducial Localization Error (FLE) and Target Registration Error (TRE)

The Fiducial Localization Error (FLE) represents the root-mean-square error distance between the estimated and the true position of a FM (Wang et al., 1996; Fitzpatrick et al., 1998). It is not easy to measure experimentally the real position of the signal of the FMs, especially for the PET image as its signal is given by the positron-emitting isotope ^{68}Ge during acquisition without indication of precise structural position of the FM. Thus, the FLE was calculated following Eq 3-18, proposed by Fitzpatrick et al using the values of the FRE and the number of the fiducial N (Fitzpatrick et al., 1998):

$$\langle FRE \rangle^2 = \left(1 - \frac{2}{N}\right) \langle FLE \rangle^2 \qquad \textbf{Eq. 3-18}$$

Using the average value of the FRE calculated previously for MI approach (here, n=4), the FLE was 0.35 mm for the PET images and 0.37 mm for the optical images. The FLE values are independent from the fiducial configuration (Fitzpatrick et al., 1998), and when these values were compared with the FRE, it showed that they were smaller than the 3D FRE values. This means that the shape and other physical characteristics of the FM do not influence much the accuracy of the FMs' position identification by the imaging systems. The error of the intra-modality FM detection is smaller than the error of the inter-modality co-registration, which proves that no extra error is added to the co-registration performance due to the localization of the position of the FM for both modalities.

The Target Registration Error (TRE) is defined as the distance after co-registration between the corresponding points in two modalities that not have been used in calculating the co-registration. As the fDOT and PET imaging systems provide both functional images, it is not evident that the images from these two modalities share any common signal distribution in the area other than the FMs. However TRE can be derived mathematically from the mean FRE and FLE according to Fitzpatrick et al (Fitzpatrick et al., 1998):

$$\langle TRE \rangle^2 = \langle FLE \rangle^2 - \langle FRE \rangle^2 \qquad \textbf{Eq. 3-19}$$

The mean TRE was 0.26 mm for optical images and 0.25 mm for PET image. The calculated TRE was similar as the FRE for both modalities, indicating that the co-registration error derived from the FM position and other positions on the image remained coherent. This guarantees the accuracy and the performance of the fDOT /PET co-registration in whole image for both modalities.

3.5.3 In-vivo Co-registration of tumor vascularity and metabolism

The fDOT-to-PET co-registration method was applied to 6 female nude mice bearing tumor xenografts of PC12-MEN2A cancer cells that mimic a human medullar thyroid carcinoma (Michiels et al., 1997). MEN 2 stands for "Multiple endocrine neoplasia type 2" which is a dominantly inherited cancer syndrome that comprises

three clinical subtypes: MEN type 2A (MEN-2A), MEN type 2B (MEN-2B), and familial medullary thyroid carcinoma (FMTC). The majority of MEN2A and FMTC mutations are located in the extracellular domain of the membrane protein RET and cause the replacement of one of five juxtamembrane cysteines by a different amino acid (Michiels et al., 1997).

The diameter of tumors ranged from 4.5 to 8 mm, corresponding to tumor weights of 50-270 mg. Each mouse received two injections, one of the fluorescent probe Sentidye®, a probe that passively accumulates in tumors by virtue of the Enhanced Permeability and Retention (EPR) effect, and one of $^{[18F]}$FDG for tumor visualization with PET. The mouse was imaged sequentially with fDOT and PET. The objective was to find out how these two probes with molecular characteristics interact with the tumor tissue and how they are located one with respect to the other, and moreover to define what complementary information they provide.

The signals of the FDG and the Sentidye have been segmented to allow quantification of the signal. In the case of PET image, a threshold of 30% of the maximum signal in the tumor was applied, while in the case of the fDOT a threshold of 10% of maximum plus a constant value was applied. This constant represents the noise of fDOT reconstructions, which is calculated by dilution of the fluorophore concentration until reaching the limit of fDOT system detection,. The choice of the thresholds was based on the study of Garofalakis et al (2010) on the evaluation of the volumes occupied by the signals of PET and fDOT with CT acting as a reference.

The correlation between total FDG uptake (the average FDG signal multiplied with the volume) of the PET image and the tumor volume measured from PET signal is shown in Figure 3-9. The coefficient of determination R^2 equals to 0.7752, indicating that there was a correlation (R^2>0.7) between the volume of the tumor and the total uptake of FDG. The correlation between the PET tumor volume and the PET signal concentration shown in Figure 3-10 yielded a coefficient of determination R^2 = 0.0811, therefore there was no correlation between the tumor volume and the concentration of FDG in the tumor expressed in percentage of injected dose per cc. In other words, the radioactivity concentration remained independent of the tumor volume.

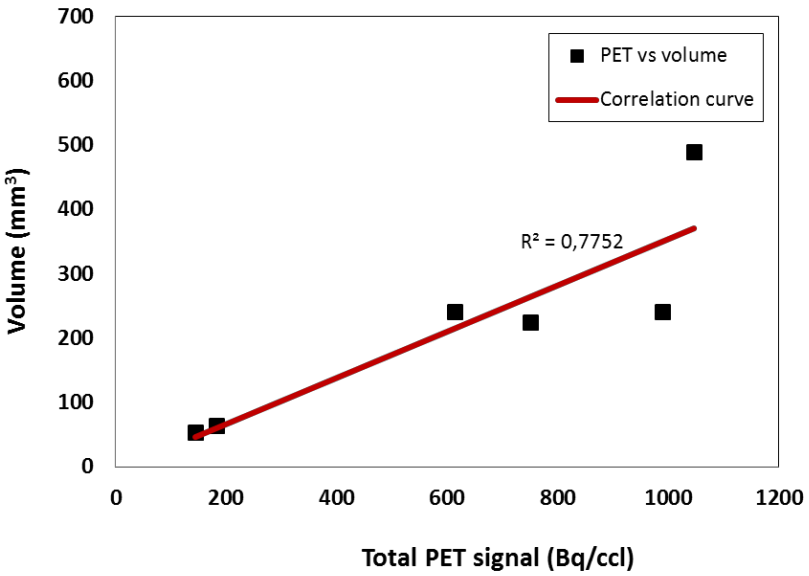


Figure 3-9: The correlation between the total FDG uptake (Total PET Signal expressed in Bq/cc) and the PET volume of the tumor.

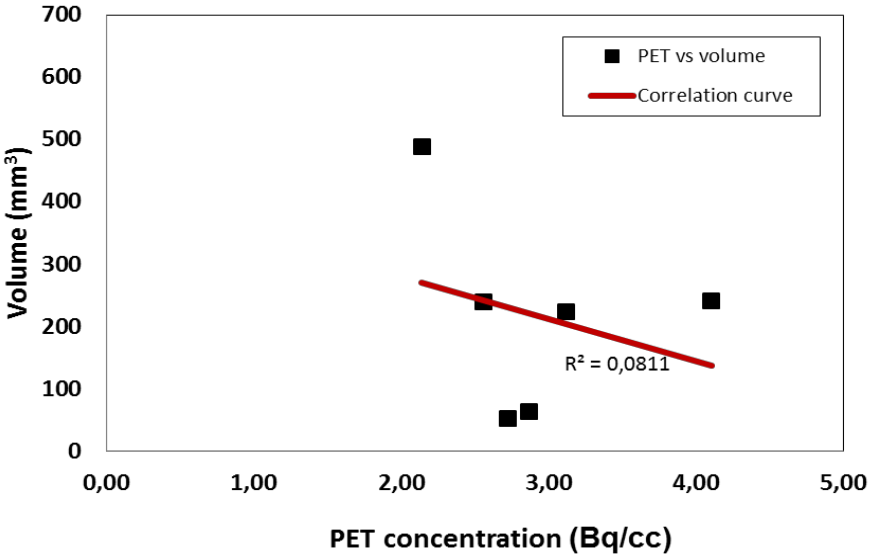


Figure 3-10: The correlation between the PET concentration (Bq/cc) and the PET volume of the tumor.

Besides, the fDOT signal increased with tumor size but plateaued for tumors larger than 150 mg, corresponding to a tumor with a diameter larger than 6 mm. Again,

as shown in figure 3-11 and figure 3-12, no correlation between tumor volume and total fDOT signal and moderate correlation between tumor volume and the concentration of the fDOT signal were found in the tumor area.

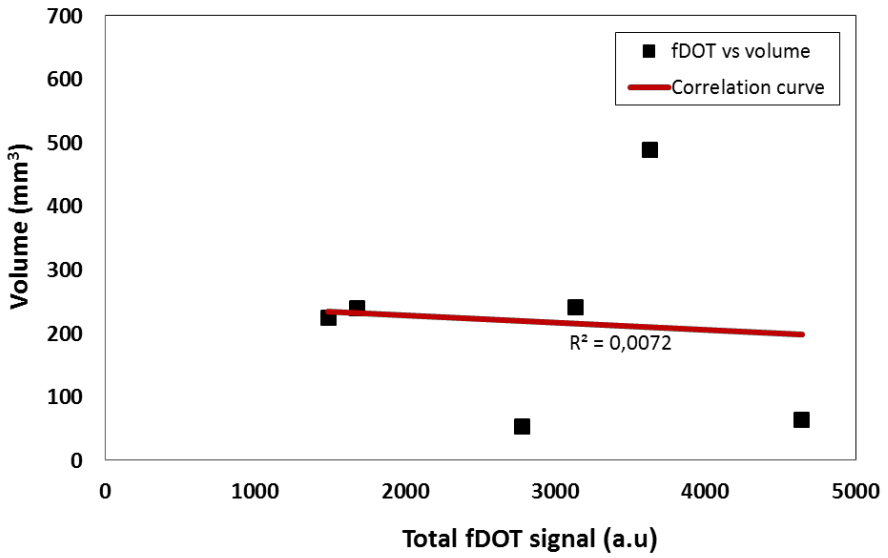


Figure 3-11: The correlation between the total fDOT signal of the Sentidye and the PET volume of the tumor.

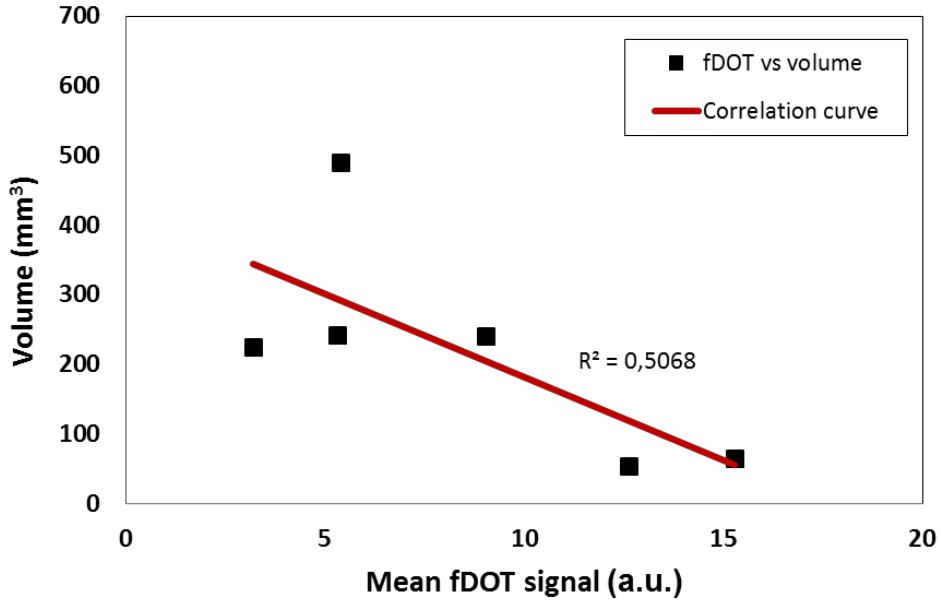


Figure 3-12: The correlation between the concentration of the fDOT signal (mean fDOT signal in arbitrary unit) and the PET volume of the tumor.

The fDOT-PET fused images (Figure 3-13) showed the localization of the optical probe with respect to the glucose consumption of the tumor. After the RODs had been defined for the mouse holder as indicated above, fDOT and PET images were co-registered automatically and the localization of FDG and Sentidye® uptakes were compared directly.

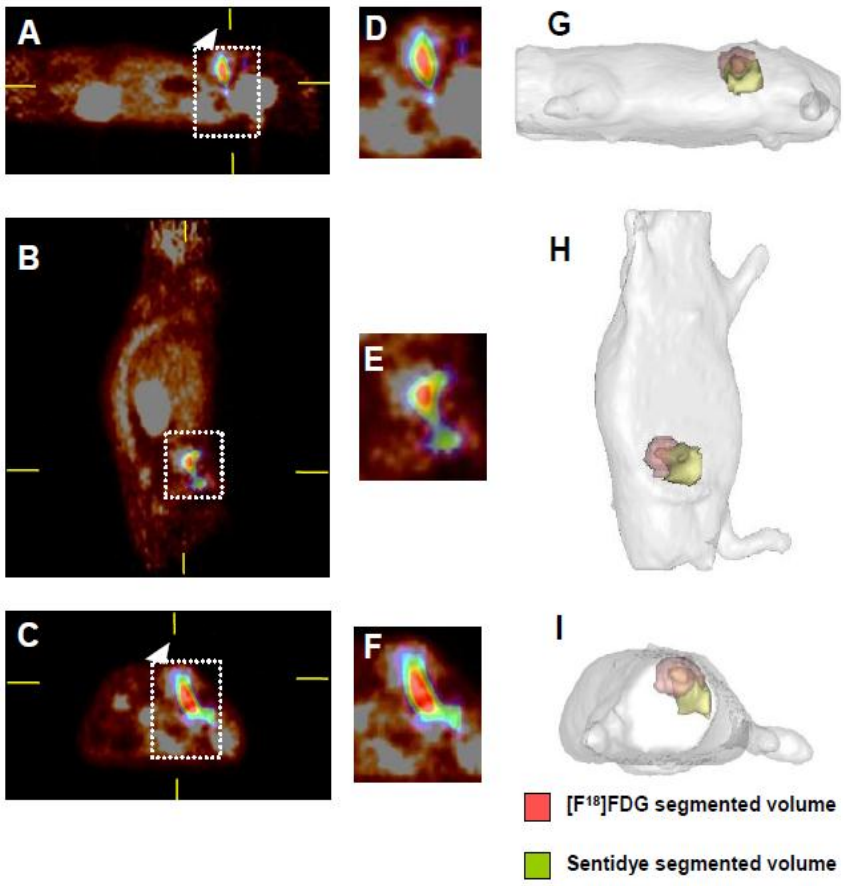


Figure 3-13: Co-registration of fDOT and micro-PET in a mouse bearing a MEN2A tumor xenograft. Left: Fusion fDOT/PET image in the sagittal (A), coronal (B) and axial (C) planes. The corresponding zooming images focus on tumor region in the sagittal (D), coronal (E) and axial (F) planes. Color scales are "temperature" (dark red to brilliant yellow) for PET and "rainbow" (blue to white) for fDOT. The white dotted rectangles point at the reconstruction mesh of the fDOT while the white arrows indicate the position of the tumor. Right: PET and fDOT signals rendered to the envelope of the mouse corresponding to the sagittal (G), coronal (H) and axial (I) projections are shown. Pink volume: [^{18}F]FDG segmented volume inside the tumor; Yellow volume: Sentidye® segmented volume (manual segmentation) inside the tumor. Both volumes were extracted from the volumes of interests (VOIs) used for the quantification of each type of signal.

Tumor volumes measured based on PET-FDG uptake ranged from 53 to 271 mm3 (mean= 143, SD= 105); tumor volumes measured from fDOT after Sentidye® uptake ranged from 83 to 265 mm3 (mean= 170, SD= 86). There was no significant correlation between the volumes measured with the two modalities (as shown in Figure 3-14, with R^2=0.5548), i.e. the ratio of fDOT-based to PET-based tumor volumes varied over almost one order of magnitude (range: 0.35-3.1; mean= 1.6; SD= 1.0). More interestingly, co-registration of fDOT with PET showed that the signal of overlap between vascular accumulation of Sentidye® and tumor uptake of FDG, calculated with the signal of the overlapping region divided by total fDOT signal, was 42±14%, indicating that only part of the tumor was hypervascular while the majority of the fDOT signal appeared located in the vasculature surrounding the tumor (Figure 3-9 D-F).

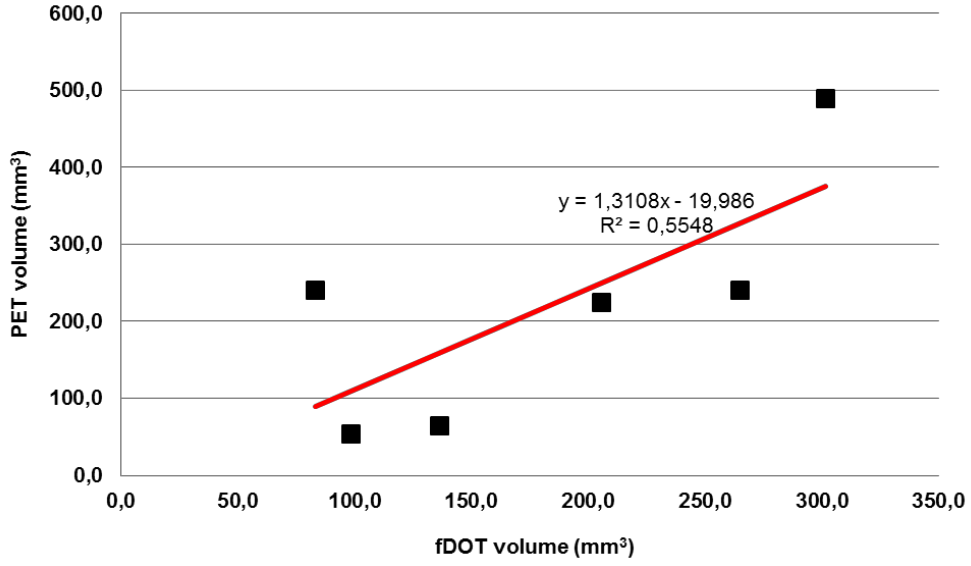


Figure 3-14 The correlation between the tumor volume (mm^3) measured from fDOT signal and from the PET signal.

3.6 Discussion

There is a clear trend towards multimodal imaging of tumor as the best way to provide relevant information on a significant number of cancer hallmarks (Culver et al., 2008; Hanahan and Weinberg, 2011). Recent studies have demonstrated the possibility to combine fDOT and PET imaging for co-registered localization of two or more biological processes at the molecular level (Garofalakis et al., 2010; Nahrendorf et al., 2010). These studies required the use of CT for the anatomical structure, therefore leading to irradiation of the animal that might have an effect on tumor cell development. This prompted us to develop direct co-registration of PET/fDOT without use of CT.

Moreover, the acquisition of 3D fDOT data is slow and would require extremely long acquisition times to scan a complete volume of the mouse body. The FM is not contiguous to the mouse body, thus requiring simultaneous 3D acquisition for unconnected objects (i.e. mouse body plus FM), which is a difficult task to implement. Finally, mice would need complete depilation since hair is incompatible with the proper transmission of fluorescent signals.

Interestingly, the planar image and the surface scan are acquired in the same referential as the fDOT volume, and thus intrinsically co-registered with it. After an initialization step to define the regions in which the FM should be detected (the RODs), the method automatically detects the coordinates of the FM and immediately co-registers the fDOT image with the PET image. Since the FM are permanently attached to the animal plate holder, the definition of the RODs needs to be performed only once for a given animal supporting plate and remains valid for all following imaging sessions with that plate.

It should be noted that the co-registration based on the FM is appropriate only in the case of rigid body transformation. The co-registration is achieved thanks to the stability of the relative positions of the FM with respect to the entire image in each modality. During the experiments, the FM remained in a fixed position with or without

contact with the subject. The co-registration does not take account for the deformation and the movement of the subject relatively with respect to the FM. Consequently, the subject should be kept unmoved during acquisition from one modality to the other. Therefore this FM based method cannot be applied to the case of follow-up studies of inter or intra subject follow-up imaging. To account for the deformation or the movement of the subject, a deformable model may be applied a posteriori to the co-registration, as a post-correction of the image quality (Krol et al., 2006). However, this deformation correction was not applied in this thesis, which has only considered the case of a rigid transformation based on FMs.

The method is based on the same principles as a manual co-registration, i.e. a detection of the points with maximum intensity, while the barycenter approaches use intensity weighting. However, Wang et al. have reported that co-registration based on barycenter intensity weighting performed better than an unweighted intensity approach (Wang et al., 1996). This apparent discrepancy is likely due to the shape of the signal of the FMs in the PET images, which is generally not well-rounded because of the noise generated by the reconstruction from punctiform sources known as the “star” artefact (Figure 3-15). This adds irrelevant weight to the RODs and renders the detection of the barycenter largely dependent on the size and localization of the ROD, leading to unpredictable and often poorly reproducible calculation of the FM’s position. In contrast, detection by maximal intensity is well adapted to automatic co-registration and can be generalized to any ROD to give reliable co-registered image results. As long as the signals from the FM remain above the surrounding background in the defined regions, the size and shape of the RODs have no influence on the results and can be larger or smaller than three times the diameter of the FM signal size.

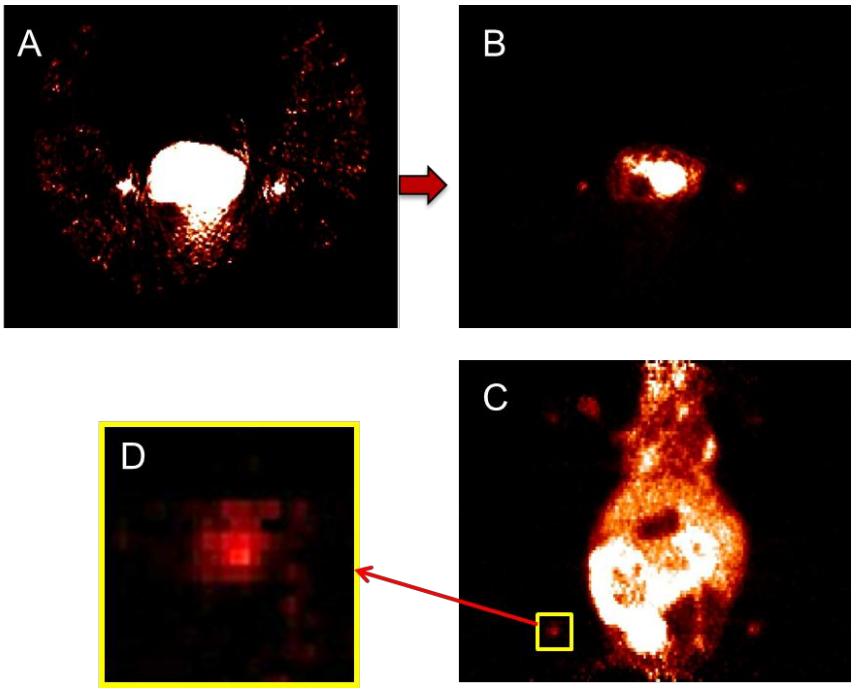


Figure 3-15: Illustration of the star artifact presents in PET image. Image (A) is the raw image of PET reconstruction of the mouse and the FM. Activity in reconstructed image is not located exclusively in original source location, but part of it is also present along each line of projection. (B) and (C) are the filtered image in axial and coronal view, where the noise is eliminated. Distinguished signal of the mouse and the FM are shown; (D) is a zoom of the FM signal in the region of ROD with emphasized signal intensity , where the noise of star artifact is still present.

Two general solutions are available to compute the point-based rigid body transformation [R, T] between the optical and PET coordinates: the iterative method (Zhang, 1994) and the closed form solution method (Horn, 1987; Eggert et al., 1997). The closed form solution method is generally superior to the iterative method in terms of efficiency and robustness (Eggert et al., 1997). Eggert et al. have compared four popular algorithms (Eggert et al., 1997): singular value decomposition (SVD), a solution involving orthonormal matrices (OM), a solution involving unit quaternions (UQ) and a solution involving dual quaternions (DQ). Each computed the translational and rotational components of the transform in closed form, as the solution to a least squares error criterion given by (Eq. 3-9). These four algorithms differ according to the representations used for the transformation components, as well as in the manner that they minimize a criterion function. Among the four methods, the singular value decomposition (SVD) developed by Arun et al. (Arun et al., 1987) was described to

give the best results in terms of 3D accuracy and stability (Eggert et al., 1997). This algorithm was therefore chosen in the present study.

The quantitative evaluation has been calculated for optical and PET image separately due to their different spatial resolution. According to Table 3-2, it is observed that the standard deviation of the co-registration error in PET image is higher than in optical image which indicates a slightly higher variation of the co-registration performance. In other words, the differences in spatial resolution between PET image and optical image could impact the accuracy of the image co-registration.

In addition, the method is adaptable to most fDOT or planar optical imaging instruments with surface reconstruction. Moreover, once the RODs have been initialized for a mouse holder with FM, multiple experiments can be co-registered automatically with the same or different mice. Where FDG is routinely used for the staging of tumors, it can be complemented with fDOT optical images of a second tumor-related activity fused to the FDG readouts.

As a proof-of-concept, images of two well-established hallmarks of cancer were co-registered: deregulation of glucose consumption through aerobic glycolysis and increased vascularisation through angiogenesis and neo-vessel formation. The mutation induces constitutive activation of the RET signalling pathway through dimerization of RET and is found in families with hereditary MTC and other disorders (Jhiang, 2000). There is evidence that RET constitutively activates angiogenesis, likely through increased VEGF secretion, in MTC (Soh et al., 1996), and RET inhibitors induce inhibition of angiogenesis (Petrangolini et al., 2006). The new blood vessels produced within tumors by chronically activated angiogenesis (‘‘angiogenic switch’’) are abnormal in their structure, distorted, enlarged, leaky, and cause erratic blood flow and hemorrhagic lakes within the tumor (Nagy et al., 2010). Sentidye® is a NIR fluorescence lipidic nanoparticle that accumulates passively in the leaky, abnormal vascular network of MEN2A MTC tumors. The observation that it distributes in a pattern distinct from that of FDG is indicative of the fact that the tumors are organized into regions with distinct underlying physiological and molecular

characteristics. Assuming that the distribution of the FDG signal indicates the localization of cancer cells and serves as a reference to the optical signal (Garofalakis et al., 2010), it can be concluded that the hypervascular part of the tumor covers approximately 40 % of the tumor area. The spatial accuracy of both PET and fDOT reconstructions has been validated with the use of CT in a previous study (Garofalakis et al., 2010). In addition, in a different set of combined PET/fDOT scans, the tumor area was sampled after sacrifice of the mice and sectioned for histology (data not shown). The ex vivo distribution of the probes matched the in vivo reconstructions perfectly. We, therefore, conclude that the mismatch in the observed contrast distribution between fDOT and PET is due to the nature of the process underlying probe distribution and not to artifacts in the co-registration method. Interestingly, high FDG uptake which reflects aerobic glycolysis is not superimposed with high vascularity in MEN2A-MTC tumors. It would be interesting to explore further the fine architecture of tumors with other molecular tracers in order to segment tumoral regions based on, e.g., oxygen pressure, pH, apoptosis, proliferation or other important hallmarks of cancer (Hanahan and Weinberg, 2011). Alternatively, it could be envisioned to co-register the distribution of a labeled drug, refine the anatomical information or superimpose maps of diffusion or viscoelastic properties using other imaging techniques such as MRI or ultrasound.

4 Multi-angle fDOT imaging with the use of mirrors

In the previous chapter, fDOT reconstruction images were fused with PET images. The uptakes of the vascular agent Sentidye® (optical) and the nuclear agent FDG for the tumor activity were simultaneously visualized and compared. This enabled to extract information of the vascular distribution around the tumor. The fused image enabled the direct comparison of fDOT reconstructions with those of PET. It was noted that fDOT imaging provides comparable image quality to PET imaging in terms of resolution (in the order of 1mm for preclinical scanners).

When comparing the system characteristics of the two modalities, the PET benefits from a gantry that records signals from every possible angle. In fDOT, in contrast, the detector (CCD camera) is fixed to the top while a planar scan is performed on the opposite side of the subject (figure 4-1). In general, the geometry of the acquisitions is expected to influence the output of a reconstruction algorithm. Given the relative position of the camera and the sources (Figure 4-1), the reconstruction algorithm is expected to favour the reconstruction resolution on the x-y plane which is normal to the camera–source z-axis. On the other hand the depth resolution along the z axis is expected to be poorer.

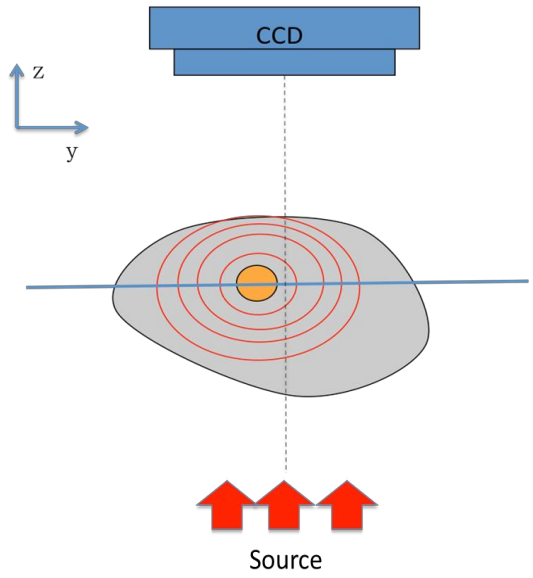


Figure 4-1: Conventional fDOT geometry; with fluorescent probes (orange spot) inside the subject (in grey color) excited by the source and the fluorescent light is captured by the CCD camera. This geometry favors the plan parallel to the fOV of camera (spot line)

The influence of the acquisition geometry on the reconstructions has already been shown in several experiments. In a study, Garofalakis et al. (2010) has co-injected a radio-labelled and optically-labelled nucleotide in a control mouse. The probe was cleared by the organism and strong accumulation of the two types of probes was reported in the region of kidney. It has allowed giving good contrast in both fDOT and PET images (Garofalakis et al., 2012). In this study the in-built software of the TOMOFLUO3D was used for the fDOT reconstructions. The accuracy of the fDOT and PET reconstructed signal was evaluated with anatomical CT scans in the kidney region. The fused kidney images of fDOT with CT and PET with CT (figure 4-2) allowed the comparison of the reconstruction resolution. The segmentation has been done following the same principle as presented in section 3.5.3, where a threshold of 30% of the maximum signal in the tumor was applied for PET images, and a threshold of 10% of maximum plus a constant value that represents the noise of fDOT reconstructions was applied for fDOT images. In figure 4-2, the red volume represents the volume occupied by the PET reconstruction, the green volume represents the fDOT reconstruction and the grey colour is the CT image of the kidneys. In the coronal

view, the PET and the fDOT give comparable results (Figure 4-2 A and B), in comparison to the CT volume, though the PET overestimates the kidney volume. However, in the axial view, the PET volume still overestimates the kidney volume (Figure 4-2 C), but more interestingly a significant compression of the fDOT signal (Figure 4-2 D) is observed along the Z direction.

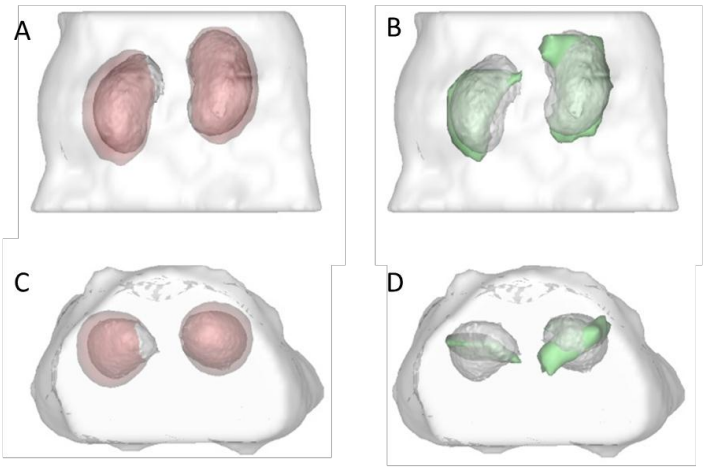


Figure 4-2: PET reconstruction of the mouse kidney (red) and fDOT reconstruction of the kidney (green) co-registered with CT volume (grey) (manual segmentation). Top row shows images in coronal view and following row shows the axial view. In the coronal view, reconstruction of both modalities overlapped with the CT image though PET overestimated the volume. In the axial view, the reconstruction of fDOT is clearly compressed comparing to the CT image and also to the PET volume.

In another experiment, the fDOT reconstruction was tested with a subject of dimensions comparable to the resolution limit of the fDOT apparatus (~1mm). A 1mm-diameter glass capillary was filled with a near infrared fluorophore and was inserted subcutaneously to the mouse scapula. A fDOT acquisition was performed at the level of the capillary and the reconstruction was performed with the in-built software of TOMOFLUO3D (Figure 4-3). Then, the accuracy of the fDOT reconstruction is evaluated from the comparison to the actual dimensions of the capillary. In this case, the reconstruction gives the accurate diameter value in the coronal view (Figure 4-3 A), but in the axial view the reconstructed signal is extended deeper than the capillary diameter (Figure 4-3B). This test experiment has been repeated several times and similar results were observed.

The above experiments show that the fDOT reconstruction is degraded with the depth, in a manner of compressing big organs such as kidneys, and while extending the dimensions of small targets. This degradation was assumed to be a consequence of the limited collection of signal due the “single angle” camera acquisition.

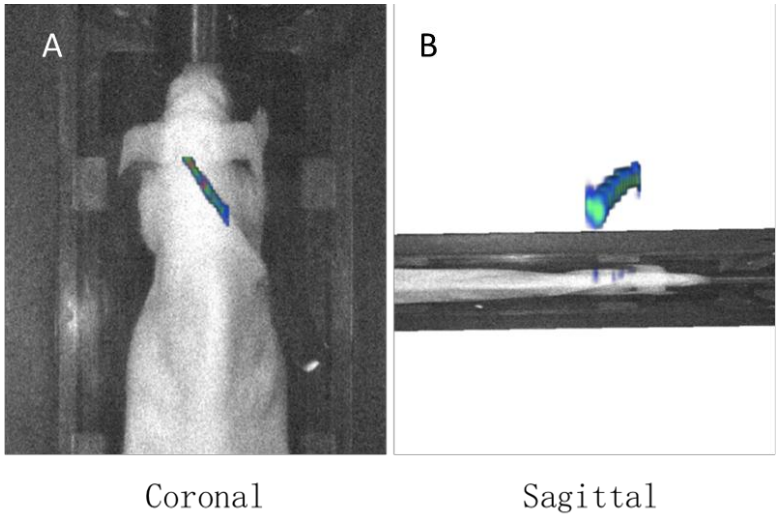


Figure 4-3: fDOT reconstruction of the capilary insert under the mouse skin. Image is overlapped with the 2D mouse photograph to indicate the position of the capilary. Left: image on the coronal view, the diameter of the reconstructed capilary remains the same as the real value. Right: image of the sagittal view, the dimension of the reconstructed capilary is longer than the real value.

In the present thesis, an approach to assess Z-axis degradation problem is proposed with the use of multi-angle acquisition geometry. Mirrors are placed at the two sides of the subject in order to redirect lateral fluorescent signals to the camera. Then a basic open source reconstruction algorithm is modified to account for these additional views in order to improve the fDOT reconstruction quality.

In the following sections a detailed presentation of this method is provided.

In section 4.1, a general introduction to multi-angle fDOT imaging is presented. In section 4.2 the principle of fDOT image reconstruction is introduced. In section 4.3 the open access fDOT reconstruction algorithm TOAST (Time resolved Optical Absorption and Scattering Tomography) is described together with a finite element method (FEM) inverse solver. In section 4.4, the materials and method of this study are presented, including the incorporation of the mirrors to the conventional fDOT

geometry and the implementation of mirror geometry to the TOAST reconstruction. In section 4.5 the results of the present study are shown and finally the discussion follows in section 4.6.

4.1 The conventional fDOT system and the multi-angle approach

4.1.1 The conventional fDOT system

As has been already mentioned in previous chapters, the fDOT is a relatively novel technology that is still under development. fDOT like any other tomographic system requires a set of “projections” in order to reconstruct a 3D image (Kak et al., 1988). The term projection refers to an image that is captured at a given angle determined from the different spatial combination of the three major imaging components: the detector, the source and the subject. Different projections can be obtained by the moving each of the above components of the system.

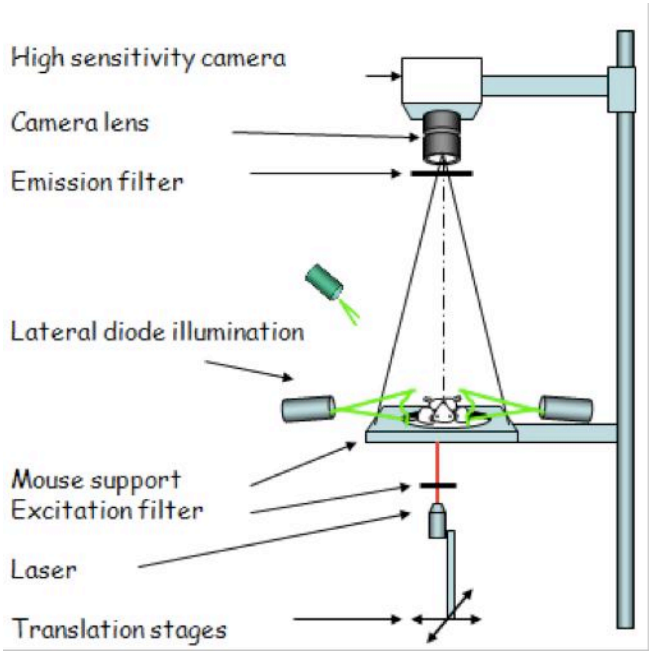


Figure 4-4: Schematical representation of the fDOT imaging system

In figure 4-4 the standard geometry of a single-angle non-contact fDOT system is presented. The subject is scanned with a laser source. The CCD camera fixed to the top records the emission light, with several emission filters selecting signals of different wavelengths. As the excitation laser scans the animal at different source positions, the image captured with each source-detector combination corresponds to a different projection. Since the orientations of the source and detector are fixed, all of these projections are generated with signal coming from the same side of the subject. Currently the majority of fDOT apparatus uses the above presented single camera apparatus or variations of this geometry (Zacharakis et al., 2005a; Garofalakis et al., 2010; Nahrendorf et al., 2010; Correia et al., 2011). Many reasons justify this choice, notably the low cost, the simple instrumentation, the user convenience and also the comfort provided to the subject.

4.1.2 Multi-angle optical imaging

Although single camera systems have been the method of choice for many experimental and commercial fDOT scanners, several multi-angle optical imaging systems have been also proposed.

The first fDOT systems represent in multi-angle systems since they were incorporating fibers that were surrounding the subject for the collection of signals (Ntziachristos et al., 2002) (Figure 4-5). A fiber-based time-resolved reconstruction method has been proposed to retrieve depth-related information on absorption variation of the tissue (Montcel and Poulet, 2006; Montcel et al., 2006).

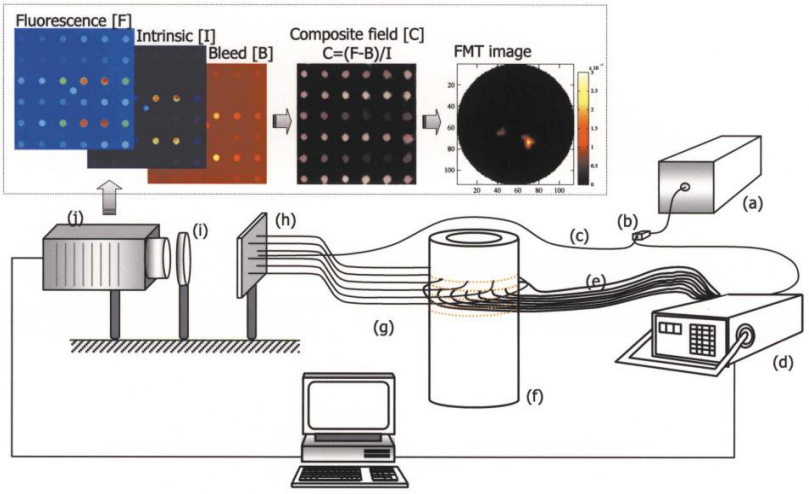


Figure 4-4-5: Schematic of the first fiber-based fDOT imager used for the experimental measurements. The imager consisted of a 675 nm laser diode (a) and a beam splitter (b) that divided light to a reference channel (c) and an optical switch (d). 24 source fibers (e) and 36 fiber bundles (g) were employed to illuminate and collect light respectively from the optical imaging bore (f). The fiber bundles and reference fiber were arranged on a grid (h) and imaged with a CCD camera (j) using appropriate filters (i). The insert surrounded by the dotted line describes the typical measurements (F, *I, B)* and formation of the composite field (C) used to produce quantified fDOT images. (Ntziachristos et al., 2002)

Later, CCD cameras were proposed as a means of signal detector (Ripoll et al., 2003). The advantage of CCD cameras is their ability to detect high sampling data (Schulz et al., 2004). CCD camera acquisition detects high resolution images, however they are less flexible components and therefore sophisticated apparatus need to be constructed in order to achieve multi-angle detection. One solution was proposed where the subject turns at multiple angles while the position of camera and source are unchanged. One such approach was proposed by Turner et al. in 2005. It consisted of a time-resolved complete angle fDOT system with a incorporated rotation stage (Figure 4-6) to collect transillumination images of both early-arriving photons and later-photons which is also capable for continuous wave photon acquisitions (Turner et al., 2005).

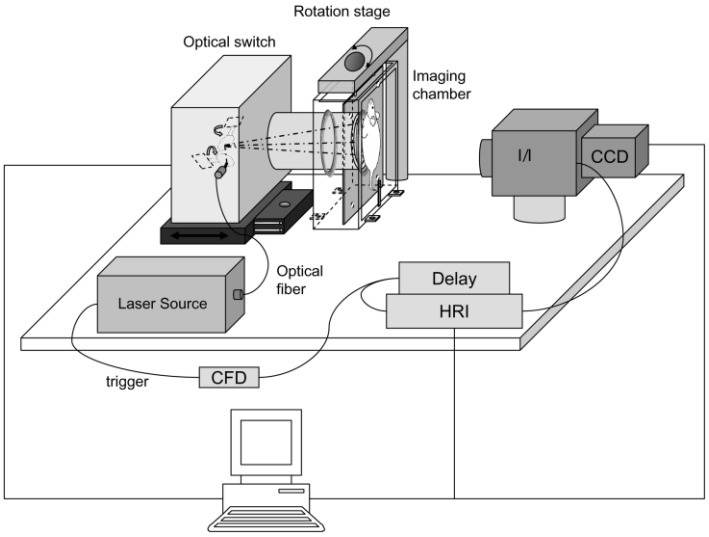


Figure 4-6: Schematic montage of the Time-resolved full-angle fDOT imaging system, using noncontact technology.

Similar system geometries have been used for fDOT in-vivo imaging of tumors (Deliolanis et al., 2006, 2009) immune function imaging (Garofalakis et al., 2007; Meyer et al., 2007). However, these systems require that the subject sample is fixed in an upright position which does not represent a physical position.

Later apparatus designs took into account the animal comfort by incorporating a geometry where the animal is lying down on a plate (Zacharakis et al., 2005a, 2005b). Still multiple angles can be recorded but given the positioning of the subject the camera and/or the laser source should move. This can be done with the use of a gantry. Da Silva et al. has proposed a method that combined the fDOT with XCT imaging (Da Silva et al., 2007). More recently, another system has been developed by Schulz et al. for the development of a FMT/CT hybrid system (Schulz et al., 2010) (Figure 4-7). However this system is technically challenging and another disadvantage is the long acquisition sequences when multiple angles are involved.

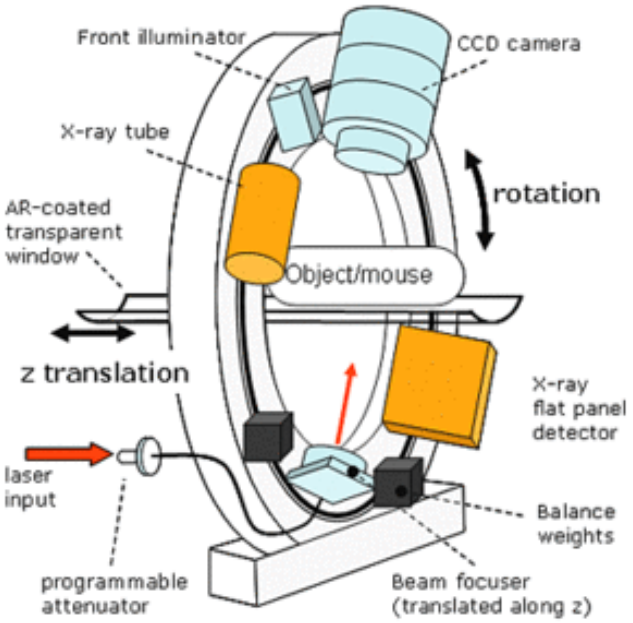


Figure 4-7: Schematical representation of the hybrid imaging system for simultaneous fluorescence tomography and X-ray computed tomography (XCT) of small animals. The system is based on a 360° rotating gantry, which accommodates the XCT hardware and a CCD camera–based optical detection modality (fDOT) (Schulz et al., 2010)

A simple way to achieve multi—angle projections is the utilization of mirrors while the subject stays lying in the holder. Such systems have been already proposed in the case of planar fluorescence, bioluminescence studies and fDOT. In bioluminescent imaging, the idea of using mirror to reflect the signal from different angles has been proposed in a commercial system (Kok et al., 2007). Instead of rotating the subject or the camera, a mirror is placed near the subject and is rotated at eight different angles to reflect the bioluminescence signal from different projections (Figure 4-8).

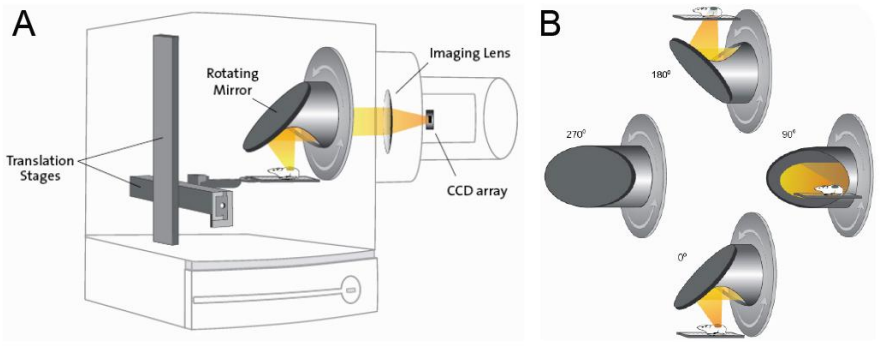


Figure 4-8: 3D bioluminescent imaging (IVIS 3D, Xenogen Capiler Life Science): A) Scheme of the system. B) Illustration of 4 possible positions of the mirror out of 8 that generate sequential images

Wang and al. (2008) proposed a fixed arrangement of mirrors with a single CCD camera that recorded four views of reflected bioluminescence images simultaneously (Wang et al., 2008) (Figure 4-8 A), which allowed the recording of higher data throughput comparing to the previous system. Similarly, Roncali et al. (2008) developed a system equipped with a conical mirror that collected all the signals on one single frame (Roncali et al., 2008) (Figure 4-8 B).

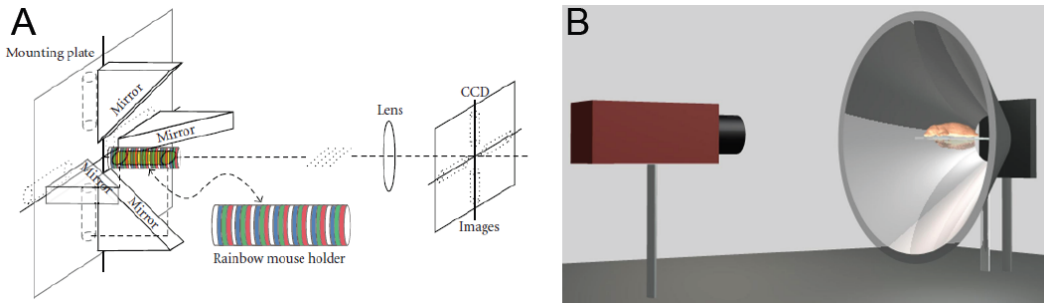


Figure 4-9: Set-up of the simultaneous multi-angle acquisition with a fixed arrangement of four mirrors proposed by Wang et al. (A) and with a conical mirror proposed by Roncali (B).

Another mirror-based system was developed by Chaudhari et al (2005) (Figure 4-10 A) and Biospace Lab (Figure 4-10 B), for simultaneous acquisition of multispectral imaging data over most of the surface of the animal (Chaudhari et al., 2005).

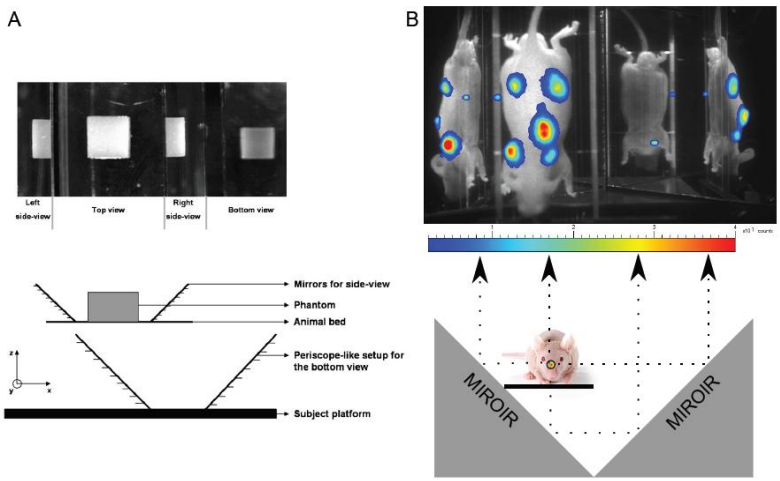


Figure 4-10: Set-up of the mirror based simultaneous multi-angle acquisition of Chaudhari et al (A) and Biospace Lab (B).

Both systems rely on an implementation of mirrors oriented at 45 ° with respect to the optical axis, offering the opportunity to observe simultaneously the main parts of the mouse in a fairly similar way as in conventional geometry (Chaudhari et al., 2005).

In the case of the fDOT, Li et al (2011) implemented the conical mirror system (Figure 4-11) for the different projections. This approach has been introduced in order to fit a fDOT system inside a PET gantry (Li et al., 2011) for combined fDOT/PET imaging. However in this study no comparison with the conventional imaging was made to characterize the reconstruction quality.

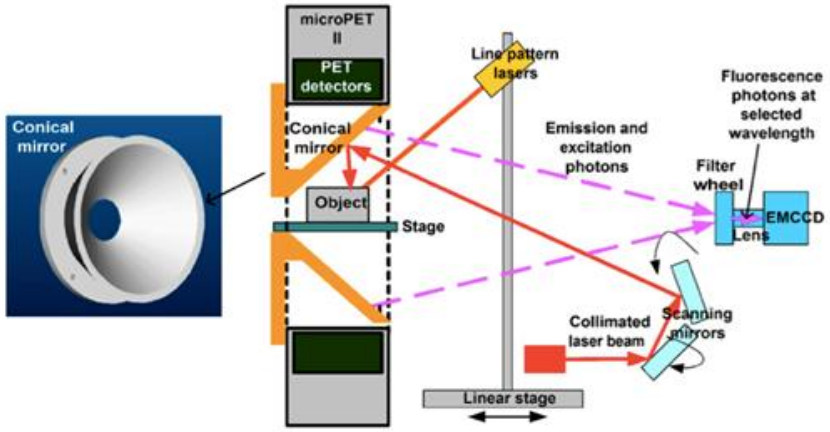


Figure 4-11: Design of conical mirror and schematic of 3D FOT system

4.2 Image reconstruction

In the following sections, the basic steps for reconstructing a fluorescent probe inside a diffusive medium will be presented. The reconstruction of a fluorescent concentration inside a diffuse medium can be divided into two steps: the forward problem and the inverse problem.

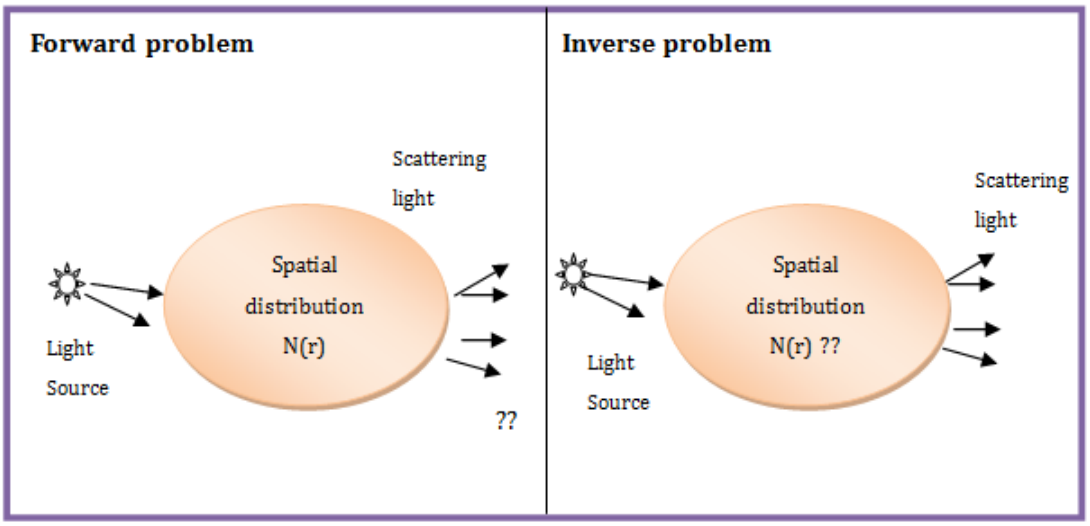


Figure 4-12: General representation of the forward problem and the inverse problem. N(r) stands for the spatial distribution of the optical property in tissue.

In optics, 3D reconstruction refers to determining the spatial distribution of an optical property based on a set of detection images and on the geometrical parameters that describe the experiment geometry (source/detector positions and subject's geometry) (Arridge, 1999; Ntziachristos and Weissleder, 2001). This process is the inverse to the process of determining the light propagation at any point inside the subject (and therefore at its surface) by taking into account its distribution of optical properties and the experimental geometry. The first process is called solving the inverse problem and the second is called solving the forward problem (Figure 4-12). From the above, it is evident that the problem of optical reconstruction is a two-step process. Solving the inverse problem first requires solving the forward problem.

4.2.1 Forward problem - Diffuse optics theory

As has been stated in the introduction, fDOT accounts for the diffusive propagation of photons in tissue in order to solve the forward problem and therefore reconstruct fluorescent signals inside opaque mediums. The problem can be assessed thanks to theoretical tools based on the diffusive theory that were developed in the mid-nineties (Yodh and Chance, 1995). Below is a brief description

of this theoretical framework.

Given the light source X_{inc} and the distribution of the fluorescent concentration $N_t(r)$ at position r within a volumetric medium V(Figure 4-13), the propagation of light X_{prop} at any position of the medium and consequently on the surface of the object S is represented by the following function:

$$f\left[X_{inc}(r,t); N_t(r)\right] \rightarrow X_{prop}(r,t) \qquad \textbf{Eq 4-1}$$

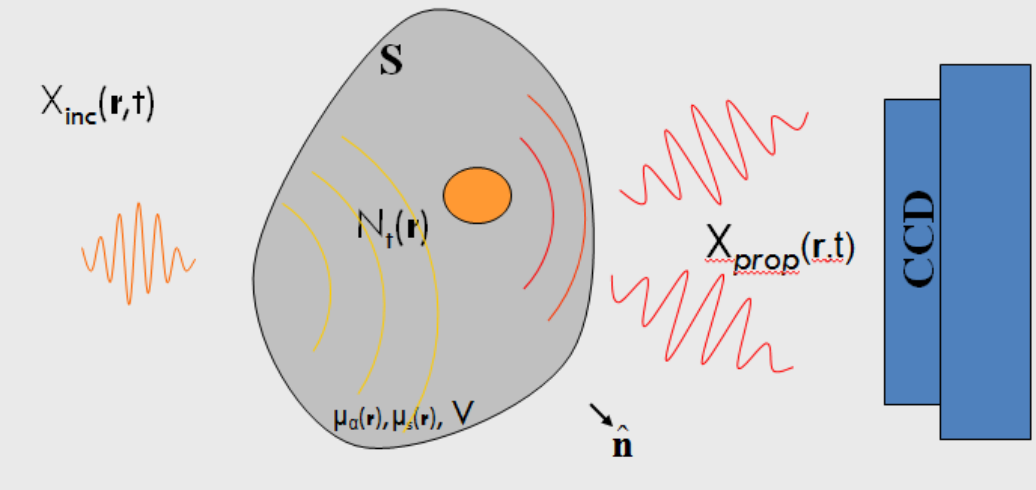


Figure 4-13: Basic scheme of the forward model based on the diffusion theory

In theory of tissue optics, a convenient way to describe light propagation is by the use of analytical methods (Arridge, 1999). These methods model the propagation of photons as a propagation of energy and use differential equations in order to extract an equation for the intensity of light (Ishimaru, 1978; Yodh and Chance, 1995).

The diffusive photon propagation for the case of a continuous wave illumination of a scattering medium can be described by the diffusion equation (Patterson et al., 1989).

$$\nabla[D\nabla\Phi(r)] + \mu_a\Phi(r) = S(r) \qquad \textbf{Eq 4-2}$$

Where $\Phi(r)$ is the average intensity of light at position r and S is the source term and D is the diffusion coefficient

$$D = \frac{1}{3(\mu_s' + \mu_a)} \quad . \qquad \textbf{Eq 4-3}$$

In equation 4-3, two important intrinsic parameters of tissue are presented, μ_a and μ'_s. μ_a represents the absorption coefficient, which is defined as the multiplicative inverse of the path that a photon travels before it is absorbed and μ'_s is the reduced scattering coefficient.

$$\mu'_s = (1-g)\mu_s \qquad \textbf{Eq 4-4}$$

with μ_s being the scattering coefficient, referring to the multiplicative inverse of the random walk path of a photon between two scattering events. Finally, g is factor taking in account the scattering anisotropy.

The diffusion equation is solved by applying a source term on the right side of Eq 4-2. In the problem of fluorescence imaging inside a tissue, two sources of diffusive light are identified. The first is produced from the laser beam as it enters the medium (excitation light). In tissue optics a light beam entering the subject is often simulated as a point source originating from a depth 1/μs below the surface (Arridge and Schweiger, 1995). The source term in Eq. 4-2 is defined as:

$$S(r) = S_0\delta(r) \qquad \textbf{Eq 4-5}$$

where δ(r) is the Dirac function and S_0 accounts for the intensity of the incident beam. The average intensity of the excitation photon $\Phi_{ex}(r)$ emitted by a continuous wave external source S at λ_{ex} at location 1/μs below $r_s \in \Omega$ is then given by

$$-\nabla D(r, \lambda_{ex})\nabla\Phi_{ex} + \mu_a(r, \lambda_{ex})\Phi_{ex}(r, \lambda_{ex}) = S_0\delta(r_s) \qquad \textbf{Eq.4-6}$$

Equation 4-6 can be solved using Green's function (Arridge, 1995; Fantini et al., 1997) for homogeneous medium:

$$[-\nabla D(r)\nabla + \mu_a(r)]G(r, r_s) = \delta(r - r_s) \qquad \textbf{Eq 4-7}$$

The solution of equation 4-6, which is the average photon density of the excitation source at position r within a volume V is then given by:

$$\Phi_{ex}(r) = \int_v dr_0 G(r_s, r) S(r_s) \quad \textbf{Eq 4-8}$$

Photons from the incident light propagate inside the medium; excite the residing fluorescent molecules giving rise to fluorescent light.

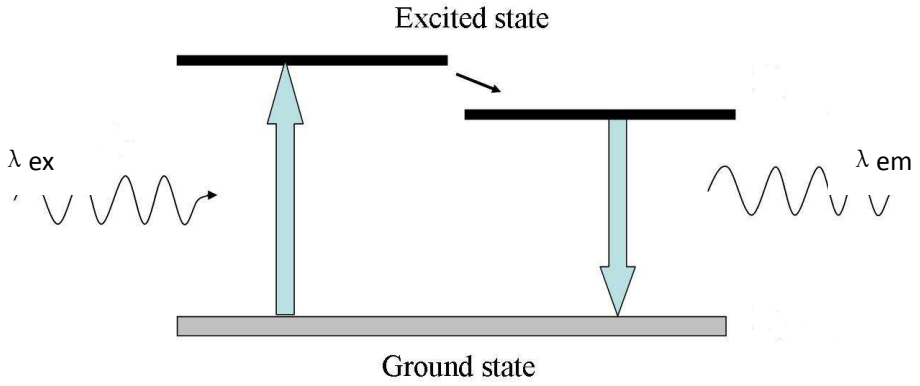


Figure 4-14: Schematic representation of the photon excitation from the ground state to the excited state by the energy of excitation wavelength λ_{ex}, followed with the photon emission of λ_{em}.

The emission of fluorescence corresponds to a second source of light (fluorescent light) with a bigger wavelength (Figure 4-14). The fluorescent source term which represents the number of emitted fluorescent photons is defined as:

$$F(r, r_s) = \eta \sigma^{fluo} N_t(r, r_s) \Phi_{ex}(r, r_s) \quad \textbf{Eq 4-9}$$

where the η is the fluorescence quantum yield and the σ^{fluo} is the absorption cross section of the fluorescent molecules at the excitation wavelength. N_t is the total number density of the fluorescence molecules.

The emission photon intensity $\Phi_{em}(r)$originating from a fluorescent inclusion is given by:

$$-\nabla D(r, \lambda_{em}) \nabla \Phi_{em}(r, \lambda_{em}) + \mu_a(r, \lambda_{em}) \Phi_{em}(r, \lambda_{em}) = F(r, r_s) \quad \textbf{Eq 4-10}$$

After solving equation 4-10, the average photon density of the fluorescence signal $\Phi_{em}(r)$ in a volume V is expressed with the aid of Green's function as (Born and

Wolf, 1999):

$$\Phi_{em}(r) = \int_v dr_s G(r_s, r) F(r_s) \Phi_{ex}(r_s) \qquad \textbf{Eq 4-11}$$

The excitation and the fluorescence signals are emitted by the medium and are recorded by a CCD camera.

4.3 Inverse problem

A means of solving equation 4-11 for the unknown $N_t(r, r_s)$ is based on a forward model using the finite-element method (FEM) (Weaver and Gere, 1980; Strang and Fix, 2008). The FEM method was first developed for solving the problem in solid mechanic, based on the matrix method for mechanical structural analysis.

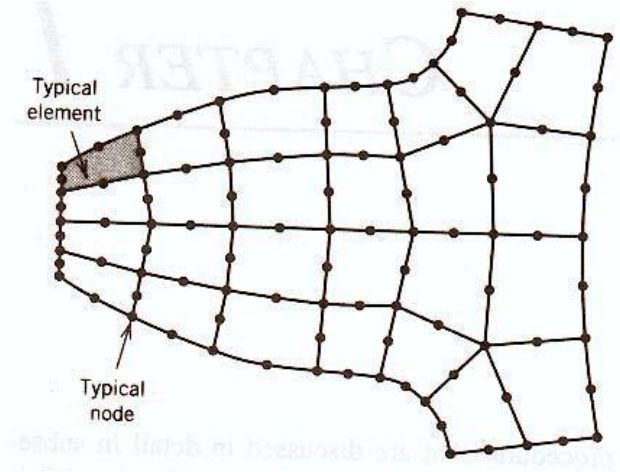


Figure 4-15: Simple illustration of the elements and nodes in FEM, the system is cut into elements and the elements are reconnected at "nodes" as the point of conjunction.

The basic idea of the FEM method is to subdivide the entire system into "elements", to form of matrix that describes a system of complex structure containing a large number of components. In FEM, the system is cut into elements and the elements are reconnected at "nodes" as if each node being the point of conjunction (Figure 4-15). Therefore the system is represented with a sum of units constituted of

nodes and elements.

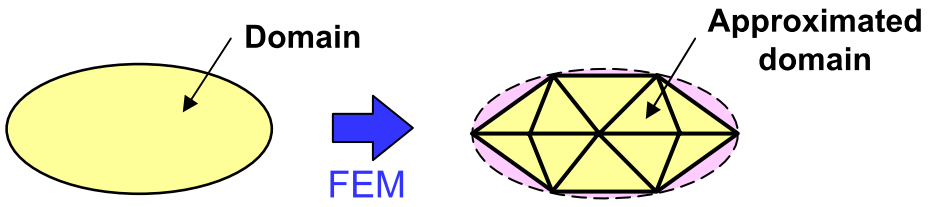


Figure 4-16: basic sheme of the FEM discretization.

In the FEM approach, the solution of equations 4-8 and 4-11 can be extracted for both homogeneous and heterogeneous media. Let us recall the basic problem of fDOT reconstruction as illustrated in Figure 4-12. The inverse problem aims at determining the spatial distribution of an optical property based on a set of detected images and the geometry of the problem. For the case of the measurements, the detector readings should be related to the theoretical equations of photon density described in the previous section. The measurements are then modelled by a Gaussian kernel centered at the detector location and computed as a linear factor $\mathcal{M}$, acting on the photon density at the boundary of the domain. Thus the measurements of the photon density of the excitation and emission terms at the detector position rd are given by:

$$\Phi_{ex}^{meas}(r_d) = \mathcal{M}\Phi_{ex}(r); \quad \Phi_{em}^{meas}(r_d) = \mathcal{M}\Phi_{em}(r) \qquad \textbf{Eq 4-12}$$

Many authors have proposed the normalization of the fluorescence data with the excitation data (Ntziachristos and Weissleder, 2001; Garofalakis et al., 2007) This approach is called the Normalized Born approximation (Ntziachristos and Weissleder, 2001) and it is expressed as:

$$U_b(r_d) = \frac{\Phi_{em}^{meas}(r_d)}{\Phi_{ex}^{meas}(r_d)} = \frac{\Phi_{em}}{\Phi_{ex}} \qquad \textbf{Eq 4-13}$$

where vector U_b accounts for all source-detector pairs of measurement. It is common to consider the fluorophore distribution as a perturbation over a homogeneously fluorescent medium (Ntziachristos and Weissleder, 2001). The

emission photon density Φ_{em} is often approximated as being linearly dependent on the fluorophore concentration F(r). Based on equation 4-11, a small variation of the fluorophore concentration δF in the medium induces a variation of the emission photon density $\delta\Phi_{em}$. In the FEM, the studied volume is discretized in small elements. In our case the volume is considered to consist of N elements, Ω_j and the fluorophore coefficient F can be represented by an N x 1- vector. Based on the above, the variation of the emission photon density is given by:

$$\delta\Phi_{em}(r_d) = \sum_j \int_{\Omega_j} dr_j G(r_d, r_j)\Phi_{ex}(r_j, r_s)\delta F_j \qquad \textbf{Eq 4-14}$$

where $\Phi_{ex}(r_j, r_s)$ is the excitation photon density at r_j due to a source at r_s.

Eq 4-14 expresses the relation between Φ(r) and F(r). Optical tomography involves multiple projections which correspond to multiple source–detector pairs, M. Let us consider as i each source-detector pair and by taking into account Eq. 4-13 and Eq 4-14, and:

$$U_b(F) = JF \qquad \textbf{Eq 4-15}$$

Where J_{ij} are the corresponding Jacobian matrix entries that relate each measurement $(U_b)_i$ to the F(r):

$$J_{ij} = \frac{\partial(U_b)_i}{\partial F_j} = \frac{1}{\Phi_{ex}^{meas}(r_d, r_s)} \int_{\Omega_j} dr_j G(r_d, r_j)\Phi_{ex}(r_j, r_s) \qquad \textbf{Eq 4-16}$$

According to Schweiger (1994), the reconstruction problem was transformed into minimizing iteratively the error norm ε of equation:

$$\varepsilon = \left\| \Phi_{em}^{meas} - U_b(F) \right\|^2 + \alpha^{\Psi}(F) \qquad \textbf{Eq 4-17)}$$

with the regularisation parameter α, and $\Psi(F) = \|F\|^2$ for quadratic Tikhonov regularisation (Schweiger, 1994).

.

4.4 Materials and Methods

4.4.1 Experimental Setup

The imaging system used in this study consisted of the 3D optical imager TomoFluo3D (Cyberstar, Grenoble, France) that has been introduced in chapter 3 (shown in Figure 3-1).

CT measurements were performed using the PET/CT scanner Inveon® (Siemens, France). A total of 360 images were recorded with an angular step of 1°. The reconstructions were performed with the in-built reconstruction software based on a filtered back-projection method. Each reconstruction resulted in a volume of 480x480x480 voxels with a voxel size of 0.206x0.206x0.206 mm^3.



Figure 4-17: Inveon® CT scanner (Siemens)

4.4.2 Tissue-like phantoms

Phantoms are often used in optical imaging studies in order to simulate tissue properties. Their optical properties can be defined during the manufacturing process. Phantoms serve to test the fDOT under controlled conditions. In the present study polyester resin phantoms were used. Resin phantoms are solid and inert and their optical properties are controlled by adding titanium oxide and ink for scattering and

absorption respectively. The recipe for the phantom used in this study can be found in (Boas, 1996). The μs' is set to 15 cm^{-1} and the μa set 0.2 cm^{-1}. These values are chosen to simulate the tissue optical properties The phantom used in the present study has been built in the Universidad Carlos III de Madrid, Departamento de Bioingenieria e Ingenieriq Aeroespacial.

4.4.3 Data processing algorithm

In the present thesis, the inverse problem was solved using a finite element approach which is the basis of the open access optical tomographic algorithm TOAST (http://web4.cs.ucl.ac.uk/research/vis/toast/) (Schweiger, 1992, 1994; Schweiger et al., 1993; Arridge and Schweiger, 1995). TOAST stands for 'Time-resolved Optical Absorption and Scattering Tomography'. It is an image processing toolbox developed by Martin Schweiger and Simon Arridge (Schweiger et al., 1993) in the Department of Computer Science at University College London (UCL). TOAST consists of a set of Matlab® (Mahworks, USA) functions and was originally designed for image reconstruction of the predecessor of fDOT, the diffusion optical tomography (DOT). It allows numerical modeling of light transport and parameter recovery and performs high-level tasks in modeling, reconstruction and visualization. TOAST can be freely downloaded software and provides open source code that allows the user to develop programs based on the particularities of each problem. TOAST relies on the FEM to model diffuse light transport in tissue.

4.4.4 Incorporation of mirrors in a conventional fDOT imager

In section 4.1.2, a multitude of fDOT imaging geometries has been presented. In each case different criteria were governing the system's design. The most essential are the following: instrumentation simplicity, maximization of information content, comfort of the subject and simplicity for the user.

In the present study, minor modifications were made to a prototype fDOT system operating in the trans-illumination mode. This system has been developed by the CEA/LETI in Grenoble, France (Koenig et al., 2010). In this system the camera records signals from the top of the subject and the laser is illuminating from the bottom. The idea of the mirrors method is to capture the signal coming from both sides of the subject, by modifying the existing apparatus. For this reason, two mirrors were placed at the two lateral sides of the subject that reflect the signal coming from the profile (Figure 4-18).

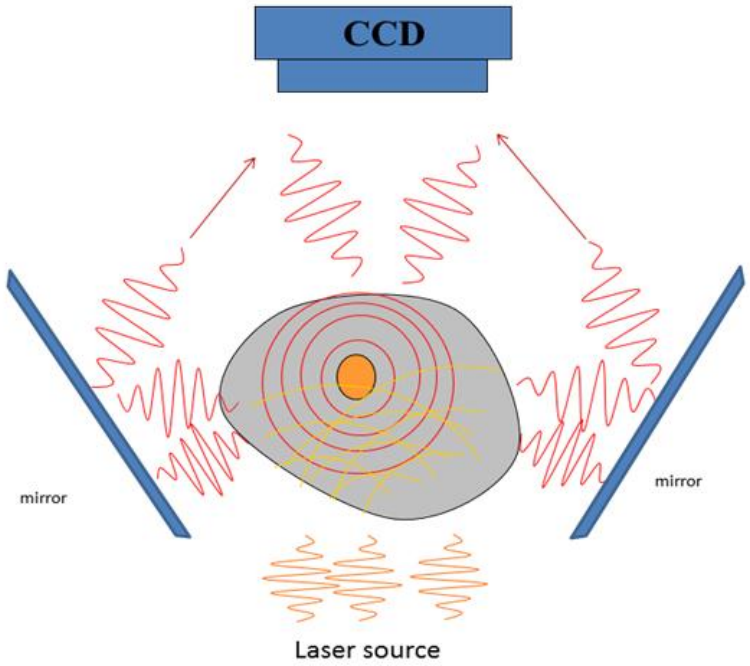


Figure 4-18: basic scheme of the mirror geometry after the modification of the conventional fDOT geometry.

The two mirrors were placed symmetrically on the two sides of the animal with an angle predefined at 45 degrees. The CCD camera on the top records the central view and two lateral views that are created by the mirror reflection. This arrangement is considered equivalent to an assembly of three cameras of identical optical characteristics that are situated at three positions (top, left and right) to record image simultaneously (Figure 4-19). The two lateral views are symmetric with respect to the central view.

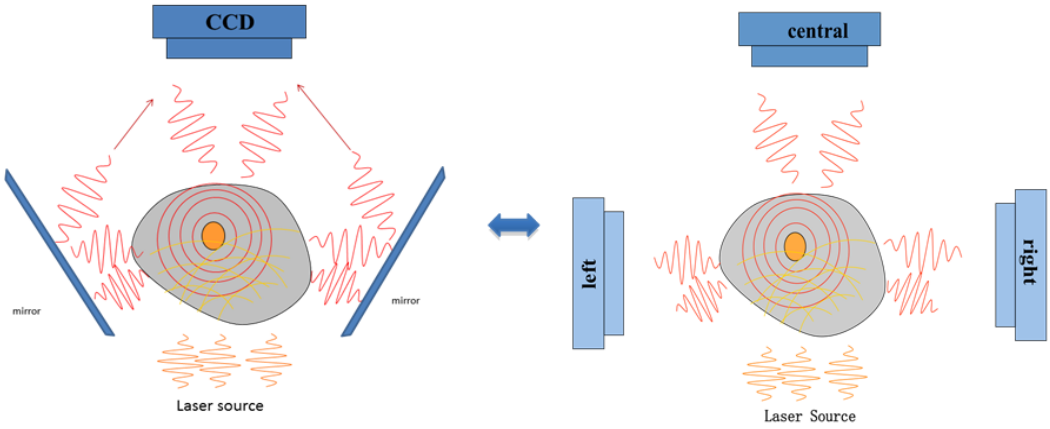


Figure 4-19: equivalent representation of the mirror geometry as virtual cameras locatied at both sides of the subject

As can be seen in (Figure 4-20), given the x and y axes for the coronal view, the mirrors enable to reflect the signal coming from the XZ plan.

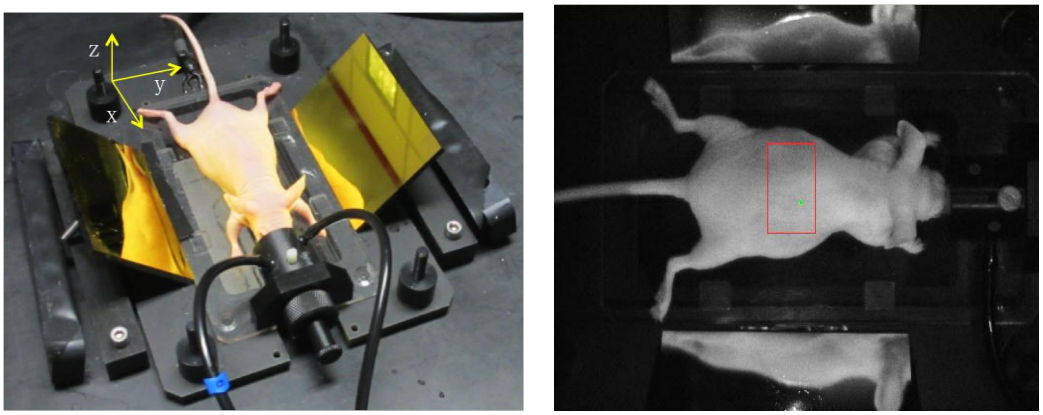


Figure 4-20: Left: the experimental set-up of our mirror geometry fDOT imaging system, Right: white light image acquired by the CCD camera during image acquisition.

This approach offers simplicity in terms of instrumentation and results in a simultaneous multi-angle acquisition. Comparing to the acquisition geometries mentioned previously (Chaudhari et al., 2005; Wang et al., 2008), the present arrangement is simplified but still appropriate for the fDOT acquisition. The excitation and fluorescence signals are recorded by changing the emission filter under the CCD camera, and both the central view and the lateral view were recorded at the same time. The next steps consist in reconstructing the fluorescence distribution inside the

animal's body using the acquired multi-view data set.

4.4.5 Implementation of the TOAST reconstruction algorithm

The image reconstruction algorithm applied was based on the TOAST software developed by Prof Simon Arridge and Dr Martin Schweiger in UCL (Schweiger et al., 1993; Schweiger, 1994; Arridge and Schweiger, 1995). TOAST is a software suite for image reconstruction in optical tomography. TOAST provides open source code in Matlab and can be adapted to the particularities of a given study. This adaptation consists of generating the input files for TOAST, modifying the source code and the parameters of the functions according to the acquisition geometry. It solves the diffusion equation with the finite element method to calculate the photon density within the medium and the photon current through the surface. The processes in TOAST reconstruction consist of a mesh generator, a FEM solver, and a data processing and analysis tool. The mesh is used to take the geometry and the boundary of the subject into account. The reconstruction generates a spatially resolved map either of the scattering, or the fluorescence absorption inside the tissue from a set of measurements, by iteratively minimizing an error function that describes the differences between the true measurement data and the data simulated by the FEM forward model using pre-defined optical parameters.

Four input files are necessary for TOAST reconstruction:

a) a mesh file (.msh) contained the coordinate of the nodes and element of the FEM mesh of the subject with the connectivity of the nodes;
b) a source/detector file (.qm) that includes the coordinates of each the source/detector pair;
c) the fluorescence image matrix M_{fluo} and
d) the excitation image matrix M_{exi} recorded at different excitation source position.

TOAST is well-developed software that has been used by many science groups. Template functions in Matlab are available that allow users to modify or create new functions based on these templates. Therefore, the users were simply asked to generate the input data corresponding to their particular study and modify the parameters of the template function according to the particular optical system.

In this thesis TOAST functions were modified in order to account for the mirror acquisitions. More specifically, this work consisted of generating the mesh file of the subject. Then the qm file defining the position of the source and detectors was calculated given the additional detector signal provided by the mirror images. Finally the matrices of the fluorescence image (M_{fluo}) and the excitation image (M_{exc}) obtained from the acquisition raw data, in a way that the side images are incorporated.

The above data were integrated as input data into the template TOAST functions. Function coefficients related to the imaging system were modified and a regularization parameter related to the error function for the reconstruction iteration was defined. Finally, all above factors were adjusted to optimize the reconstruction performance.

4.4.6 Mesh file generation.

In order to reconstruct the fluorescence image, it is necessary to take into account the shape of light propagation medium. The mesh volume of the subject was acquired during the imaging acquisition. The mesh files utilized in TOAST are used to define the node coordinates and element connectivity of the finite element mesh required by the FEM forward solver. The elements of the FEM after discretization have the form of tetrahedrons.

In this study, a CT scan of the subject has been used to extract the correct surface volume. Therefore, for each fDOT acquisition, a CT scan was performed. Thanks to the fiducial markers-based automatic image co-registration method introduced in chapter 3, the volume image acquired by the CT scan was co-registered

to the fDOT images.

The Iso2mesh software (http://iso2mesh.sourceforge.net/cgi-bin/index.cgi) (Fang and Boas, 2009) has been chosen to convert the CT image to FEM mesh. Iso2mesh" is a Matlab/Octave-based mesh generation and processing toolbox designed for the creation of surface and tetrahedral meshes from 3D volumetric images. Iso2mesh allows the conversion of 3D volume images like CT, PET etc., into the FEM discretized mesh with extraction of the nodes coordinate information. Iso2mesh toolbox enables the input from volumetric image and can create 3D tetrahedral finite element (FE) mesh from surfaces, 3D binary, segmented or grey-scale images, allowing the generation of a tetrahedral mesh with custom mesh resolution from the direct input of the grey-scale CT volume image. The CT image volume and the desired size of element are taken as input parameters, and as an output a matrix including the node coordinate list and the connectivity list of the mesh is generated. The following figure (Figure 4-21) presents an example of conversion of the CT gray-scale volume image into the FEM mesh.

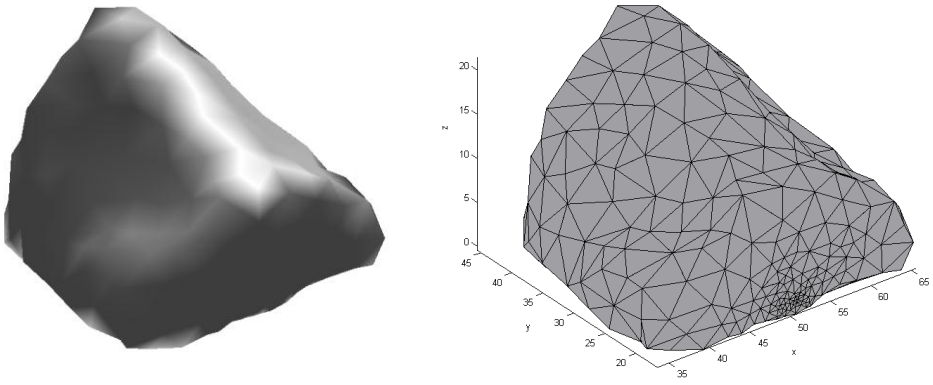


Figure 4-21: example of converting the CT gray-scale volume image in to the FEM mesh

A general problem with 3D mesh is the choice of the number of elements and nodes. The number of elements and nodes should be sufficient enough to ensure the correct resampling of the reconstruction and providing enough reconstruction resolution. However, a large amount of elements and nodes results in large matrices and consequently in longer computational times. Therefore, a compromise should be found for the number of elements and nodes by taking into consideration the desired

resolution and the computational time needed for the reconstruction. According to (Schweiger, 1994), typically the number of elements for a 3D mesh is limited to less than 10^5, and is varied according to different size of the studied subject.

The mesh is selected with respect to the zone of the optical scan, which is in turn selected with respect to the position of the targeted organ. Two limits are selected on the coronal image (X1 and X2) approximately 2mm from the top and bottom edge of the optical scan region respectively, so that the laser source defined by the red rectangle in figure 4-22 would not coincide with the edge of the segmented mesh. Since the typical value of μs' for tissue in NIR is 15 cm^{-1}, this distance of 2mm which is about three times of transfer mean free path has been chosen to ensure the diffusion equation stands for the fDOT reconstruction of the three views. This zone is relocated onto the CT volume image using the transformation matrix calculated with the co-registration method presented in chapter 3.

In our study which concerned the imaging of the kidneys, a segment of the entire CT volume (region covered by blue rectangle in figure 4-22) around the region of interest ROI (red rectangle) is selected and used for the mesh generation. The segment is defined by firstly pre-selecting a region based on the X1 and X2 limits. From the entire CT volume a region in the level of the kidneys is selected.

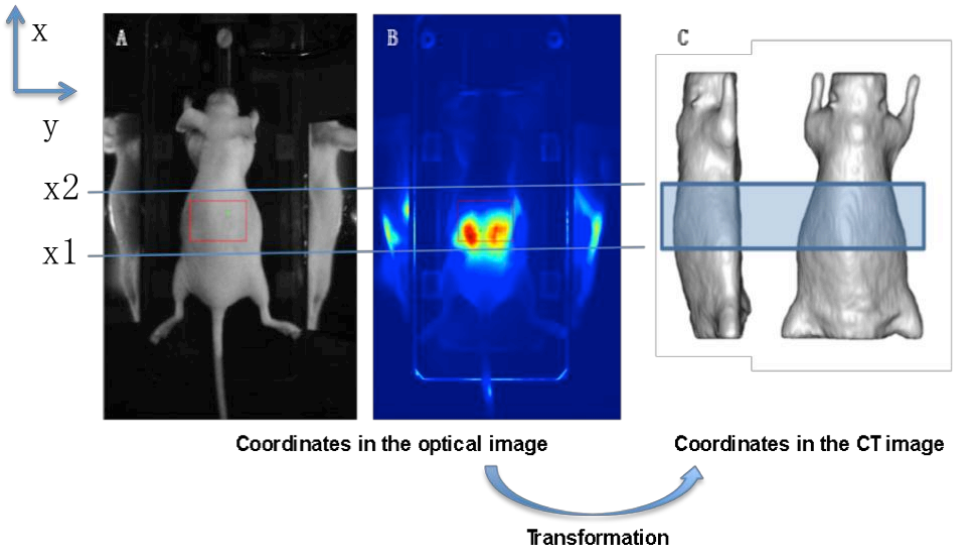


Figure 4-22: identical selection of the region of interest in data image (fluorescence and excitation image) and the CT volume segmented for mesh, via image transformation between the optical image and the CT image

The selected segment of the CT image is then used as the input gray-scale image in Iso2mesh. The size of nodes and elements is defined so that the mesh contains about 2400 nodes. Then Iso2mesh function returns as the output the matrix containing nodes information, which is used to generate the proper mesh file with extension .msh as one of the input for the TOAST reconstruction.

4.4.7 The Source/detector file (QM file)

The other input of the TOAST reconstruction program is the source/detector file, which is also called the QM file. In the FEM model, the physical source is approximated as an isotropic point source on the surface. Three principle elements are contained in the QM file: the coordinate of the source positions, the coordinate of the detector position and the link list between the sources and detectors (Annex).

During image acquisition, the laser source scans the animal at different position one point after another in the ROI that is predefined at the beginning of the experiment. The TOMOFLUO3D scanner generates a header file containing the laser positions at the end of each acquisition. The source coordinates defined in the QM file were extracted from this header file by copying the laser positions contained in the header file in the order of the laser movement during acquisition. The coordinates of detectors presented in the qm file are defined by the position of the camera, by which the image has been recorded at a certain laser position. The source and the detector positions are given in the same coordinate system in the QM file. One source position related to one detector position, and this correspondence between the source and the detector was indicated in the QM file.

In this study of multi-angle fDOT imaging, the detector CCD camera captures the images of the central and lateral view simultaneously in a fixed position. This configuration is equivalent to images captured by three cameras: one real CCD camera on the top, and two virtual cameras on the right and left. Therefore one source position corresponds to 3 detectors position: central, left mirror and right mirror. The

source position defined in the QM file is given by the position of the laser scan within the predefined ROI; the detector position in the QM file is defined by the position of the CCD camera (position A in figure 4-23) and of the viral camera (position A' in figure 4-23).

In practise the use of mirrors represents a system of three cameras: one is real and two others are virtual cameras. The choice of the mirror angle determines the position of the virtual camera. In the present thesis the virtual cameras are chosen to be at 90 degrees with respect to the laser direction. This requirement is fulfilled by choosing an appropriate angle of the mirrors. Figure 4-23 shows how this angle is calculated with respect to any desired camera position and consequently to the chosen 90 degrees geometry.

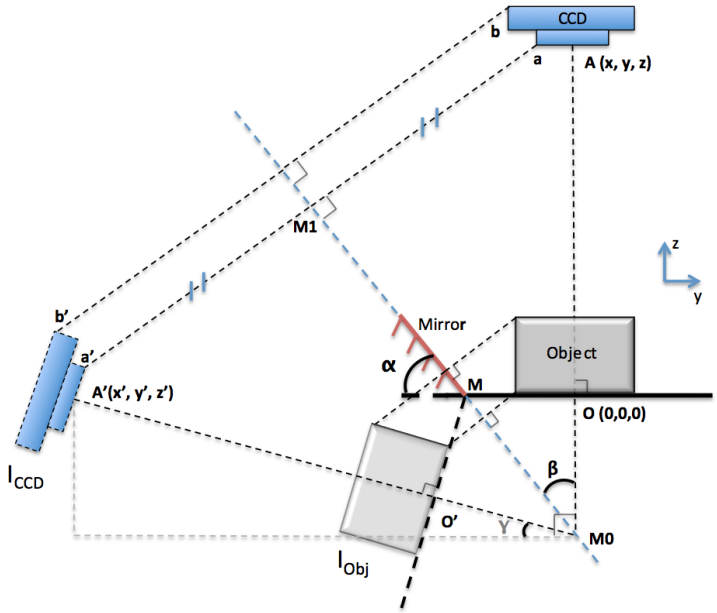


Figure 4-23: scheme of the calculation of the position of the equivalent virtual camera according to the position of the mirror (presented in one side of the mirror, identical for the other side) .

As shown in the figure above, the position of the subject is at O (x_0=0, y_0=0, z_0=0). The CCD camera is at position A (x, y, z). The mirror is on the supporting plate with its fixed edge at point M and its other edge forms an angle α with the plate. The I_{Obj} is

the mirror image of the object, I_{CCD} is the mirror image of the CCD camera. The mirror image of the object captured by the CCD camera is equivalent to the actual image of the object as it is captured by the virtual camera. The coordinates of position A' of the virtual camera position are expressed (x', y', z'). These coordinates depend on the angle α. The relation between the coordinates (x', y', z') and the angle α has been calculated as follow.

The distance AO between the subject and the CCD camera (40 cm), as well as the distance MO between the subject and the lower point of the mirror (5cm) and the angle of the mirror α can be measured from the imaging system, and represent the known parameters. The subject and the image of the subject I_{obj} are symmetric and the CCD camera and the I_{CCD} are also symmetric with respect to the axis of the mirror M0M1, then:

$$\begin{cases} \beta = 90^{\circ} - \alpha \\ \gamma = \alpha - \beta \end{cases} \quad \textbf{Eq 4-18}$$

$$OM_0 = OM * \tan\alpha \quad \textbf{Eq 4-19}$$

$$\mathrm{A'M_0} = \mathrm{AM_0} = \mathrm{OM_0} + \mathrm{AO} \quad \textbf{Eq 4-20}$$

the coordinate of A' :

$$\begin{cases} \mathrm{x'} = \mathrm{x} \\ \mathrm{y'} = -\mathrm{A'M_0} * \cos\gamma \\ \mathrm{z'} = \mathrm{OM_0} - \mathrm{A'M_0} * \sin\gamma \end{cases}, \quad \textbf{Eq 4-21}$$

The position of the virtual camera is chosen to be at the level of the subject, the angle of the mirror should be fixed to $\alpha = 49°$.

4.4.8 Data file - Fluorescence matrix (M_{fluo}) and Excitation matrix (M_{exc})

The data file contains boundary forward data for a set of source and detector sites at the surface of the imaged subject. In our case, the data file consists of the fluorescence and excitation image acquired during the imaging experiments. Matlab was used for the data processing. Since in Matlab images are represented as matrices, the fluorescent and excitation data were transformed in matrices, M_{fluo} and M_{exc}.

Figure 4-24 shows a typical fluorescence image acquired by the imaging system. From each camera image three regions were selected corresponding to the views captured by the central, the left and the right detector. Only signal from the rectangular region around the scanning frame is selected from the raw image to form the data matrices. The central view (grey rectangle 2 in the center) is defined based on scanning frame, with an extension of approximately 2 millimetres so that the position of the laser source would not be located on the edge of the segmented mesh to ensure the validity of the diffusion equation. Keeping the same interval in x-axis and extending in the y-axis, the left “mirror” (grey rectangle 1) and right “mirror” (grey rectangle 3) frames were chosen with respect to the targeted organ.

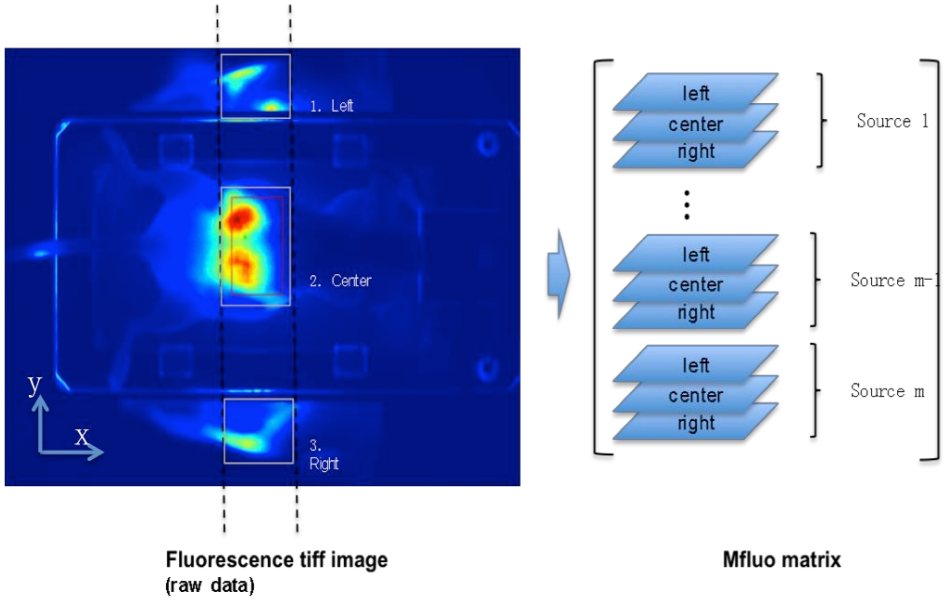


Figure 4-24: Generation of fluorescence image matrix Mfluo with the fluorescence tiff image (raw data)

Each laser source point gives two images by using an excitation and an emission filter in front of the camera. From each camera image three sub-images are created corresponding to the three detector views. The data are organized as 3D matrices (image stacks) following the pattern presented in figure 4-24.

The fluorescent and excitation images are projected to the mesh according to the source/detector position defined in the QM file: Based on the position of the camera

and its distance to the subject, the algorithm projected the data onto the surface of the subject, taking into account the free space propagation (Ripoll et al., 2003) of the diffusing light from the surface to the detector. In order to simplify the overlapping between the mesh and optical image for the evaluation of the fDOT reconstruction, the resolution of the fluorescence and excitation tiff image (raw data) as well as the CT volume image have been resampled to 1mm in the x, y and z axes direction.

4.4.9 Modification and execution of the TOAST algorithm with the generated input data

In loading all the files, the program associates the forward model with the input image data, calculates the Jacobian and executes the reconstruction iteration with a defined regularization parameter. The program returns as the output the 3D reconstruction matrix that can be visualized in different slices.

Two parameters are influencing the most the reconstruction result: a) the mask based on the excitation image

$$Dmask > \% * \max(\Phi_{ex}), \qquad \textbf{Eq.4-22}$$

which is used for the Normalized Born approximation (see section 4.3). The masked excitation image is used to calibrate the fluorescence image, i.e. $\frac{\Phi^{\mathrm{em}}}{\Phi^{\mathrm{ex}}}$ (see equation 4-13).

More analytically, the elements in the excitation matrix $M_{exc}=\left[\Phi_{xyz}^{ex}\right]$ is filtered with D_{mask}, where indices x y and z are the positions in the excitation matrix corresponding to the coordinates of the excitation image. Only the Φ_{xyz}^{ex} values superior to the D_{mask} were selected.. Taking the multiplicative inverse of the $\Phi_{ij}^{ex}(Dmask)$ the excitation matrix is converted to M'_{exc} (Eq.4-23), which is then multiplied with the fluorescent data for normalization.

$$M_{exc} = \left[\Phi^{ex}_{xyz}\right] \xrightarrow{Dmask} \begin{bmatrix} 0 & 0 & 0 \\ 0 & \Phi^{ex}_{xyz}(Dmask) & 0 \\ 0 & 0 & 0 \end{bmatrix}$$

$$\Rightarrow M'_{exc} = \begin{bmatrix} 0 & 0 & 0 \\ 0 & \frac{1}{\Phi^{ex}_{xyz}(Dmask)} & 0 \\ 0 & 0 & 0 \end{bmatrix} \qquad \textbf{Eq. 4-23}$$

The excitation mask D_{mask} is an important parameter in TOAST algorithm since it calibrates the fluorescence image data to account for the heterogeneity of the medium. The choice of D_{mask} is based on the noise of the recorded images. A general rule is that the higher the noise the higher the value of $D_{mask.}$ This allows filtering the images based on their noise background signal.

Another important parameter of the reconstruction is the regularization parameter (RP) involved in the inverse model and that defines the degree of iteration. This parameter corresponds to the error function implicated to the iterative process of the reconstruction algorithm. It affects the performance of the reconstruction. Different methods have been proposed to define the value of the RP (Correia et al., 2009; Chamorro-Servent et al., 2011). In our study, since the TOAST toolbox provides template function with some predefined coefficients, RP here is initialized to a value of certain order of magnitude, e.g. 0.001, then the result of reconstruction is optimized in changing slightly the value of RP within this order of magnitude. This initialization value of RP was suggested by the TOAST developer in UCL, and is generally set within the range of 0.1 to 0.0001, depending on the signal to noise ratio of the input data and the size of the data matrices.

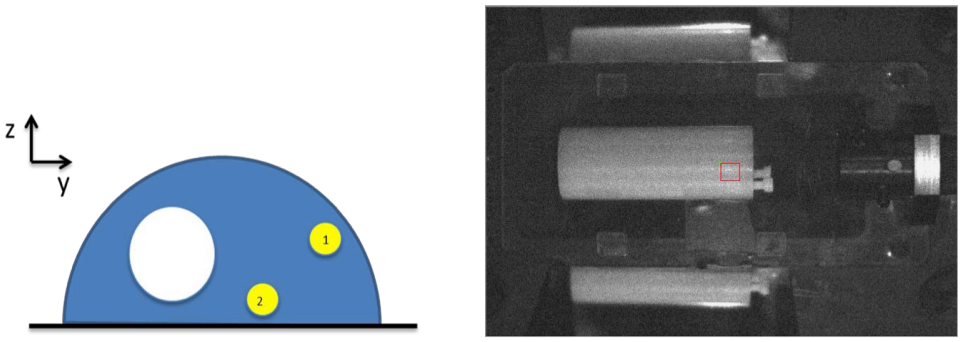
The image processing time of this program depends on the number of elements in the mesh and also depends on the size of the M_{fluo} and M_{exc}. Typical computational times varied between five and ten minutes in a Window 32-bits system Inter® Core™ i7 CPU (DELL Precision M6500) for an organ of the size single mouse kidney.

4.5 Results

So far a general introduction of the TOAST reconstruction algorithm is introduced. In the following sections, the term “mirror geometry” will be used to represent our multi-angle fDOT system with one camera and two mirrors, and “conventional geometry” stands for the conventional fDOT imaging system of a single view geometry .The experiment set-up and results of the reconstruction using TOAST with our mirror geometry will be presented in two different cases: a phantom experiment and an in-vivo mouse experiment with the reconstruction of the mouse kidney (healthy mouse). The comparison of reconstruction of the mirror geometry with the conventional geometry will be addressed, to evaluate the improvement in term of the depth resolution brought by the mirror geometry. Points such as the choice of the reconstruction parameters, influence of the mesh resolution to the reconstruction will be discussed at the end.

4.5.1 Semi-cylindrical phantom experiment

In this experiment, measurements were performed on phantom that has a semi-cylindrical form. This geometry has been chosen since it simulates the form of the mouse geometry. The design of the phantom is shown in figure 4—25 A. The optical property of the phantom is: μ_s’=15 cm^{-1} and the μ_a = 0.2 cm^{-1}. These values are chosen to simulate the tissue optical properties. The phantom contains two cavities with a diameter of 2mm and a length of 10mm where the fluorophore Hypoxisense680®(PerkinElmer™) has been inserted. This fluorescent probe exhibits an excitation peak at 680 nm and emits at 730 nm. The objective of this experiment is to reconstruct the form of the fluorophores inside the phantom.



(A) (B)

Figure 4-25: (A) schematically representation of the phantom with the position of the two cavities shown as yellow spots. (B)White light image recorded during image acquisition; the red square is the region ROI of the excitation laser source.

The phantom was fixed in the center of the supporting plate. Figure 4-25 B shows the white light image captured by the CCD camera, with the central view of the phantom and the two mirror reflections. The laser scan was performed in the area shown by the red frame.

A scan was performed in the level of the phantom cavities. The scanning grid consisted of 5x5 sources/detector pairs in steps of 2 mm and the detection area, shown as a white frame, was 10 x 10 mm^2. The mouse underwent a 10-minute fDOT acquisition followed by a 10-minute CT scan. A mask was applied to threshold the signal of the acquired images. The mask was defined as $\mathrm{Dmask} > 1\%*\max(\Phi_{\mathrm{ex}})$ with intensity greater 1% of the maximum value in the excitation image. The regularization parameter (RP) was set to $\alpha = 0.001$

The result of reconstruction of mirror geometry was compared with the reconstruction of the conventional geometry using the same mask and RP value. The comparison of the reconstruction will be evaluated using two criteria: 1) the position of the capillary reconstructed in Z direction compared to the real position; 2) the signal distribution of the reconstructed capillary.

The reconstructions of the fluorescent signal for both geometries are shown in figure 4-26. Figures A and B are the 2D representation in the axial view while figures D and E are the 3D volume of the fluorescence signal segmented and co-registered with CT volume. For the segmentation, a threshold of 30% of the maximum signal in the

tumor was applied for PET images, and a threshold of 10% of maximum plus a constant value that represents the noise of fDOT reconstructions was applied for fDOT image. As shown in figure 4-26, both geometries could reconstruct two distinct regions corresponding to the two cavities (position 1 and position 2). In the case of the mirror geometry the two cavities have similar sizes however differences are reported with respect to the intensity of the reconstructed signal. In the case of the conventional geometry the reconstruction of position 1 is spread in a larger space when compared with position 2.

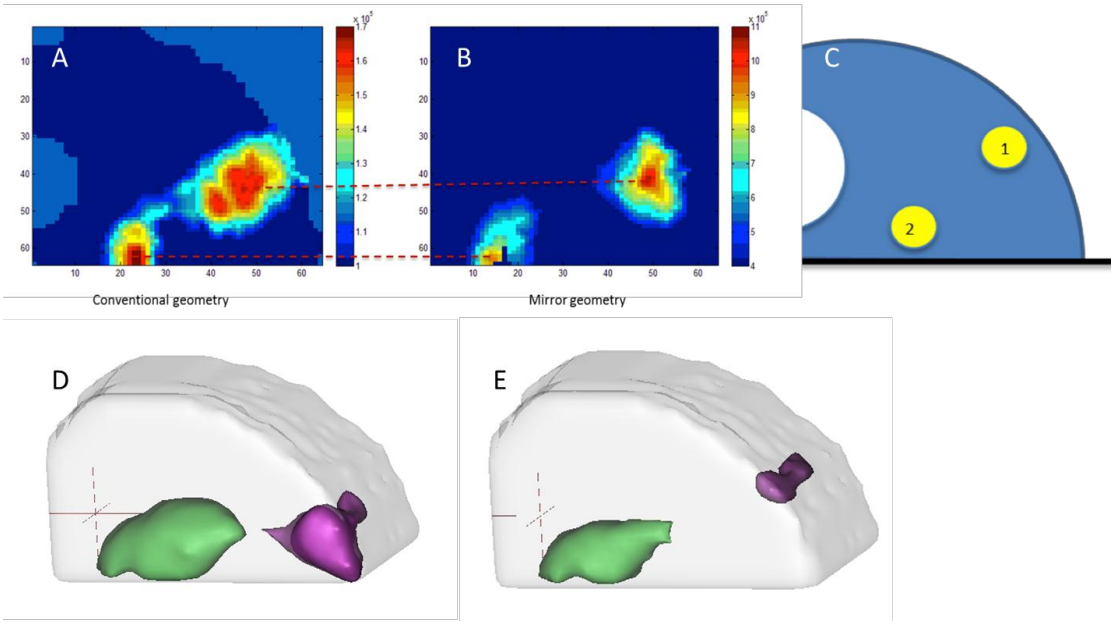


Figure 4-26 The fluorescence reconstruction of the conventional geometry shown in 2D image (A) and 3D volume (D), compared with the reconstruction of the mirror geometry presented in 2D (B) and 3D (E), The image of the phantom (C) indicates the positions 1 and 2 of the two capillary inside the phantom. The 2D images of the reconstructions are axial views. For the 3D representation, the reconstructed fluorescent signal are shown in purple and green corresponding to the capillary at positions 1 and 2 respectively, the CT mesh volume is presented in grey color.

The centers of the fluorescent signals have been reconstructed at the same Z position in both geometries. The reconstruction with the mirror geometry provides better resolution in Z direction and also in y direction; in term of distinguishing between two separate reconstructed regions compared to results obtained with the conventional geometry.

Besides the visual comparison, the quantitative comparison of the reconstruction for both geometries has been performed from the segmented volumes (Figure 4-26, D and E). The result of this quantitative analysis will be presented in section 4-6.

4.5.2 In-vivo experiments

Experiments were also carried out using mouse models. An in-vivo experiment has been conducted to test the performance of the mirror geometry with respect to the conventional geometry. The in vivo experiment consisted of reconstructing signal from the kidney of a control mouse. In the case of the in-vivo experiment, co-registered CT images of the subject were used as a reference in order to evaluate the quality of the reconstructions.

The kidney was chosen as a targeted organ since it is located deep inside the subject and can be in principle visualized with the use of CT. The fluorescent probe used was the B subunit of the Shiga toxin (STxB) coupled with the fluorophore AlexaFluor680 (Viel et al., 2008). A 25 gr female mouse received an Intravenous injection of 150 μL of a probe of a concentration of 1.6 mg/mL. The STxB targets the kidneys due to its small size and it gives strong image contrast in the region of kidney (Figure 4-27).

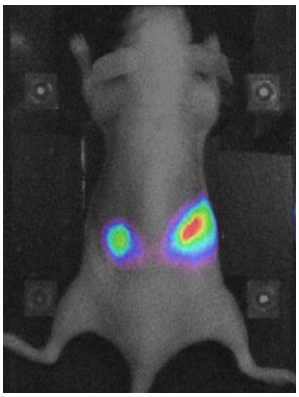


Figure 4-27 Fluorescent signal of the kidney given by Shinga toxin coupled with AlexaFluor680 overlapped with mouse photograph

A scan was performed at the level of the left (upper) kidney. The scanning grid

consisted of 5 x 5 sources/detector pairs in steps of 2 mm and the detection area was 16 x 16 mm^2. The mouse underwent a 10-minute fDOT acquisition followed by a 10-minute CT scan. The CT scan provided the geometry of the mouse surface and among other anatomical structures the shape of the kidney inside the mouse (Figure 4-28)

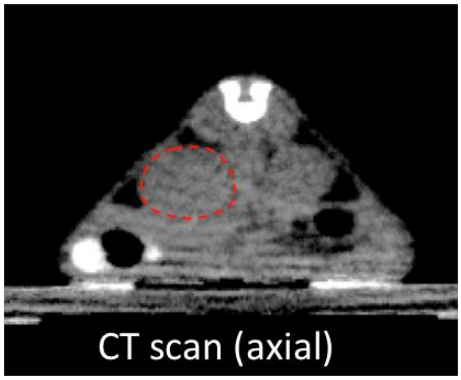


Figure 4-28 the CT scan in the region of mouse kidney, the approximate shape of the left kidney is contoured with red spot line

In figure 4-29, the red frame corresponds to the source scan and the white frames correspond to the regions selected for the image matrices M_{fluo} and M_{exc} of reconstruction algorithm. A sub-volume of the CT image (blue rectangle in figure B) that covered the left kidney was segmented to serve as the mesh volume.

The signal from the kidneys was quite strong and thus the signal to noise ratio was high, resulting in a relatively small threshold (20%) to eliminate the noise signals. Different regularization parameters (RP) have been tested and the best reconstruction was achieved by setting the RP to 0.001.

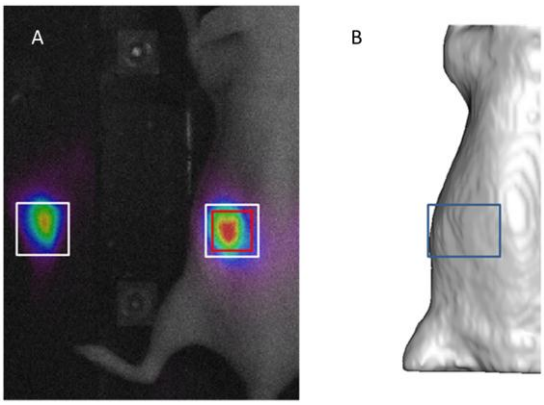


Figure 4-29: selection of the region of interest for left kidney. A is the white light image

of the mouse overlapped with the fluorescent signal of the kidney. The red frame correspond to the laser source scanning region; The white rectangles are the regions of the fluorescence or excitation signal coming from the mouse body or reflected by the mirror, which are selected for the image matrix of TOAST reconstruction. B is the CT volume with blue rectangle representing the subvolume extracted for the mesh file of TOAST reconstruction

The CT reconstruction of the kidney was taken as the gold standard for the evaluation of the fDOT reconstructions.

Figure 4-30 shows the fDOT reconstructions fused to the CT image of the kidneys. The reconstruction of mirror geometry was compared with that of the conventional geometry, with respect to the region of kidney given by CT image.

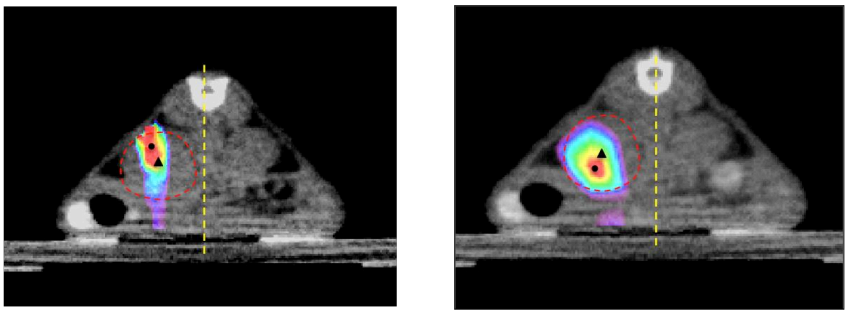


Figure 4-30: comparison of the reconstruction of the kidney in conventional geometry and the mirror geometry. Images are fused with CT image and showed in axial section, with fDOT reconstruction in rainbow color and the CT image in grey-scale image

As shown in figure 4-30, for both reconstructions the higher signal is found inside the kidney volume. In the case of the conventional geometry the signal forms a narrow pattern that is extended from the bottom of the mouse until the top of the body. Also the strongest signal was located near the surface of the mouse. For the mirror geometry, a better visualization of the shape of the kidney was achieved. However, the signal is distributed with its higher intensity in the center less noise was presented outside the contour of the kidney.

From this experiment, it is observed that the mirror geometry offered better reconstruction than that of the conventional geometry in terms of the shape of

reconstructed organs. The percentage of the overlapping region in the mirror geometry is much higher than the conventional geometry. The quantitative evaluation of the volume overlap will be presented in the following section.

4.6 Quantitative evaluation of the reconstruction

As mentioned previously, quantitative evaluation of the reconstruction has been performed for the semi-cylindrical phantom experiment presented in 4.5.1 and the in-vivo experiment presented in 4.5.2.

4.6.1 Quantitative evaluation of the phantom experiment

For the semi-cylindrical phantom experiment, the segmented volume (Figure 4-26 D, E) and intensity of the fluorescence signal at two positions have been quantified for both geometries. Table 4-1 presents the measured fluorescent signal intensity and volume of the reconstructed cylinders.

To clarify the significance of this table, separate analysis are presented below (Figure 4-31 and Figure 4-32) in comparing the reconstruction of two geometries in terms of the volume of the reconstructed cylinders and fluorescent signal intensity in the cylinders.

		position 1		position 2	
		Mirror	Conventional	Mirror	Conventional
Signal intensity (a.u)	min	86	86	86	86
	max	255	255	215	243
	mean	119.011	111.37	118.744	131.767
	STD	34.4942	25.9416	27.6359	37.2949
Volume (nb of voxel)		88	284	422	861

Table 4-1: The values of different parameters measured from the reconstructed images: the fluorescent signal intensity (in arbitrary unit) and the volume of the

reconstruction (in number of voxel counted from the volume), calculated with the reconstruction at position 1 and position 2, for mirror geometry (Mirror) and conventional geometry (Conventional) respectively.

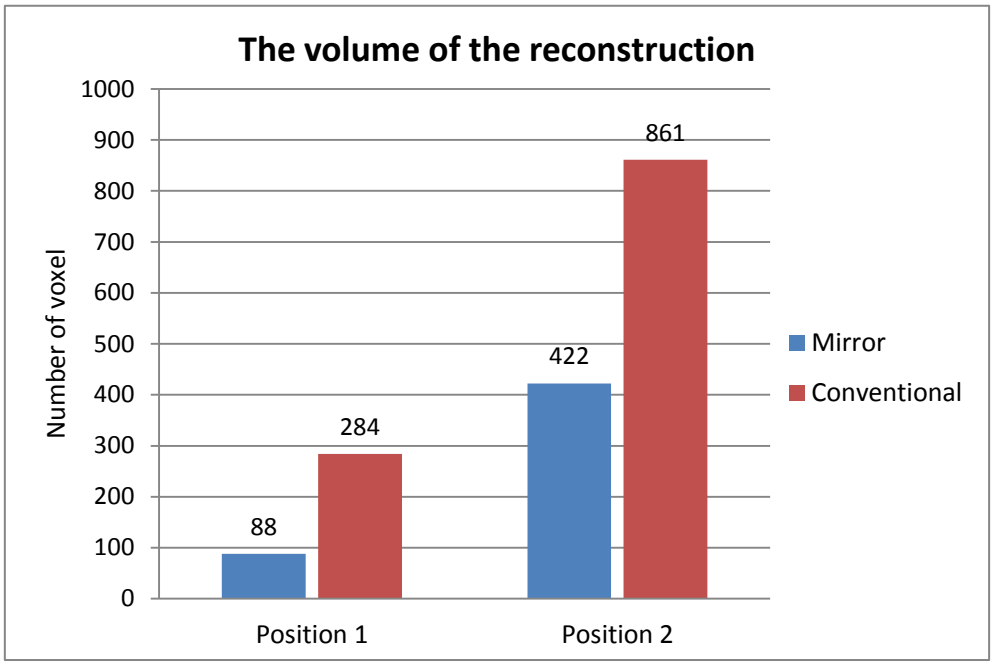


Figure 4-31: Comparison of the volume of the reconstructed cylinders between the mirror geometry and conventional geometry for the capillary at position 1 and position 2. The volumes are expressed as the number of voxel, within the region of the segmented volumes.

In figure 4-31, the volumes of the reconstructed cylinders are compared between the mirror geometry (in blue color) and conventional geometry (in red color) at position 1 and position 2 respectively. The values of the volume are presented as the number of voxel counted within the segmented volumes. Obvious differences between the blue and red bars are observed for both position 1 and position 2, and the values of the voxel number shown in the figure indicate that the volume of the reconstruction of the mirror geometry is three times smaller than that of the conventional geometry at position 1 and two times smaller at position 2. These differences well support the results of visual comparison presented in section 4.7.1, which proves that the mirror geometry offers a better resolution in term of separating two distinguished reconstruction regions, although quantitative accuracy could still be improved.

However, the real sizes of the two capillaries are the same while the volumes of

the reconstruction at the two positions are different for both geometries. This could be in fact due to the different location of these two capillaries; the position 1 is much closer to the surface of the phantom than the position 2, more scattering has taken place during fluorescent light transmission for the deeper location. The reconstruction used in this thesis is based on the diffusion theory and the absorption during light propagation is considered to be negligible. Then, it is expected that the larger volume in deep location comes along with a lower concentration, and the intensity of the reconstruction of the two locations remain identical. As a consequence, it is necessary to compare quantitatively the fluorescence intensity of the reconstruction between these two positions and between the two geometries.

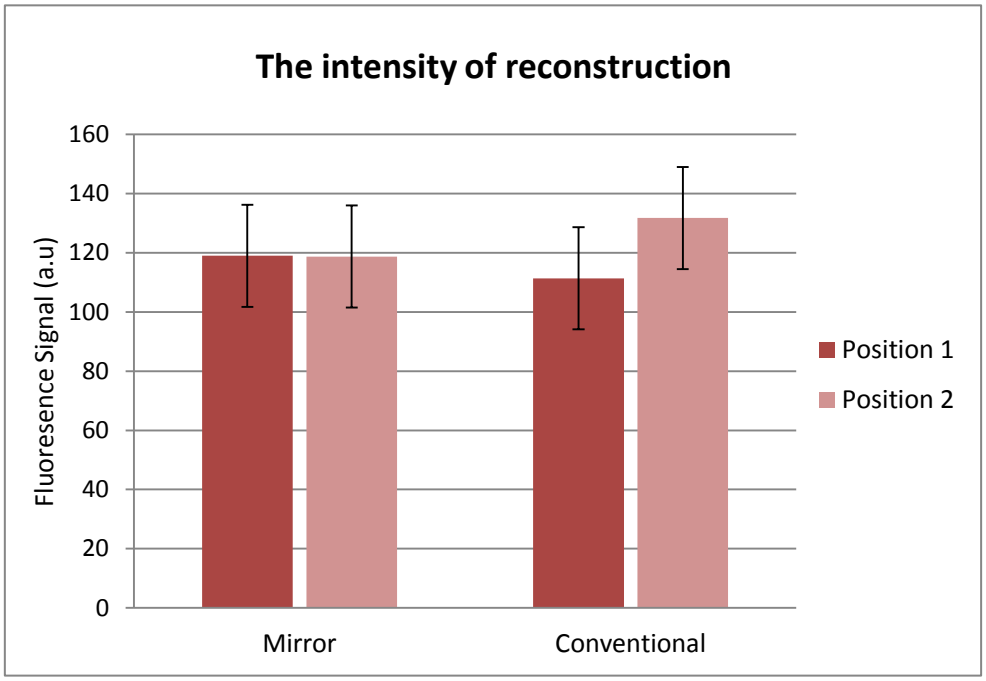


Figure 4-32: Comparison of intensity of the fluorescence reconstruction at position 1 and position 2, for the mirror geometry and conventional geometry respectively. The signal intensity of the fluorescence is expressed in arbitrary unit (a.u).

The quantification of the fluorescent signal has been performed with the values expressed in arbitrary unit. This has brought to a quantitative comparison and evaluation of the fluorescent intensity between the reconstructions at different positions for both geometries. For both geometries, the intensity values of the

reconstructions between the two positions are compared since the real intensity of the fluorescent probes present in the capillaries at position 1 and 2 are identical. Therefore, an accurate reconstruction normally should not bring much difference to the reconstruction in term of the signal intensity between the two positions. Figure 4-32 shows that the intensity of the reconstruction at two positions are almost the same for mirror geometry, while a difference of 20 a.u. between the two positions is shown for the conventional geometry. This means that the mirror geometry has been able to reconstruct the fluorescent signal with the same intensity for the both capillaries. This result proves that the reconstruction of the mirror geometry is more accurate than the reconstruction of the conventional geometry.

4.6.2 Quantitative evaluation of the in vivo experiment

To evaluate quantitatively the percentage of overlapping region for the in-vivo experiment presented in section 4.5.2, the volume of fDOT reconstruction of both geometries and the CT volume of the kidney have been segmented. A threshold of 30% of the maximum signal in the tumor was applied for PET images, and a threshold of 10% of maximum plus a constant value that represents the noise of fDOT reconstructions was applied for fDOT images. The total segmented volumes and the regions where the fDOT reconstruction of both geometries overlapped with the CT image of the kidney are shown in figure 4-33 and table 4-2.

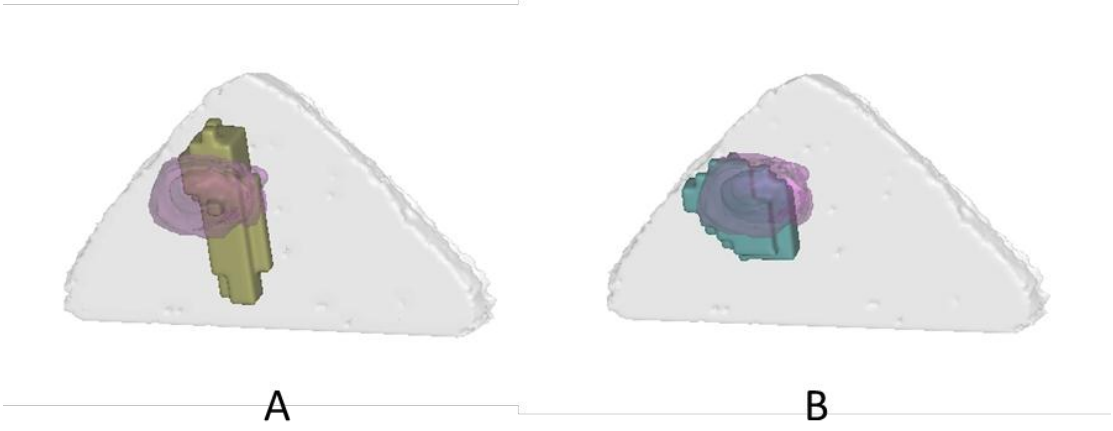


Figure 4-33: Segmentation of the fDOT reconstruction overlapped with CT image for the conventional geometry (A) and the mirror geometry (B): both the CT and fDOT

image are segmented manually. The grey triangle volumes in A and B represent the segment of the mouse body in axial plan; the volumes in magenta color show the CT image of kidney. The fDOT reconstruction of conventional geometry is the yellow volume in A; the fDOT reconstruction of the mirror geometry is shown with the light blue color in B.

	Volume (mm^3)	Volume overlapping with volume kidney (mm^3)	% of overlap (overlapped volume/ CT volume)
CT volume of the kidney	220		
Mirror geometry	116	73	33,18%
Conventional geometry	112	50	22,73%

Table 4-2: The volume of the fDOT reconstruction in the mirror geometry and the conventional geometry, compared with CT volume of the kidney.

As shown in Figure 4-33, the shape of segmented volume of the mirror geometry (shown in B) is more comparable, than that of the conventional geometry, to the segmented kidney volume of the CT image. The quantification of the segmented volumes for fDOT reconstruction and CT image is given in Table 4-2. The overlapping region between the fDOT reconstruction and the CT image of the kidney is 73mm3 for mirror geometry and 50 mm3 for the conventional geometry. The percentage of the overlapping region shown in the fourth column was calculated by dividing the volume of the overlapping region (values in the second column) with the CT volume of the kidney (220 mm3) respectively for each of the two geometries. This table indicates that the reconstruction of the mirror geometry provided a larger overlapping region than the conventional geometry. The percentage of overlapping for the mirror geometry (33.18%) is 1.5 times higher than the conventional geometry (22.73%). Since the CT image of the kidney has been considered as the standard reference for the reconstruction evaluation, a higher percentage of overlapping means closer location of the reconstruction to the real position of the kidney. Therefore the mirror

geometry has offered a more accurate reconstruction than the conventional geometry. However; further improvement and quantitative calibration of the reconstruction are needed to quantify the method and to achieve a better accuracy of the fDOT reconstruction with mirror geometry.

5 Discussion

One of the limitations of the fDOT technique is the resolution accuracy which is of the order of ~1 mm. Although this limit, imposed by physical restrictions, cannot be drastically minimized, several methods are aiming to improving the fDOT resolution. As has been presented in the introduction, multi-angle fDOT geometries have not yet been fully explored because of several technical challenges. Here a system incorporating two mirrors is built and tested in a phantom and in an in-vivo experiment.

5.1 Reconstruction parameter

Despite the fact that the improvement was found in the phantom and the in-vivo case, the performance of the reconstruction with this mirror geometry was sensitive to different parameters. One of the main parameters that affected the reconstruction performance is the excitation mask Dmask, which is used to filter and select the excitation data which in turn were used for the normalization of the fluorescence data (as described in equations 4-22 and 4-23). This parameter depends on the signal quality of the raw image: when the fluorescent raw images provide good image quality (strong signal to noise ratio), a small threshold of filtering is defined; in the contrary, when the raw images is much noisier, this threshold in % is increased to eliminate

more noise. During the test of the reconstruction quality, multiple values of the masks were chosen before achieving a good reconstruction. This demonstrates the sensitivity of the code to this parameter.

Another important parameter of the reconstruction is the regularization parameter RP. In our study, as mentioned in the previous chapter, the RP value is defined by optimizing the initial RP of the TOAST template function, and this initial RP value suggested by the TOAST developer can be varied within a certain interval. The change of RP value impacts the reconstruction result.

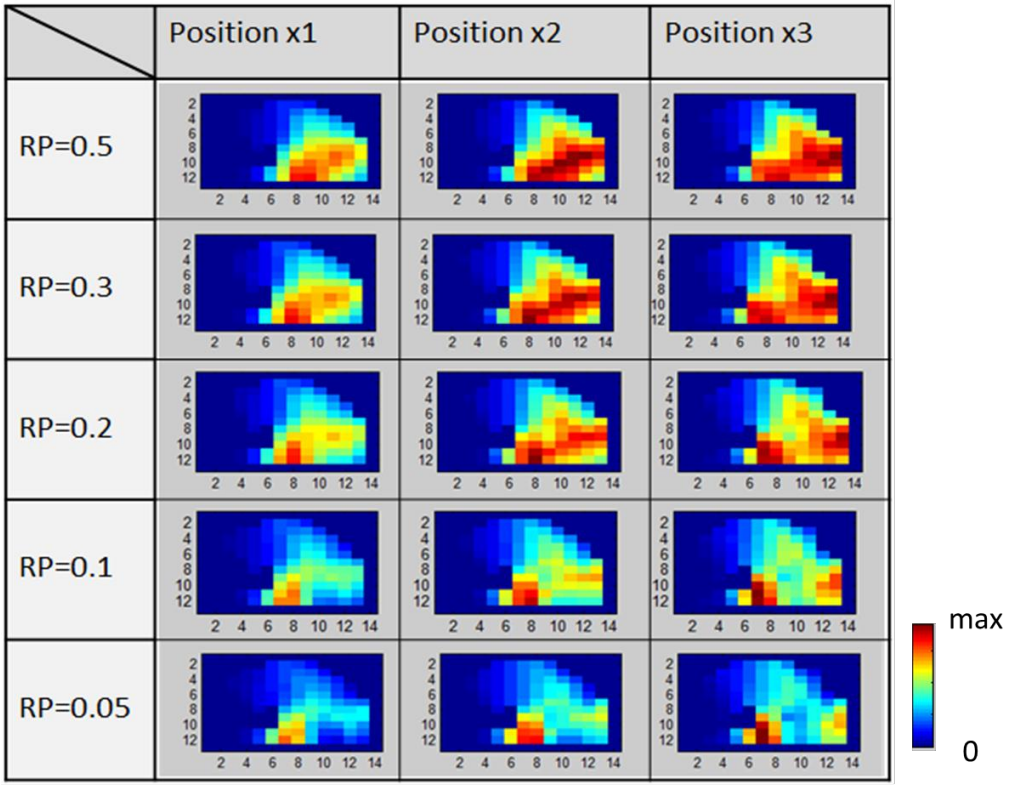


Figure 5-1: Variation of the reconstruction signal with different values of regularization parameter at three different x positions. The images of the reconstruction are shown in axial view and the fluorescent signal is present in yellow and red color depending on the intensity.

In general, the smaller the RP value, the finer and more accurate the reconstruction. This is because theoretically (Eq.4-17) smaller RP value yields a smaller error function ε defined for the inverse problem thus closer match between the theoretical projections to the true measurement. This influence of the variation of RP

to the fDOT reconstruction has been verified using the data of the semi-cylinder phantom experiment (Figure 5-1) by changing the RP value in the reconstruction algorithm. As shown in figure 5-1, when the RP value increased, the reconstructions begun to lose its resolution since the reconstruction signal of two capillary merged into one region. The signal to noise ratio decreased as the RP value increased.

Ideally, FDOT reconstruction should be robust and not depend on the fine tuning of several parameters. Therefore future improvements include the automatization of the reconstruction process by defining rules governing the selection of the parameters based on values related to the signal intensity or the subject geometry.

Besides, the fDOT reconstruction algorithm used in chapter 3 and the examples of depth deformation presented at the beginning of chapter 4 (Figure 4-2 and figure 4-3) were achieved using the reconstruction software developed by CEA/LETI, which is integrated in the fDOT imaging system TOMOFLUO3D (Hervé et al., 2007; Koenig et al., 2010). Since all the z resolution problems were observed with this algorithm, it would be preferable to choose it in the reconstruction with mirror geometry for a fair investigation of the impact of the acquisition geometry on the fDOT reconstruction. Because a different method, the “Algebraic Reconstruction Method (ART), was used to solve the inverse problem in TOMOFLUO3D software, which involves different parameters in the calculation compared to TOAST. However the TOMOFLUO3D code is not yet open access although its principles are presented in various publications (Hervé et al., 2007; Koenig et al., 2010). In this thesis it was chosen to modify an open access fDOT algorithm (TOAST) instead of rewrite the TOMOFLUO3D in-built algorithm. It would be interesting to reconstruct the data acquired with the mirror method with the CEA/LETI code and compare the performance. In each code, the multi-angle geometry is expected to give better results in comparison to the one angle geometry.

5.2 Comparison of TOAST reconstruction with TOMOFLUO3D reconstruction

The fDOT reconstruction using TOMOFLUO3D code has been applied for the conventional geometry and not to the mirror geometry. However, a fair investigation of the impact of the geometry would require that the reconstruction of TOAST and the reconstruction of TOMOFLUO3D be both performed for the phantom experiment and in-vivo experiment, under the conventional geometry.

5.2.1 The reconstruction comparison of phantom experiments

The data of the phantom experiment acquired under conventional geometry was used to reconstruct images with TOMOFLUO3D reconstruction code. The TOMOFLUO3D reconstruction was then compared with the TOAST reconstruction of conventional geometry which has been presented in section 4.5.1.

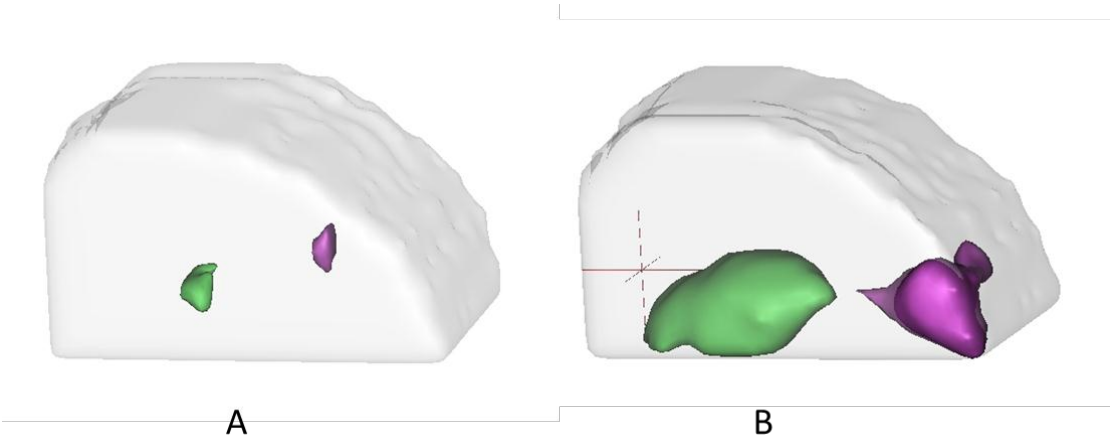


Figure 5-2: 3D image of the fDOT reconstruction using TOMOFLUO3D (A) and TOAST (B), fused with the CT mesh volume. The reconstructed fluorescent signal is shown in purple and green corresponding to the capillaries at position 1 and 2 respectively; the CT volume is presented in grey color.

From figure 5-2, the regions in green and purple shown in the reconstructed image using the TOMOFLUO3D code are smaller than those obtained with TOAST reconstruction, and are much closer to the real dimension and the positions of the

capillaries. It shows that the volume of the TOMOFLUO3D reconstruction is far better than the TOAST reconstruction. However, when the two reconstructions were evaluated quantitatively by comparing the intensity of the reconstructed signal at two capillary positions (Table 5-1), it was observed that the mean intensity value at the two positions are closer for the TOAST reconstruction than for the TOMOFLUO3D reconstruction. The deviation of the mean intensity between the two positions (the deviation here is defined as the difference of the mean intensity between the position 1 and the position 2, divided by the mean intensity of the position 1) is 37.4% for TOMOFLUO3D reconstruction and 18.3% for TOAST reconstruction. This indicates that TOAST provides a more accurate reconstruction than TOMOFLUO3D code in term of reconstructed fluorescent intensity, since the real concentration of the fluorescent probes presented in the two capillaries were the same.

	TOMOFLUO3D		TOAST	
	Position 1	Position 2	Position 1	Position 2
Min	0.115424	0.106115	86	86
Max	0.51602	0.347641	255	243
Mean	**0.279255**	**0.174847**	**111,37**	**131,767**
STD	0.100826	0.0654689	25,9416	37,2949
Volume	21.3335	21.778	284	861

Table 5-1: Comparison of the fluorescent signal intensity at the two capillaries' positions for the TOMOFLUO3D reconstruction and the TOAST reconstruction. The values are presented in arbitrary unit (A.U).

5.2.2 The reconstruction comparison of in-vivo experiments

In the case of in-vivo experiment, the data acquired under conventional geometry in the experiment presented in section 4.5.2 was used to reconstruct fluorescent images of kidney with TOMOFLUO3D reconstruction code. The result of this

reconstruction was then compared with the TOAST reconstruction of conventional geometry which has been presented in section 4.5.2. Again, the CT image of the kidney was taken as the reference image to evaluate the reconstruction performance of these two algorithms.

The images of both reconstruction algorithms were fused with the CT image (as shown in figure 5-3). The fluorescent signal of the TOMOFLUO3D reconstruction was found to be smaller than that of the TOAST reconstruction in the region of kidney. Moreover, distinct artefact signal was presented outside the region of mouse body in the TOMOFLUO3D reconstruction (figure 5-3 A), which is not the case for the TOAST reconstruction (figure 5-3 B),

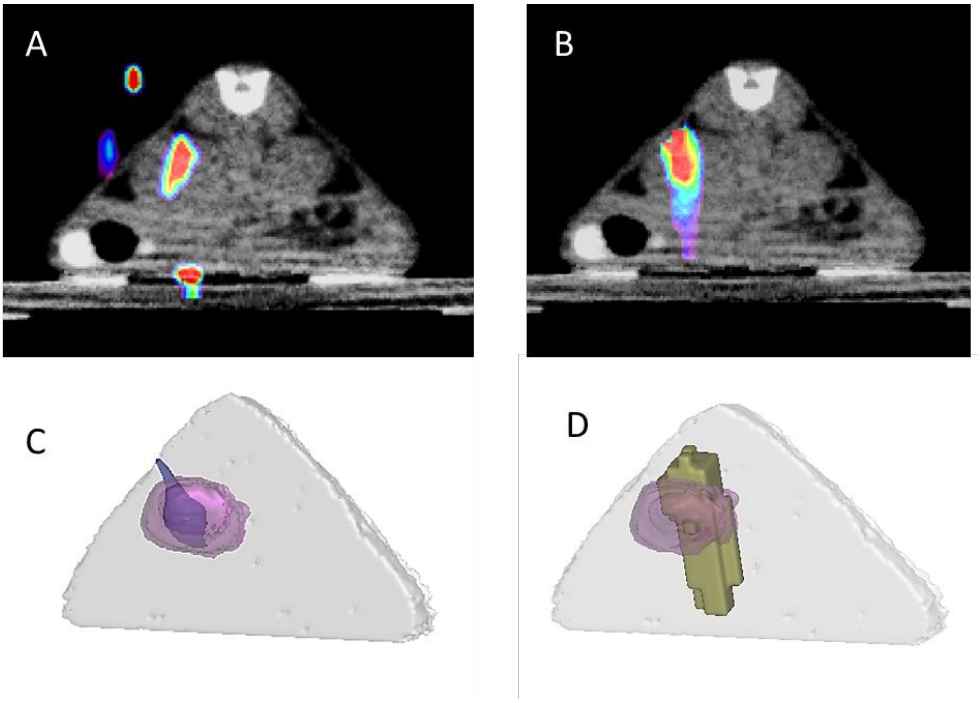


Figure 5-3: Comparison of the kidney image reconstructions using TOMOFLUO3D code and TOAST. The fluorescent images are fused with the CT images and showed in axial section. The 2D slices of the TOMOFLUO3D reconstructions (A) and of the TOAST reconstructions (B), with fDOT reconstruction in rainbow color and the CT image in grey-scale image. The manual segmentation of the reconstructed volume for TOMOFLUO3D code (C) and TOAST (D): The volumes in magenta color show the CT image of kidney. The TOMOFLUO3D reconstruction is in purple color and the TOAST reconstruction is presented in yellow.

The volumes of the reconstructions are segmented for both reconstruction

algorithms (Figures 5-3 C and D), and the total reconstructed volumes and the regions where the fDOT signal overlapped with the CT image were counted and compared (Table 5-2). As shown in Table 5-2, the total volume of the reconstruction for TOAST is bigger and closer to the CT volume. The percentage of the overlapping region in TOAST reconstruction is higher than the TOMOFLUO3D reconstruction. These values illustrated that TOAST in conventional geometry provides a better fDOT reconstruction than the TOMOFLUO3D code in reducing the reconstruction artefact outside the mouse body and also in term of the reconstructed volume overlapping with the kidney region.

	Volume (mm^3)	Overlapping volume (mm^3)	% overlap (overlapping volume/ CT volume)
CT	220		
TOMOFLUO3D	43	35	**15,91%**
TOAST	112	50	**22,73%**

Table 5-2: The volume of the fDOT reconstruction for TOMOFLUO3D and TOAST, compared with CT volume of the kidney.

With the two comparisons presented above and the quantitative evaluation presented in section 4-6, the three method of reconstruction: the TOMOFLUO3D, the TOAST with conventional geometry and the TOAST with mirror geometry have been compared together. It has been concluded that: first, the TOAST reconstruction with mirror geometry has provided better result than TOAST reconstruction with conventional geometry in term of reconstructed fluorescent intensity. However, further calibration is needed to quantify the reconstruction method with mirror geometry. Then, the TOMOFLUO3D algorithms reconstructed the signal of the two capillaries with a much higher precision in reconstructed volume for the phantom experiment, although the TOAST reconstruction has been better in term of the reconstructed fluorescent

intensity. Overall, a promising result indicating an improvement of the fDOT reconstruction using mirror geometry has been shown; however, further studies are still necessary to quantify this method of the fDOT reconstruction with mirror geometry, as well as to improve the accuracy of TOAST reconstruction performance.

5.3 The use of CT image for mesh generation

In this study, a CT scan of the subject has been used to extract the correct surface volume. However, as presented in section 3.3, the TOMOFLUO3D system incorporates a surface extraction technique which uses a laser to generate the optical surface image. With this surface image, the mesh of the subject can be reconstructed. Yet, the use of a laser line is not capable of accurately reconstructing the lateral sides. The geometry of the surface pattern laser (section 3.3) favours the correct reconstruction of the contour of the upper surface of the mouse. But the form of the animal body creates some “hidden zones” that cannot be reconstructed with the use of the actual surface extracting method (Figure 5-4)

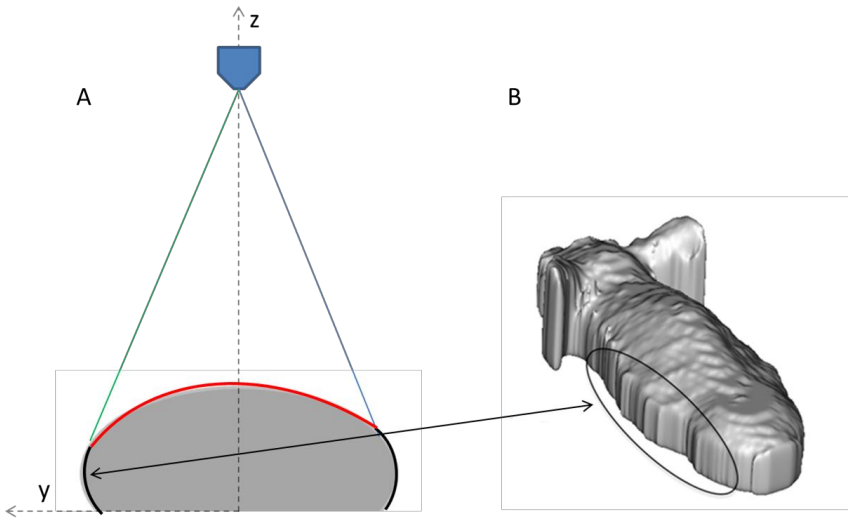


Figure 5-4: The “hidden zoon” where the green laser cannot reach to the surface of the subject, thus the lateral side of the subject cannot be reconstructed with surface extraction technique of the fDOT. A: The red arc show the scanning area of the laser where it is able to extact information of the surface. The black arc corresponds to the zoon where the laser cannot reach to. B: the reconstructed optical mesh of the mouse that lacks the shape of surface on the lateral side .

In the conventional one camera imaging signal is mainly coming from the top surface. In the case of mirrors where the lateral signals are incorporated, an accurate reconstruction of the lateral regions of the subject is necessary. As a consequence, the CT scan of the subject has been used to extract the accurate surface volume, especially of the lateral side of the subject.

However, the objective of this study as defined at the beginning was to improve the fDOT reconstruction quality with the help of two mirrors adding to the conventional fDOT system. It was not expected to involve a third modality other than PET and fDOT, since the advantage of our previous study on the PET/fDOT image co-registration was the absence of the CT as a reference modality. Therefore, instead of using CT image for the mesh volume, the optical surface extraction technique incorporated in the TOMOFLUO3D system could be improved to adapt to the mirror geometry. The most obvious solution is that during the optical surface image acquisition, the green planar laser scans the subject under the mirror geometry: first, the lateral sides of the subject is illuminated by the green laser reflected by the mirrors, and then, the surface image of lateral side is reflected by the mirror recorded by the CCD camera (Figure 5-5).

As shown in figure 5-5, under this geometry, double or even triple reflection of the green laser signal takes place during the optical surface image acquisition. The situation becomes very complicated, as it is hard to define the path of the light transmission and the solid angle where the surface of the subject is recorded by the CCD camera, especially when the subject is of arbitrary shape. Moreover, since the accuracy of the optical mesh depends on the quality of the optical surface image while the signal to noise ratio of surface image is sensitive to the laser reflectance and the exposure time of the laser, it is not ideal that the method introduces complicated laser illumination.

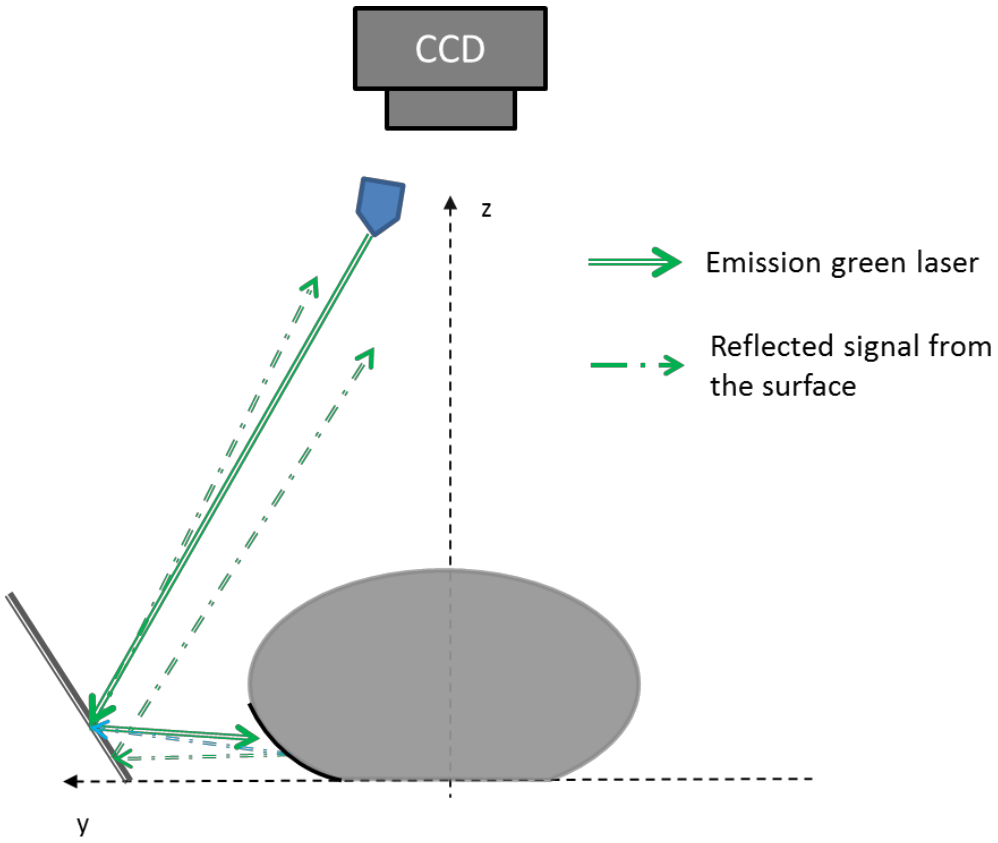


Figure 5-5: Scheme of the acquisition of the surface image on the lateral side of the subject, with the planar green laser scanning the subject under the mirror geometry (example of one side only). The green laser illuminates the lateral surface via mirror reflection; The reflecting surface signal upon illumination (green spot line) will then be recorded by the CCD camera.

Therefore, it is necessary to find another solution that allows generating the mesh for fDOT reconstruction under mirror geometry, without the use of a third modality. However, since this problem was not addressed in this thesis, it is too early to say that the optical surface extraction technique cannot be used to solve this problem. Further studies remain to be done in order to e.g. find the experimental or theoretical tools to minimize the complexity brought by the laser reflections.

5.4 Conclusion

To conclude, this thesis has presented the molecular imaging techniques as tools to explore biological and physiological information of the living tissue at molecular level. Among different techniques for molecular imaging, the fDOT has recently emerged to provide volumetric and quantitative information of fluorescent contrast in-vivo. The fDOT imaging after calibration provides functional quantitative fluorescent images and is relatively low-cost incorporating non-ionizing radiation comparing to other imaging modalities. Additionally, benefits from combining the fDOT image with other well-established imaging techniques can be expected. In this thesis a novel method was developed for co-registering Positron Emission Tomography (PET) with fDOT.

The method for co-registration of PET and fDOT presented here is based on the detection of the position coordinates of FM visible by both modalities. While detection of radiolabelled FM with PET is relatively straightforward, it is not trivial for fDOT since planar optical images do not provide any information on the position of the FM in the z axis. With these limitations in mind, we developed a semi-automatic method based on the combination of a planar optical image with a surface scan of the animal that automatically determines the full 3D coordinates of four FM placed around the body of the animal.

Moreover the method allows the precise and fast co-registration of individually taken images without any operator dependent bias which can be advantageous when a study involves a large amount of experiments. It allows the processing of throughput measurements in a supervision-free manner. The accuracy of co-registration with the present automatic method was comparable to that of manual methods, and found to be better than that of the barycenter-based (BC) approach, while being as accurate as an experienced human observer. The aforementioned evaluation results show the advantages of our method in terms of reliability and robustness.

As a proof of concept, co-registered images of two well-established hallmarks of cancer were imaged: deregulation of glucose consumption through aerobic glycolysis

and increased vascularization through angiogenesis and neo-vessel formation. Automatic co-registration of glycolysis with FDG-PET and vascularity with Sentidye® fDOT clearly demonstrated that the two signals were independently distributed in Multiple Endocrine Neoplasis syndrome type 2A (MEN2A-induced medullary thyroid carcinoma (MTC) xenografts. MEN2A syndromes are linked to a mutation of the RET (rearranged during transfection) proto-oncogene coding for a membrane tyrosine kinase receptor.

It is noteworthy that co-registration of fDOT and PET offers the interesting possibility to co-register and therefore visualize two purely molecular contrast–based imaging methods, without the need for referring to another anatomical imaging method. The proposed co-registration method can easily be customized for specific applications. The method can also be applied to co-registration between fDOT and modalities other than PET, such as CT or MRI, as long as the images contain the relevant FM.

Future applications could include the use of other types of fluorescent probes, in particular those that are activated only after interaction with the target for the monitoring of a variety of tumor-related molecules (Nahrendorf et al., 2010). Additionally, since optical imaging allows the imaging of several probes with distinct emission spectra at the same time, the concept of complementing the FDG signal with a growing number of information could be further extended. The benefits from the fusion of fDOT and PET in combination with CT are expected to give rise to scanners where the two modalities are integrated within the same apparatus and there are ongoing efforts for the development of this type of methods (Li et al., 2009, 2011; Solomon et al., 2011). The combination of these two modalities offers new opportunities for describing tissue physiopathology non-invasively at refined molecular levels, and opens experimental molecular imaging to simultaneous detection of multiple molecular targets and activities (“multiplexing”).

In the first part of the present thesis, an automatic co-registration method has been developed for fusing fDOT with PET. This combination of modalities is not quite common in the field of molecular imaging. The benefits of this approach have been

discussed previously in the manuscript. Multimodal PET/fDOT images allow a direct comparison of the two machines and may serve in the evaluation of the fDOT in particular since it represents a novel technique. fDOT is in constant development since its first implementation fifteen years ago. New acquisition geometries are proposed based on the experimental needs, the cost and the reconstruction quality. A parameter that has been the target of improvements has been the resolution accuracy. The multi-angle approach of the fluorescence diffuse optical tomography may improve performance over the conventional fDOT imaging system in terms of the spatial resolution in depth.

Under this context, a new multi-angle fDOT system has been developed which by slightly modifying a standard fDOT scanner. Optical imaging benefits from optical components that may redirect photon signal. Based on this principle, the positioning of two mirrors in the two sides of the subject is considered equivalent to using two additional cameras. Therefore the simplicity of the original fDOT systems is retained while the information that can be recorded is multiplied. This modification can be easily implemented to the majority of the fDOT scanners incorporating trans-illumination geometry with the subject lying on a plate holder.

In the present study the FEM-based TOAST reconstruction algorithm forward model (Schweiger, 1994) was modified in order to account for the new geometry. The mirror approach was implemented to provide multi-angle acquisitions of a phantom and a mouse. Reconstructions have been performed with the use of multi-angle data and the results were compared to those of the conventional geometry.

A phantom experiment and an in-vivo experiment have been performed. The comparison and the quantitative evaluation showed that the mirror geometry fDOT system yields better reconstruction performance, especially in terms of the position and the shape of the reconstructed structures. However, this method should be further tested in phantoms of different shapes and in in-vivo models. Also the evaluation of the quality of the fDOT reconstruction by CT could be improved by using CT contrast agents that can provide better contrast of the targeted organs. The development of dual CT/optical probes is expected to optimize the evaluation of the fDOT

reconstructions by comparing them directly to the high resolution CT images.

The mirror modification proposed in this study is not affecting the positioning of the animal in the fDOT scanner. Therefore the simplicity of the fDOT/PET co-registration approach is retained. A mirror-based fDOT system could lead to better reconstructions for the case of combined fDOT/PET imaging.

To summarize, the study presented here aims at contributing to the development of the fDOT imaging. Benefits from the above described approaches can be applied to a wide field of applications. Accurate fDOT reconstructions and co-registration techniques combining multiple imaging modalities would likely to (i) facilitate in vitro to in vivo correlations through ex vivo fluorescent imaging of pathological samples (Nahrendorf et al., 2010); (ii) document the mechanism of uptake of clinically used radiotracers and contrast agents by adding complementary molecular information (Nahrendorf et al., 2010); (iii) decipher the changes induced by administration of therapy (Kossodo et al., 2010); and (iv) validate the in vivo targeting capacity of new molecular probes prior to radioactive labeling for PET or SPECT or tagging with paramagnetic atoms for MRI (Nahrendorf et al., 2010).

6 Annex

6.1 An example of the mesh file in TOAST

Mesh file header

MeshData 5.0

Node coordinate list

NodeList n d

x1 y1 [z1]

x2 y2 [z2]

...

xn yn [zn]

where n is the number of nodes in the list, and d is the number of degrees of freedom per node. Values for d other than 1 are currently not supported.

Element connectivity list

ElementList m

t1 n1,1 n1,2 ... n1,v(t1)

t2 n2,1 n2,2 ... n2,v(t2)

...

tm nm,1 nm,2 ... nm,v(tm)

where m is the number of elements in the list, ti is a one-character identifier for the element type, and ni,j is the node index for the j-th node of element i.

6.2 An example of the QM file in TOAST

Header

`QM file`
`Dimension` *d*
d is 2 or 3, for 2D and 3D problems

Source list

`SourceList` *n* [`fixed`]
x_1 y_1 [z_1]
x_2 y_2 [z_2]
...
x_n y_n [z_n]
where *n* is the number of sources in the list, which itself contains of the Cartesian 2D or 3D coordinates of each of the source points. If `fixed' is specified after n, then toast will use these positions directly without modifications. Otherwise, toast will shift them to the closest boundary point r, and from there to a distance of $1/\mu_s(r)$ below the boundary, along the surface normal at r. With fixed source points, it is the responsibility of the user to ensure the positions are not outside the mesh.

Measurement list

`MeasurementList` *m*
x_1 y_1 [z_1]
x_2 y_2 [z_2]
...
x_m y_m [z_m]
which defines the cartesian coordinates of m detector locations on the surface. If a specified position is not located exactly on the mesh boundary, toast will shift it to the

nearest boundary point. Locations should be defined as close to the boundary as possible to avoid placement errors.

Link list

LinkList
d_1: $m_{1,1}$ $m_{2,1}$ ... $m_{d1,1}$
d_2: $m_{1,2}$ $m_{2,2}$ ... $m_{d2,2}$
...
d_n: $m_{1,n}$ $m_{2,n}$ ... $m_{dn,n}$

The link list contains one line for each source. d_i is the number of detectors active for source i. $m_{1,i}$ ... $m_{di,i}$ is the detector index list for source i. Note that this index list is zero-based, i.e. index 0 refers to the first entry in the MeasurementList. $d_i > 0$ is required, i.e. each source must be linked to at least a single detector. The total number of measurements is $d = d_1+d_2+...+d_n$. Each data file associated with a given QM file is expected to contain d entries.

7 List of publication and communications

Published paper:

- Xiao Tong, Anikitos Garofalakis, Albertine Dubois, Raphaël Boisgard, Frédéric Duconge, Régine Trebossen, Bertrand Tavitian: Co-registration of glucose metabolism with positron emission tomography and vascularity with fluorescent diffuse optical tomography in mouse tumors. EJNMMI Research, 2:19, 2012

Conference:

- Xiao Tong, Anikitos Garofalakis, Albertine Dubois, Raphael Boisgard, Bertrand Tavitian: An Automatic Method for Co-registration of Small Animal Optical Tomographic Imaging with Other Imaging Modalities. World Molecular Imaging Congress (WMIC) 2011. Poster Session 4, P486. San Diego, CA. 7-10 September 2011
- Xiao Tong, Anikitos Garofalakis, Albertine Dubois, Raphaël Boisgard, Frédéric Duconge, Régine Trebossen, Bertrand Tavitian: A semi-automatic method for co-registration of small animal optical tomographic imaging with other imaging modalities. Présentation poster à l' European Molecular Imaging Meeting(EMIM), Leiden, Pays-Bas, 19-21 Juin 2011

Seminar:

- Xiao Tong, Co-registration of optical tomography (fDOT) with Positron emission tomography and development of multi-angle optical tomography. Présentation orale à la journée des doctorants des infrastructures de l'I2BM, 26 juin 2012

8 References

Anand, P., Kunnumakara, A.B., Sundaram, C., Harikumar, K.B., Tharakan, S.T., Lai, O.S., Sung, B., and Aggarwal, B.B. (2008). Cancer is a Preventable Disease that Requires Major Lifestyle Changes. Pharm Res *25*, 2097–2116.

Anderson, C.J., and Ferdani, R. (2009). Copper-64 radiopharmaceuticals for PET imaging of cancer: advances in preclinical and clinical research. Cancer Biother. Radiopharm. *24*, 379–393.

Arridge, S.R. (1995). Photon-measurement density functions. Part I: Analytical forms. Appl. Opt. *34*, 7395–7409.

Arridge, S.R. (1999). Topical review: Optical tomography in medical imaging. Inverse Prob *15*, 41–93.

Arridge, S.R., and Schweiger, M. (1995). Photon-measurement density functions. Part 2: Finite-element-method calculations. Appl. Opt. *34*, 8026–8037.

Arun, K.S., Huang, T.S., and Blostein, S.D. (1987). Least-squares fitting of two 3-d point sets. IEEE Trans Pattern Anal Mach Intell *9*, 698–700.

Ashburner, J., and Friston, K. (2004). Rigid body registration (London: Elsevier Pres).

Benaron, D.A., Hintz, S.R., Villringer, A., Boas, D., Kleinschmidt, A., Frahm, J., Hirth, C., Obrig, H., Van Houten, J.C., Kermit, E.L., et al. (2000). Noninvasive functional imaging of human brain using light. J. Cereb. Blood Flow Metab. *20*, 469–477.

Bernardini, F., and Rushmeier, H. (2002). The 3D Model Acquisition Pipeline. Computer Graphics Forum *21*, 149–172.

Beyer, T., Townsend, D.W., Brun, T., Kinahan, P.E., Charron, M., Roddy, R., Jerin, J., Young, J., Byars, L., and Nutt, R. (2000). A combined PET/CT scanner for clinical oncology. J. Nucl. Med. *41*, 1369–1379.

Black, W.C. (1998). Advances in radiology and the real versus apparent effects of early diagnosis. Eur. J. Radiol. *27*, 116–122.

Boas, D.A. (1996). Diffuse Photon Probes of Structural and Dynamical Properties of Turbid Media: Theory and Biomedical Applications (Graduate School of Arts and Sciences, University of Pennsylvania).

Boas, D.A., Chen, K., Grebert, D., and Franceschini, M.A. (2004). Improving the diffuse optical imaging spatial resolution of the cerebral hemodynamic response to brain activation in humans. Opt Lett *29*, 1506–1508.

Boda, S. (2009). Feature-Based Image Registration. MTech thesis. National Insititute of Technology Rourkela

Born, M., and Wolf, E. (1999). Principles of Optics: Electromagnetic Theory of Propagation, Interference and Diffraction of Light (Cambridge University Press).

Boutet, J., Koenig, A., Hervé, L., Berger, M., Dinten, J.-M., Josserand, V., and Coll, J.-L. (2011). Optical tomograph optimized for tumor detection inside highly absorbent organs. Opt. Eng *50*, 053203–053203.

Bremer, C., Ntziachristos, V., and Weissleder, R. (2003). Optical-based molecular imaging: contrast agents and potential medical applications. Eur Radiol *13*, 231–243.

Brown, E.B., Campbell, R.B., Tsuzuki, Y., Xu, L., Carmeliet, P., Fukumura, D., and Jain, R.K. (2001). In vivo measurement of gene expression, angiogenesis and physiological function in tumors using multiphoton laser scanning microscopy. Nat. Med. *7*, 864–868.

Brown, L.G. (1992). A Survey of Image Registration Techniques. ACM Computing Surveys *24*, 325–376.

Cao, L., Breithaupt, M., and Peter, J. (2010). Geometrical co-calibration of a tomographic optical system with CT for intrinsically co-registered imaging. Phys Med Biol *55*, 1591–1606.

Chamorro-Servent, J., Aguirre, J., Ripoll, J., Vaquero, J.J., and Desco, M. (2011). Feasibility of U-curve method to select the regularization parameter for fluorescence diffuse optical tomography in phantom and small animal studies. Opt Express *19*, 11490–11506.

Chance, B., Wang, N.G., Maris, M., Nioka, S., and Sevick, E. (1992). Quantitation of tissue optical characteristics and hemoglobin desaturation by time- and frequency-resolved multi-wavelength spectrophotometry. Adv. Exp. Med. Biol. *317*, 297–304.

Chaudhari, A.J., Darvas, F., Bading, J.R., Moats, R.A., Conti, P.S., Smith, D.J., Cherry, S.R., and Leahy, R.M. (2005). Hyperspectral and multispectral bioluminescence optical tomography for small animal imaging. Phys Med Biol *50*, 5421–5441.

Cherry, S.R. (2006). Multimodality in vivo imaging systems: Twice the Power or Double the Trouble? Annual Review of Biomedical Engineering *8*, 35–62.

Cho, Z.-H., Son, Y.-D., Kim, H.-K., Kim, K.-N., Oh, S.-H., Han, J.-Y., Hong, I.-K., and Kim, Y.-B. (2008). A fusion PET–MRI system with a high-resolution research tomograph-PET and ultra-high field 7.0 T-MRI for the molecular-genetic imaging of the brain. Proteomics *8*, 1302–1323.

Chow, P.L., Stout, D.B., Komisopoulou, E., and Chatziioannou, A.F. (2006). A method of image registration for small animal, multi-modality imaging. Phys Med Biol *51*, 379–390.

Claxton, N.S., Fellers, T.J., and Davidson, M.W. (2006). Microscopy, Confocal. In Encyclopedia of Medical Devices and Instrumentation, (John Wiley & Sons, Inc.),.

Cointepas, Y., Mangin, J.-F., Garnero, L., Poline, J.-B., and Benali, H. (2001). BrainVISA: Software platform for visualization and analysis of multi-modality brain data. NeuroImage *13*, 98.

Contag, C.H., and Bachmann, M.H. (2002). Advances in in Vivo Bioluminescence Imaging of Gene Expression. Annual Review of Biomedical Engineering *4*, 235–260.

Contag, P.R., Olomu, I.N., Stevenson, D.K., and Contag, C.H. (1998). Bioluminescent indicators in living mammals. Nat. Med. *4*, 245–247.

Correia, T., Aguirre, J., Sisniega, A., Chamorro-Servent, J., Abascal, J., Vaquero, J.J., Desco, M., Kolehmainen, V., and Arridge, S. (2011). Split operator method for fluorescence diffuse optical tomography using anisotropic diffusion regularisation with prior anatomical information. Biomed Opt Express *2*, 2632–2648.

Correia, T., Gibson, A., Schweiger, M., and Hebden, J. (2009). Selection of regularization parameter for optical topography. J Biomed Opt *14*, 034044.

Culver, J., Akers, W., and Achilefu, S. (2008). Multimodality molecular imaging

with combined optical and SPECT/PET modalities. J. Nucl. Med. *49*, 169–172.

Culver, J.P., Siegel, A.M., Stott, J.J., and Boas, D.A. (2003). Volumetric diffuse optical tomography of brain activity. Opt Lett *28*, 2061–2063.

Davis, M.H., Khotanzad, A., Flamig, D.P., and Harms, S.E. (1995). Coordinate transformation in 3D image matching by a physics based method-elastic body splines. ISCV 1995,218 –222.

Delbeke, D., and Martin, W.H. (2001). Positron emission tomography imaging in oncology. Radiol. Clin. North Am. *39*, 883–917.

Deliolanis, N., Lasser, T., Hyde, D., Soubret, A., Ripoll, J., and Ntziachristos, V. (2007). Free-space fluorescence molecular tomography utilizing 360° geometry projections. Opt. Lett. *32*, 382–384.

Deriche, R. (1993). Recursively Implementing the Gaussian and its Derivatives. INRIA RR-1893

Egeblad, M., Nakasone, E.S., and Werb, Z. (2010). Tumors as organs: complex tissues that interface with the entire organism. Dev. Cell *18*, 884–901.

Eggert, D.W., Lorusso, A., and Fisher, R.B. (1997). Estimating 3-D rigid body transformations: a comparison of four major algorithms. Mach. Vision Appl. *9*, 272–290.

Elliott, A. (2005). Medical imaging. Nuclear Instruments and Methods in Physics Research Section A: Accelerators, Spectrometers, Detectors and Associated Equipment *546*, 1–13.

Fantini, S., Franceschini, M.A., and Gratton, E. (1997). Effective source term in the diffusion equation for photon transport in turbid media. Appl Opt *36*, 156–163.

Fitzpatrick, J.M., West, J.B., and Maurer, C.R., J. (1998). Predicting error in rigid-body point-based registration. IEEE Trans. Med. Imag. *17*, 694 –702.

Garofalakis, A., Dubois, A., Kuhnast, B., Dupont, D.M., Janssens, I., Mackiewicz, N., Dollé, F., Tavitian, B., and Ducongé, F. (2010). In vivo validation of free-space fluorescence tomography using nuclear imaging. Opt Lett *35*, 3024–3026.

Garofalakis, A., Dubois, A., Thézé, B., Czarny, B., Tavitian, B., and Ducongé, F. (2012). Fusion of [(18)F]FDG PET with Fluorescence Diffuse Optical Tomography to Improve Validation of Probes and Tumor Imaging. Mol Imaging Biol. Epub 2012 Aug 28.

Garofalakis, A., Zacharakis, G., Meyer, H., Economou, E.N., Mamalaki, C., Papamatheakis, J., Kioussis, D., Ntziachristos, V., and Ripoll, J. (2007). Three-dimensional in vivo imaging of green fluorescent protein-expressing T cells in mice with noncontact fluorescence molecular tomography. Mol Imaging *6*, 96–107.

Gillies, R.J., Robey, I., and Gatenby, R.A. (2008). Causes and consequences of increased glucose metabolism of cancers. J. Nucl. Med. *49 Suppl 2*, 24S–42S.

Goertzen, A.L., Meadors, A.K., Silverman, R.W., and Cherry, S.R. (2002). Simultaneous molecular and anatomical imaging of the mouse in vivo. Phys Med Biol *47*, 4315–4328.

Goldman, L.W. (2007). Principles of CT and CT technology. J Nucl Med Technol *35*, 115–128; quiz 129–130.

Gower, J.C., and Dijksterhuis, G.B. (2004). Procrustes Problems (OUP Oxford).

Graves, E.E., Ripoll, J., Weissleder, R., and Ntziachristos, V. (2003). A submillimeter resolution fluorescence molecular imaging system for small animal imaging. Med Phys *30*, 901–911.

Grieve, K., Tiruveedhula, P., Zhang, Y., and Roorda, A. (2006). Multi-wavelength imaging with the adaptive optics scanning laser Ophthalmoscope. Opt. Express *14*, 12230–12242.

Gross, K.A. (2005). A fast model of a multiple-pinhole SPECT imaging system. Proc. SPIE 5749, 118–127.

Gusnard, D.A., Raichle, M.E., and Raichle, M.E. (2001). Searching for a baseline: functional imaging and the resting human brain. Nat. Rev. Neurosci. *2*, 685–694.

Hampel, H., Prvulovic, D., Teipel, S.J., and Bokde, A.L.W. (2011). Recent developments of functional magnetic resonance imaging research for drug development in Alzheimer's disease. Progress in Neurobiology *95*, 570–578.

Hanahan, D., and Weinberg, R.A. (2011). Hallmarks of cancer: the next generation. Cell *144*, 646–674.

Hasegawa, B.H., Iwata, K., Wong, K.H., Wu, M.C., Da Silva, A.J., Tang, H.R., Barber, W.C., Hwang, A.H., and Sakdinawat, A.E. (2002). Dual-modality imaging of function and physiology. Acad Radiol *9*, 1305–1321.

Hervé, L., Koenig, A., Da Silva, A., Berger, M., Boutet, J., Dinten, J.M., Peltié,

P., and Rizo, P. (2007). Noncontact fluorescence diffuse optical tomography of heterogeneous media. Appl Opt *46*, 4896–4906.

Hillman, E.M.C., and Moore, A. (2007). All-optical anatomical co-registration for molecular imaging of small animals using dynamic contrast. Nat Photonics *1*, 526–530.

Horn, B. (1987). Closed-form solution of absolute orientation using unit quaternions. J. Opt. Soc. Am. A *4*, 629–642.

Ishimaru, A. (1978). Wave Propagation and Scattering in Random Media: Multiple scattering, turbulence, rough surfaces, and remote sensing (Academic Press).

Jhiang, S.M. (2000). The RET proto-oncogene in human cancers. Oncogene *19*, 5590–5597.

Kak, A.C., Slaney, M., and Society, I.E. in M. and B. (1988). Principles of computerized tomographic imaging (IEEE Press).

Kapoor, V., McCook, B.M., and Torok, F.S. (2004). An Introduction to PET-CT Imaging1. Radiographics *24*, 523–543.

Khandani, A.H., Calvo, B.F., O'Neil, B.H., Jorgenson, J., and Mauro, M.A. (2007). A pilot study of early 18F-FDG PET to evaluate the effectiveness of radiofrequency ablation of liver metastases. AJR Am J Roentgenol *189*, 1199–1202.

Kim, D.-W., Jung, S.-A., Kim, C.-G., and Park, S.-A. (2010). The efficacy of dual time point F-18 FDG PET imaging for grading of brain tumors. Clin Nucl Med *35*, 400–403.

Koenig, A., Hervé, L., Gonon, G., Josserand, V., Berger, M., Dinten, J.-M., Boutet, J., Peltié, P., Coll, J.-L., and Rizo, P. (2010). Fluorescence diffuse optical tomography for free-space and multifluorophore studies. J. Biomed Opt. *15*, 016016.

Kok, P., Dijkstra, J., Botha, C.P., Post, F.H., Kaijzel, E., Que, I., Löwik, C.W.G.M., Reiber, J.H.C., and Lelieveldt, B.P.F. (2007). Integrated visualization of multi-angle bioluminescence imaging and micro CT. Proc. SPIE 6509, 65091U

Kossodo, S., Pickarski, M., Lin, S.-A., Gleason, A., Gaspar, R., Buono, C., Ho, G., Blusztajn, A., Cuneo, G., Zhang, J., et al. (2010). Dual in vivo quantification of integrin-targeted and protease-activated agents in cancer using fluorescence molecular tomography (FMT). Mol Imaging Biol *12*, 488–499.

Krol, A., Unlu, M.Z., Magri, A., Lipson, E., Coman, I.L., Mandel, J.A., Baum, K.G., and Feiglin, D.H. (2006). Iterative finite element deformable model for nonrigid coregistration of multimodal breast images. pp. 852 –855.

Langheinrich, A.C., Leithäuser, B., Greschus, S., Von Gerlach, S., Breithecker, A., Matthias, F.R., Rau, W.S., and Bohle, R.M. (2004). Acute rat lung injury: feasibility of assessment with micro-CT. Radiology *233*, 165–171.

Li, C., Wang, G., Qi, J., and Cherry, S.R. (2009). Three-Dimensional Fluorescence Optical Tomography in Small Animal Imaging using Simultaneous Positron Emission Tomography Priors. Opt Lett *34*, 2933–2935.

Li, C., Yang, Y., Mitchell, G.S., and Cherry, S.R. (2011). Simultaneous PET and multispectral 3-dimensional fluorescence optical tomography imaging system. J. Nucl. Med. *52*, 1268–1275.

Liu, X. (2003). Marker orientation in fiducial registration. (SPIE), pp. 1176–1185.

Lovell, J.F., and Zheng, G. (2008). Activatable Smart Probes for Molecular Optical Imaging and Therapy. J. Innov Opt. Health. Sci. 01, 45–61.

Maeda, H., Wu, J., Sawa, T., Matsumura, Y., and Hori, K. (2000). Tumor vascular permeability and the EPR effect in macromolecular therapeutics: a review. J Control Release *65*, 271–284.

Marks, R.J. (1991). Introduction to Shannon sampling and interpolation theory (Springer-Verlag).

Martin, A., Aguirre, J., Sarasa-Renedo, A., Tsoukatou, D., Garofalakis, A., Meyer, H., Mamalaki, C., Ripoll, J., and Planas, A.M. (2008). Imaging changes in lymphoid organs in vivo after brain ischemia with three-dimensional fluorescence molecular tomography in transgenic mice expressing green fluorescent protein in T lymphocytes. Mol Imaging *7*, 157–167.

Massoud, T.F., and Gambhir, S.S. (2003). Molecular imaging in living subjects: seeing fundamental biological processes in a new light. Genes Dev. *17*, 545–580.

Mattson, M.. (2000). Emerging neuroprotective strategies for Alzheimer's disease: dietary restriction, telomerase activation, and stem cell therapy. Experimental Gerontology *35*, 489–502.

McLaughlin, R., Hipwell, J., Hawkes, D., Noble, J.A., Byrne, J., and Cox, T. (2002). A Comparison of 2D-3D Intensity-Based Registration and Feature-Based Registration for Neurointerventions. In Medical Image Computing and Computer-Assisted Intervention — MICCAI 2002, T. Dohi, and

R. Kikinis, eds. (Springer Berlin / Heidelberg), 517–524.

Van der Meel, R., Gallagher, W.M., Oliveira, S., O'Connor, A.E., Schiffelers, R.M., and Byrne, A.T. (2010). Recent advances in molecular imaging biomarkers in cancer: application of bench to bedside technologies. Drug Discovery Today *15*, 102–114.

Meyer, H., Garofalakis, A., Zacharakis, G., Psycharakis, S., Mamalaki, C., Kioussis, D., Economou, E.N., Ntziachristos, V., and Ripoll, J. (2007). Noncontact optical imaging in mice with full angular coverage and automatic surface extraction. Appl Opt *46*, 3617–3627.

Michiels, F.M., Chappuis, S., Caillou, B., Pasini, A., Talbot, M., Monier, R., Lenoir, G.M., Feunteun, J., and Billaud, M. (1997). Development of medullary thyroid carcinoma in transgenic mice expressing the RET protooncogene altered by a multiple endocrine neoplasia type 2A mutation. Proc. Natl. Acad. Sci. U.S.A. *94*, 3330–3335.

Miller, J.C., and Thrall, J.H. (2004). Clinical molecular imaging. Journal of the American College of Radiology *1*, 4–23.

Montcel, B., Chabrier, R., and Poulet, P. (2006). Time-resolved absorption and hemoglobin concentration difference maps: a method to retrieve depth-related information on cerebral hemodynamics. Opt Express *14*, 12271–12287.

Montcel, B., and Poulet, P. (2006). An instrument for small-animal imaging using time-resolved diffuse and fluorescence optical methods. Nuclear Instruments and Methods in Physics Research Section A: Accelerators, Spectrometers, Detectors and Associated Equipment *569*, 551–556.

Munnink, T.H.O., Nagengast, W.B., Brouwers, A.H., Schröder, C.P., Hospers, G.A., Hooge, M.N.L., Van der Wall, E., Van Diest, P.J., and De Vries, E.G.E. (2009). Molecular imaging of breast cancer. The Breast *18, Supplement 3*, S66–S73.

Myers, R., and Hume, S. (2002). Small animal PET. Eur Neuropsychopharmacol *12*, 545–555.

Nagy, J.A., Chang, S.-H., Shih, S.-C., Dvorak, A.M., and Dvorak, H.F. (2010). Heterogeneity of the tumor vasculature. Semin. Thromb. Hemost. *36*, 321–331.

Nahrendorf, M., Keliher, E., Marinelli, B., Waterman, P., Feruglio, P.F., Fexon, L., Pivovarov, M., Swirski, F.K., Pittet, M.J., Vinegoni, C., et al. (2010). Hybrid PET-optical imaging using targeted probes. PNAS *107*, 7910–7915.

Nahrendorf, M., Sosnovik, D.E., French, B.A., Swirski, F.K., Bengel, F.,

Sadeghi, M.M., Lindner, J.R., Wu, J.C., Kraitchman, D.L., Fayad, Z.A., et al. (2009). Multimodality Cardiovascular Molecular Imaging, Part II. Circ Cardiovasc Imaging *2*, 56–70.

Nanni, C., Rubello, D., Khan, S., Al-Nahhas, A., and Fanti, S. (2007). Role of small animal PET in stimulating the development of new radiopharmaceuticals in oncology. Nucl Med Commun *28*, 427–429.

Nayak, T.K., Garmestani, K., Baidoo, K.E., Milenic, D.E., and Brechbiel, M.W. (2011). PET imaging of tumor angiogenesis in mice with VEGF-A-targeted (86)Y-CHX-A″-DTPA-bevacizumab. Int. J. Cancer *128*, 920–926.

Nekolla, S.G., Martinez-Moeller, A., and Saraste, A. (2009). PET and MRI in cardiac imaging: from validation studies to integrated applications. Eur. J. Nucl. Med. Mol. Imaging *36 Suppl 1*, S121–130.

Nelson, G.S., Perez, J., Colomer, M.V., Ali, R., and Graves, E. (2011). Facilitating multimodal preclinical imaging studies in mice by using an immobilization bed. Comp. Med. *61*, 499–504.

Nolting, D.D., Gore, J.C., and Pham, W. (2011). NEAR-INFRARED DYES: Probe Development and Applications in Optical Molecular Imaging. Curr Org Synth *8*, 521–534.

Ntziachristos, V. (2006). Fluorescence Molecular Imaging. Annual Review of Biomedical Engineering *8*, 1–33.

Ntziachristos, V., and Chance, B. (2001). Probing physiology and molecular function using optical imaging: applications to breast cancer. Breast Cancer Res. *3*, 41–46.

Ntziachristos, V., Hielscher, A.H., Yodh, A.G., and Chance, B. (2001). Diffuse optical tomography of highly heterogeneous media. IEEE Trans Med Imag. *20*, 470–478.

Ntziachristos, V., Tung, C.-H., Bremer, C., and Weissleder, R. (2002). Fluorescence molecular tomography resolves protease activity in vivo. Nat. Med. *8*, 757–760.

Ntziachristos, V., Turner, G., Dunham, J., Windsor, S., Soubret, A., Ripoll, J., and Shih, H.A. (2005). Planar fluorescence imaging using normalized data. J Biomed Opt *10*, 064007.

Ntziachristos, V., and Weissleder, R. (2001). Experimental three-dimensional fluorescence reconstruction of diffuse media by use of a normalized Born approximation. Opt Lett *26*, 893–895.

Patterson, M.S., Chance, B., and Wilson, B.C. (1989). Time resolved reflectance and transmittance for the non-invasive measurement of tissue optical properties. Appl. Opt. *28*, 2331–2336.

Petrangolini, G., Cuccuru, G., Lanzi, C., Tortoreto, M., Belluco, S., Pratesi, G., Cassinelli, G., and Zunino, F. (2006). Apoptotic cell death induction and angiogenesis inhibition in large established medullary thyroid carcinoma xenografts by Ret inhibitor RPI-1. Biochem. Pharmacol. *72*, 405–414.

Pluim, J.P.W., Maintz, J.B.A., and Viergever, M.A. (2003). Mutual-information-based registration of medical images: a survey. IEEE Trans. Med. Imag. *22*, 986 –1004.

Prout, D.L., Silverman, R.W., and Chatziioannou, A. (2004). Detector Concept for OPET-A Combined PET and Optical Imaging System. IEEE Trans Nucl Sci *51*, 752–756.

Pryma, D.A., Schöder, H., Gönen, M., Robbins, R.J., Larson, S.M., and Yeung, H.W.D. (2006). Diagnostic accuracy and prognostic value of 18F-FDG PET in Hürthle cell thyroid cancer patients. J. Nucl. Med. *47*, 1260–1266.

Riker, A., Libutti, S.K., and Bartlett, D.L. (1997). Advances in the early detection, diagnosis, and staging of pancreatic cancer. Surgical Oncology *6*, 157–169.

Ripoll, J., Schulz, R.B., and Ntziachristos, V. (2003). Free-space propagation of diffuse light: theory and experiments. Phys. Rev. Lett. *91*, 103901.

Ripoll, J., Yessayan, D., Zacharakis, G., and Ntziachristos, V. (2005). Experimental determination of photon propagation in highly absorbing and scattering media. J Opt Soc Am A Opt Image Sci Vis *22*, 546–551.

Roncali, E., Savinaud, M., Levrey, O., Rogers, K.L., Maitrejean, S., and Tavitian, B. (2008). New device for real-time bioluminescence imaging in moving rodents. J Biomed Opt *13*, 054035.

Rudin, M. (2005). Molecular Imaging – Basic principles and applications to biomedical research. (London: Imperial College Press).

Rudin, M., Rausch, M., and Stoeckli, M. (2005). Molecular imaging in drug discovery and development: potential and limitations of nonnuclear methods. Mol Imaging Biol *7*, 5–13.

Schulz, R.B., Ale, A., Sarantopoulos, A., Freyer, M., Soehngen, E., Zientkowska, M., and Ntziachristos, V. (2010). Hybrid System for Simultaneous Fluorescence and X-Ray Computed Tomography. IEEE Trans. Med. Imag. *29*, 465 –473.

Schulz, R.B., Ripoll, J., and Ntziachristos, V. (2004). Experimental fluorescence tomography of tissues with noncontact measurements. IEEE Trans Med Imag. *23*, 492–500.

Schweiger, M. (1994). Application of finite element method in infrared reconstruction of scattering media. Ph.D Thesis. University of London.

Schweiger, M., Arridge, S.R., and Delpy, D.T. (1993). Application of the finite-element method for the forward and inverse models in optical tomography. J. Math. Imaging Vis. *3*, 263–283.

Sharma, P., Brown, S., Walter, G., Santra, S., and Moudgil, B. (2006). Nanoparticles for bioimaging. Advances in Colloid and Interface Science *123–126*, 471–485.

Sharma, S., and Ebadi, M. (2008). SPECT neuroimaging in translational research of CNS disorders. Neurochemistry International *52*, 352–362.

Da Silva, A., Bordy, T., Debourdeau, M., Dinten, J.-M., Peltié, P., and Rizo, P. (2007). Whole body in vivo examination of small animals by simultaneous X-rays/optical tomography: comparison between the reconstructions obtained with different types of fluorescent labels. SPIE Proc. 6629-37.

Soh, E.Y., Sobhi, S.A., Wong, M.G., Meng, Y.G., Siperstein, A.E., Clark, O.H., and Duh, Q.Y. (1996). Thyroid-stimulating hormone promotes the secretion of vascular endothelial growth factor in thyroid cancer cell lines. Surgery *120*, 944–947.

Solomon, M., White, B.R., Nothdruft, R.E., Akers, W., Sudlow, G., Eggebrecht, A.T., Achilefu, S., and Culver, J.P. (2011). Video-rate fluorescence diffuse optical tomography for in vivo sentinel lymph node imaging. Biomed Opt Express *2*, 3267–3277.

Stahl, A., Wieder, H., Piert, M., Wester, H.-J., Senekowitsch-Schmidtke, R., and Schwaiger, M. (2004). Positron emission tomography as a tool for translational research in oncology. Mol. Imaging Biol. *6*, 214–224.

Stout, D.B., and Zaidi, H. (2008). Preclinical Multimodality Imaging in Vivo. PET Clinics *3*, 251–273.

Strang, G., and Fix, G.J. (2008). An Analysis of the Finite Element Method (Wellesley-Cambridge Press).

Suckow, C., Kuntner, C., Chow, P., Silverman, R., Chatziioannou, A., and Stout, D. (2009). Multimodality rodent imaging chambers for use under barrier conditions with gas anesthesia. Mol Imaging Biol *11*, 100–106.

Sweeney, T.J., Mailänder, V., Tucker, A.A., Olomu, A.B., Zhang, W., Cao, Y., Negrin, R.S., and Contag, C.H. (1999). Visualizing the kinetics of tumor-cell clearance in living animals. PNAS *96*, 12044–12049.

Tabuchi, A., Mertens, M., Kuppe, H., Pries, A.R., and Kuebler, W.M. (2008). Intravital microscopy of the murine pulmonary microcirculation. J Appl Physiol *104*, 338–346.

Teverovskiy, L.A., Carmichael, O.T., Aizenstein, H.J., Lazar, N., and Liu, Y. (2007). Feature-Based vs. Intensity-Based Brain Image Registration: Comprehensive Comparison Using Mutual Information. ISBI 2007: 576-579.

Torchilin, V.P. (2007). Targeted pharmaceutical nanocarriers for cancer therapy and imaging. AAPS J *9*, E128–E147.

Townsend, D.W. (2004). Physical principles and technology of clinical PET imaging. Ann. Acad. Med. Singap. *33*, 133–145.

Townsend, D.W. (2008). Multimodality imaging of structure and function. PMB *53*, R1–R39.

Tsukada, H. (2011). [Application of pre-clinical PET imaging for drug development]. Nihon Shinkei Seishin Yakurigaku Zasshi *31*, 231–237.

Turner, G.M., Zacharakis, G., Soubret, A., Ripoll, J., and Ntziachristos, V. (2005). Complete-angle projection diffuse optical tomography by use of early photons. Opt Lett *30*, 409–411.

Viel, T., Dransart, E., Nemati, F., Henry, E., Thézé, B., Decaudin, D., Lewandowski, D., Boisgard, R., Johannes, L., and Tavitian, B. (2008). In vivo tumor targeting by the B-subunit of shiga toxin. Mol Imaging *7*, 239–247.

Vira, S., Mekhedov, E., Humphrey, G., and Blank, P.S. (2010). Fluorescent labeled antibodies - balancing functionality and degree of labeling. Anal Biochem *402*, 146–150.

Wang, G., Shen, H., Liu, Y., Cong, A., Cong, W., Wang, Y., and Dubey, P. (2008). Digital spectral separation methods and systems for bioluminescence imaging. Opt Express *16*, 1719–1732.

Wang, M.Y., Maurer, C.R., Jr, Fitzpatrick, J.M., and Maciunas, R.J. (1996). An automatic technique for finding and localizing externally attached markers in CT and MR volume images of the head. IEEE Trans Biomed Eng *43*, 627–637.

Weaver, W., and Gere, J.M. (1980). Matrix analysis of framed structures (New York: D. Van Nostrand Co.).

Weissleder, R. (1999). Molecular imaging: exploring the next frontier. Radiology *212*, 609–614.

Weissleder, R. (2001). A clearer vision for in vivo imaging. Nat. Biotechnol. *19*, 316–317.

Weissleder, R. (2002). Scaling down imaging: molecular mapping of cancer in mice. Nat. Rev. Cancer *2*, 11–18.

Weissleder, R. (2006). Molecular imaging in cancer. Science *312*, 1168–1171.

Weissleder, R., and Mahmood, U. (2001). Molecular Imaging1. Radiology *219*, 316–333.

Weissleder, R., and Ntziachristos, V. (2003). Shedding light onto live molecular targets. Nat. Med. *9*, 123–128.

Weissleder, R., Tung, C.H., Mahmood, U., and Bogdanov, A., Jr (1999). In vivo imaging of tumors with protease-activated near-infrared fluorescent probes. Nat. Biotechnol. *17*, 375–378.

West, J., Fitzpatrick, J.M., Wang, M.Y., Dawant, B.M., Maurer, C.R., Jr, Kessler, R.M., Maciunas, R.J., Barillot, C., Lemoine, D., Collignon, A., et al. (1997). Comparison and evaluation of retrospective intermodality brain image registration techniques. J Comput Assist Tomogr *21*, 554–566.

Widmark, J.M. (2007). Imaging-related medications: a class overview. Proc (Bayl Univ Med Cent) *20*, 408–417.

Yang, C.C., Wu, T.H., Lin, M.H., Huang, Y.H., Guo, W.Y., Chen, C.L., Wang, T.C., Yin, W.H., and Lee, J.S. (2006). Multimodality imaging combination in small animal via point-based registration. Nuclear Instruments and Methods in Physics Research Section A: Accelerators, Spectrometers, Detectors and Associated Equipment *569*, 240–244.

Yodh, A., and Chance, B. (1995). Spectroscopy and Imaging with Diffusing Light. Physics Today *48*, 34.

Yodh, A.G. (2008). Breast cancer imaging and stroke monitoring with diffuse optics. Conf Proc IEEE Eng Med Biol Soc *2008*, 1.

Zacharakis, G., Kambara, H., Shih, H., Ripoll, J., Grimm, J., Saeki, Y., Weissleder, R., and Ntziachristos, V. (2005a). Volumetric tomography of fluorescent proteins through small animals in vivo. Proc. Natl. Acad. Sci. U.S.A. *102*, 18252–18257.

Zacharakis, G., Ripoll, J., Weissleder, R., and Ntziachristos, V. (2005b).

Fluorescent protein tomography scanner for small animal imaging. IEEE Trans Med Imag. *24*, 878–885.

Zhang, J., Campbell, R.E., Ting, A.Y., and Tsien, R.Y. (2002). Creating new fluorescent probes for cell biology. Nat. Rev. Mol. Cell Biol. *3*, 906–918.

Zhang, Z. (1994). Iterative point matching for registration of free-form curves and surfaces. Int. J. Comput. Vision *13*, 119–152.

.